2015

Pulsar population synthesis using palfa detections and pulsar search collaboratory discoveries including a wide DNS system and a nearby MSP

Joseph Karl Swiggum

Recommended Citation
Swiggum, Joseph Karl, "Pulsar population synthesis using palfa detections and pulsar search collaboratory discoveries including a wide DNS system and a nearby MSP" (2015). *Graduate Theses, Dissertations, and Problem Reports*. 6754.
https://researchrepository.wvu.edu/etd/6754

PULSAR POPULATION SYNTHESIS USING PALFA DETECTIONS AND PULSAR SEARCH COLLABORATORY DISCOVERIES INCLUDING A WIDE DNS SYSTEM AND A NEARBY MSP

Joseph Karl Swiggum

Dissertation submitted to
the Eberly College of
Arts and Sciences at
West Virginia University
in partial fulfillment of
the requirements for
the degree of

Doctor of Philosophy
in
Physics

Dr. Duncan Lorimer, Ph.D., Chair
Dr. Maura McLaughlin, Ph.D.
Dr. Loren Anderson, Ph.D.
Dr. Paul Miller, Ph.D.
Dr. Natalia Schmid, Ph.D.

Department of Physics

Morgantown, West Virginia
2015

Keywords: pulsars: surveys (PALFA, GBT 350 MHz drift scan), individual (PSR J1400−1432, PSR J1631−1612, PSR J1821+0155, PSR J1926−1314, PSR J1930−1852, PSR J2136−1606)

ABSTRACT

PULSAR POPULATION SYNTHESIS USING PALFA DETECTIONS AND PULSAR SEARCH COLLABORATORY DISCOVERIES INCLUDING A WIDE DNS SYSTEM AND A NEARBY MSP

Joseph Karl Swiggum

Using the ensemble of detections from pulsar surveys, we can learn about the sizes and characteristics of underlying populations. In this thesis, I analyze results from the Pulsar Arecibo L-band Feed Array (PALFA) precursor and Green Bank Telescope 350 MHz Drift Scan surveys; I examine survey sensitivity to see how detections can inform pulsar population models, I look at new ways of including young scientists – high school students – in the discovery process and I present timing solutions for students' discoveries (including a nearby millisecond pulsar and a pulsar in a wide-orbit double neutron star system).

The PALFA survey is on-going and uses the ALFA 7-beam receiver at 1400 MHz to search both inner and outer Galactic sectors visible from Arecibo (32° � £ � 77° and 168° � £ � 214°) close to the Galactic plane ($|b|$ � 5°) for pulsars. The PALFA precursor survey observed a subset of this region, ($|b|$ � 1°) and detected 45 pulsars, including one known millisecond pulsar (MSP) and 11 previously unknown, long-period (normal) pulsars. I assess the sensitivity of the PALFA precursor survey and use the number of normal pulsar and MSP detections to infer the size of each underlying Galactic population. Based on 44 normal pulsar detections and one MSP, we constrain each population size to $107,000^{+36,000}_{-25,000}$ and $15,000^{+85,000}_{-6,000}$ respectively with 95% confidence. Based on these constraints, we predict yields for the full PALFA survey and find a deficiency in normal pulsar detections, possibly due to radio frequency interference and/or scintillation, neither of which are currently accounted for in population simulations.

The GBT 350 MHz Drift Scan survey collected data in the summer of 2007 while the GBT was stationary, undergoing track replacement. Results discussed here come from $\sim 20\%$ of the survey data, which were processed and donated to the Pulsar Search Collaboratory (PSC). The PSC is a joint outreach program between WVU and NRAO, involving high school students in the pulsar discovery process – hands-on, cutting-edge research – to foster their interest in pursuing Science, Technology, Engineering and Mathematics (STEM) related career paths. The PSC began in 2008; since then, over 100 teachers and 2,500 students from 18 states have participated and discovered seven pulsars. Of these seven, J1400−1431, a bright, nearby MSP shows promising characteristics for inclusion in pulsar timing arrays, which aim to detect gravitational waves by precisely timing an array of MSPs. Two others – J1821+0155, a disrupted recycled pulsar and J1930−1852 show interesting properties due to interactions with binary companions. PSR J1930−1852 is a partially-recycled, first-to-evolve pulsar in a double neutron star (DNS) system with a high-eccentricity 45 day orbit. Its spin period and orbital period are factors of 2 and 3 higher, respectively, than any previously-known, primary DNS pulsars. We measure the relativistic advance of periastron $\dot{\omega} = 0.00078(4)$, implying a total system mass of $M_{\rm tot} = 2.59(4)$, which is consistent with other DNS systems. PSR J1930−1852's spin and orbital parameters, however, challenge current DNS evolution models, making it an important system for further investigation.

Acknowledgments

Writing my thesis has been a coffee-fueled blur, but I have many people to thank, in addition to the friendly staff at The Daily Grind who provided delicious Lattés and chocolate chip muffins that made this work possible. My advisors Duncan Lorimer and Maura McLaughlin involved me in every aspect of pulsar astronomy – from writing proposals to observing to data analysis – they focused my interests and helped me stay organized and on task. I am grateful for their generosity in inviting me to conferences all over the world where I worked with leading scientists in our field, made lasting friendships and built my network and knowledge base for future endeavors.

In the summer of 2010, when I arrived in West Virginia, I had the good fortune of helping out with a month-long Pulsar Search Collaboratory workshop in Green Bank, WV, where I met Sue Ann Heatherly, Rachel Rosen and Ryan Lynch. Sue Ann is a wizard when it comes to wrangling a group of high schoolers and has a contagious excitement about astronomy. I bonded with Rachel and Ryan during my first overnight GBT observing run and since then, they have answered countless “quick email" questions and provided advice about science, careers and life. They have been wonderful mentors and friends.

I have also thoroughly enjoyed getting to know Sarah Scoles, then Kathryn Williamson through the PSC; their senses of humor were a nice reprieve from days of wrangling high schoolers. Sarah and Kathryn also introduced me to Reva and Frank, two of the coolest dogs I know.

A huge thanks to my friends, colleagues and office mates: Pete Gentile, Fernando Cardoso, Lucas Hunt, Mehran Mohebbi, Akshaya Rane, Justin Ellis, Amy Sardone, Megan Jones and many others. We have been through a lot together – late nights in Hodges and White Hall, post-Weldon-exam beers, Mother India Fridays, roller chair races, *Taken* marathons, geocaching at Snake Hill, friends dinner. Grad school is not all about work.

Joel Weisberg, my undergraduate advisor at Carleton College, introduced me to pulsar astronomy. In addition to his long list of scientific accomplishments, Joel is an activist, he has a bizarre sense of humor and a huge heart. I am grateful for his advice and encouragement and pleased to meet other astronomers as kind and curious as Joel.

To Maura, Dunc and my other committee members, Loren Anderson, Paul Miller and Natalia Schmid – thank you for taking the time to read about my work and provide feedback. The end product has been greatly improved thanks to your input.

Mom, Papa and Suelyn, you may be some of the only others to actually read this thing, so thanks for that. Thank you for your love and support and for your genuine excitement about the work I'm doing. Tusen, tusen takk!

Finally, I've found that in trying to finish my dissertation while planning a wedding and a big move at the same time, it's nice to have someone else to take care of the wedding and the move. Sarah, I couldn't have done this without you. I love you and I'm excited to begin our life together this fall in Milwaukee.

Table of Contents

List of Figures

List of Tables

Chapter 1

Introduction

Pulsars are incredibly dense cores made primarily of neutrons that remain after supernova explosions of massive stars. They have rapid, extremely regular spin periods and strong magnetic fields. When their magnetic poles align with our line of sight as they rotate, we can detect faint intensity spikes called pulses with radio telescopes.

1.1 Historical Context

Now imagine the above statement in reverse. Starting with the radio pulses themselves, how does one connect observed, periodic signals with the rotations of exotic, cosmic objects as massive as our Sun, but only about 20 km across and spinning once every second?

1.1.1 In the beginning...

Jocelyn Bell was the first person to see such pulses after helping Anthony Hewish build a radio telescope for the purpose of observing scintillation (twinkling) of radio signals from distant objects called quasars. Every four days, she would make a map of the entire sky using a pen recorder; she collected 100 feet of chart data per day. “Occasionally," Bell recollected,[1] “in that 400 feet, there’d be a quarter inch of chart paper with a signal that I didn’t understand." Even after Jocelyn Bell managed to capture the signal on fast-recording chart paper in order to see that individual pulses were spaced evenly, by 1.33 seconds, the complete picture of pulsars as rapidly rotating, highly magnetized neutron stars was unclear. Hewish initially dismissed the signal as non-astrophysical radio frequency interference (RFI).

---

[1] Interview with Dame Jocelyn Bell-Burnell, *Little Green Men*.

Jocelyn Bell had noticed the offending “scruff" amidst her scintillation data for over a month prior to capturing the apparently periodic signal on fast-recording chart paper; she knew that every time it appeared, it came from the same part of the sky. Hewish was interested enough that he sat in on observations the next evening and right on cue, the mysterious pulses showed up again. “This is where our problems started," said Bell.[2]

Hewish et al. (1968) included a detailed treatment of Jocelyn Bell’s initial discovery and found three others like it. Still, the mechanism behind these “Rapidly Pulsating Radio Sources” was not understood. Despite the uncertainty surrounding the sources of emission, several clues could be gleaned from the pulses detected. First, based on the short pulse duration (0.016 s at any given frequency across a 1 MHz bandwidth), light travel time would suggest that the source must be less than about 5,000 km across. This is less than half the diameter of Earth. Second, the delays measured between the arrival times of pulses at different radio frequencies matched those one would expect for a signal traveling through a plasma of cold electrons, a major component of the interstellar medium (ISM). Assuming a constant electron density in the ISM along the line of sight provides a distance estimate to the source; in this case, the frequency delays implied a distance of just over 200 light years – outside the Solar System, but well within our Galaxy. Finally, the period between consecutive pulses could be measured with high precision, $P = 1.3372795 \pm 0.0000020$ s.

1.1.2 What are these cosmic clocks?

Over the following year, a flurry of theoretical papers tried to explain the precise “ticking” mechanism observed by Hewish et al. (1968). These papers considered three natural, clock-like processes involving vibrations, orbits or rotations.

Prior to the first pulsar discovery, Meltzer & Thorne (1966) showed that the minimum fundamental vibrational period of a white dwarf (WD) is 8 s and for a higher-density neutron star (NS), the maximum vibrational period is 10 ms. Since the radio pulses discovered had a period (~ 1.34 s)

---

[2] Interview with Dame Jocelyn Bell-Burnell, *Frozen Star* (Greenstein, 1983).

outside the range predicted for oscillating WDs or NSs, Hewish et al. (1968) invoked harmonics of fundamental vibrational modes to explain the discrepancy. Including elasticity in their calculations, Faulkner & Gribbin (1968) found that WD fundamental vibrational periods could be as low as 1.5 s, much closer to, but still above, the observed pulse period. Higher vibrational harmonics would still have to be invoked and there was no good explanation as to why the fundamental period would not be dominant. In April of 1968, Pilkington et al. (1968) reported the discovery of "Cambridge pulsed source" CP 0950, with a pulse period of ~ 0.25 s, decisively below predicted vibrational periods for WDs, but still above the range expected for NSs.

A binary system interacting such that once per orbit, radio emission would be directed towards Earth could also explain the mysterious radio pulsations observed. Using Kepler's Third Law and considering a small satellite orbiting a 1.0 M_0WD, the satellite would have to orbit at a distance of $\sim 1,800$ km in order to have an orbital period equal to 1.33 s, the pulse period observed by Hewish et al. (1968). In other words, to achieve such a short orbital period, the satellite would have to be practically skimming the surface of its companion WD! To explain shorter pulse periods with orbits, it makes more sense to consider a satellite orbiting a NS (~ 20 km in diameter) since shorter orbital periods require smaller orbital radii. The source CP 0950 (pulse period of ~ 0.25 s; Pilkington et al., 1968) would require an orbital separation of 600 km from a 1.0 M_0NS in order to be explained by orbits.

Ostriker (1968) pointed out that binary systems with orbital periods short enough to explain the observed radio pulses would give off significant amounts of gravitational radiation and thus, the orbital period would change rapidly. Observations over several weeks would easily detect such changes and yet, the pulse period of CP 1919 was stable to two parts per million over several months. To avoid the complication of obvious period changes over short time scales, the orbiting satellite would have to be small – less than $3 \times 10^{8}\ M_{O}$(Pacini & Salpeter, 1968). Furthermore, the satellite would have to withstand crushing tidal forces and high energy radiation from its NS companion.

Rotation was the third candidate mechanism considered as a possible means of generating regular radio pulses. Countering arguments that supported oscillating WD models, Gold (1968) wrote, “*Accuracies of one part in* 10^8 *belong to the realm of celestial mechanics of massive objects, rather than to that of plasma physics.*" The difficulty with a rapidly-rotating massive object however is its tendency to spin itself apart. This begins to happen when the centrifugal force exceeds the gravitational force on a test mass on the rotating object’s equator. If we were to propel the Earth such that it spun once every 1.4 hours, a person standing at the equator would be weightless. At higher speeds, buildings would crack at their foundations, Earth’s crust would dislodge and a disk of material would fling out from the equator. The Sun would experience a similar fate if it were to reach a spin period less than about three hours; white dwarfs could sustain spin periods of about a second; neutron stars, about a millisecond.

In October, Large et al. (1968) announced a possible association between a “pulsating source of radio," PSR B0833−45 and the Vela supernova remnant. In quick succession another pulsar was found in the Crab Nebula (Cocke et al., 1969). The Vela and Crab pulsars were the first to be found associated with supernova remnants and they had much more rapid pulse periods than previous discoveries – 89 ms and 33 ms respectively. Such rapid pulse periods put any remaining theories involving white dwarfs to rest, leaving rotating or binary neutron stars as the only plausible explanations.

After describing pulsars as highly-magnetized, rotating neutron stars producing beams of radio emission “like a light-house beacon," Gold (1968) concluded, “If this basic picture is correct, it may be possible to find a slight but steady slowing down of the observed repetition frequencies." In fact, Richards & Comella (1969) measured this spin-down a short three months after the Crab pulsar was discovered. The separation between orbiting bodies that emit gravitational radiation shrinks over time and therefore, the orbital period also gets shorter. A highly-magnetized rotating neutron star however emits magnetic dipole radiation and its spin slows over time (see §1.3.1).

In 1969, the Crab and Vela pulsars had by far the most rapid spin periods and were the only two sources known to be associated with supernova remnants; this connection was not lost on astronomers at the time, nor was it purely coincidence. Pulsars are born in supernova explosions, thus supernova remnants are byproducts of their birth, so the Crab and Vela pulsars must be young. Eventually supernova remnants disperse and older pulsars like CP 1919, the first pulsar discovered, outlive them. CP 1919 had no detectable spin-down over a year's observations; the Crab's comparatively significant spin-down measured by Richards & Comella (1969) solved the mystery of what produced the radio pulsations observed by Hewish et al. (1968), but it also gave the scientific community a snapshot of pulsar evolution. Young pulsars tend to have rapid spin periods, but also lose energy quickly – they spin down over time. Due to this spin-down, older pulsars tend to have longer spin periods, but do not spin down as quickly. In §1.3, I will further discuss the pulsar population, evolutionary processes and how far we have come since this first moment of clarity in 1969.

The fascinating history of the pulsar discovery process is summarized here, but more detailed accounts can be found in Greenstein (1983) and Lyne & Graham-Smith (1998). Maran & Cameron (1968) offer an interesting perspective, outlining the progression of theoretical arguments being considered to explain the observed radio pulsations just months after the first discovery paper.

1.2 Timing – the “Bread and Butter" of Pulsar Astronomy

Before discussing the wide variety of pulsars that have been observed, it is important to first understand the way in which we interpret the “ticks" of individual pulsars. Pulsars spin with extreme regularity and stability; much of what we learn from studying pulsars starts with the process of precisely time-tagging individual pulses or carefully summed series of pulses in order to compare times-of-arrival (TOAs) with a model, based on various parameters. The process of improving model parameters by “phase connecting" TOAs is called timing. We say that TOAs are phase connected by a given model if we have unambiguously accounted for every rotation before or after some reference time.

One of the first parameters measured from a new pulsar discovery is its spin frequency, f, which can be expressed as a Taylor expansion,

$$f(t) = f_0 + \dot{f}_0(t - t_0) + \frac{1}{2}\ddot{f}_0(t - t_0)^2 + \ldots, \tag{1.1}$$

where $f_0 = f(t_0)$, the spin frequency measured at reference time, t_0. Although they do so very slowly, pulsars eventually lose spin angular momentum and rotate less rapidly; therefore, physical $\dot{f}_0$ values are negative when measured over timespans of several months to a year (before then, spin-down is usually undetectable in most pulsars). Higher-order frequency derivatives ($\ddot{f}_0$, etc.) are usually only measurable for young pulsars, which exhibit relatively large fluctuations in spin parameters compared to the rest of the pulsar population. Integrating Equation 1.1 gives an expression for the number of rotations,

$$N(t) = N_0 + f_0(t - t_0) + \frac{1}{2}\dot{f}_0(t - t_0)^2 + \frac{1}{6}\ddot{f}_0(t - t_0)^3 + \ldots, \tag{1.2}$$

where $N(t_0) = N_0$, $f_0 = \dot{N}_0$ and higher derivatives of N_0 are expressed in terms of frequency derivatives. If you were able to hover in an inertial reference frame nearby a solitary pulsar you wished to study, Equation 1.2 would be completely sufficient for describing its pulses. Such an experiment would prove difficult however, since the nearest pulsar is over 500 light-years away and once there, you would need proper shielding from the intense radiation, high energy electrons and protons to survive.

1.2.1 Studying Pulsars from Earth

We are not in an inertial reference frame. The radio telescopes we use to observe pulsars are whirling around as the Earth rotates and meanwhile, Earth orbits the Sun and the Sun orbits the Solar System Barycenter (SSB), or center of mass. The SSB itself orbits our Galaxy, but it does so only once every 200 Myr, so for pulsar solutions that span months or years, the SSB is a good approximation for an inertial reference frame. Pulsar TOAs that are recorded at the observatory and time-tagged using a local atomic clock are called *topocentric* and these are converted to *barycentric* TOAs by applying time corrections of different magnitudes.

The most significant time correction arises due to a pulsar's position and the Earth's orbit around the Sun. For simplicity, assume the Earth's orbit is circular and consider a newly-discovered pulsar on the ecliptic plane in the constellation Sagittarius. We know that the light travel time between the Sun and the Earth is (1 AU)/c ″′ 500 s, so in December, when the Sun appears in Sagittarius, pulses arrive late at Earth compared to the SSB (near the Sun). In June, Sagittarius rises highest in the sky at midnight (the Earth is between the Sun and the pulsar), so the pulsar signal is observed on Earth ~ 500 s before it would reach the SSB. Still assuming Earth's orbit is circular, but now considering a pulsar with any given ecliptic latitude (β) and longitude (λ), the correction t_c is given by

$$t_c = A\cos(\omega t - \lambda)\cos\beta, \tag{1.3}$$

where A is the light travel time from the Sun to the Earth and ω is the Earth's orbital angular velocity. Because of this dependence on λ and β, applying the correct t_c goes hand in hand with refining pulsar position.

Another time correction is applied to account for the Earth's phase in its rotation; this correction can have a magnitude as large as the light travel time over the Earth's radius, $R_\oplus/c$ ″′ 21 ms. The full light travel time between the phase center of the radio telescope and the SSB is called the Römer delay, $\Delta_{\mathrm{R}O}$. Several factors in addition to $\Delta_{\mathrm{R}O}$ must be accounted for to convert topocentric TOAs (t_{topo}) to barycentric TOAs (t_{bary}):

$$t_{\mathrm{bary}} = t_{\mathrm{topo}} + t_{\mathrm{corr}} + t_{\mathrm{disp}} + \Delta_{\mathrm{R}O} + \Delta_{\mathrm{S}O} + \Delta_{\mathrm{E}O}. \tag{1.4}$$

TOAs are measured at the telescope – usually referencing a local hydrogen maser clock – and converted to Coordinated Universal Time (UTC), giving t_{topo}. UTC accounts for the Earth's nonuniform rotation[3] by occasionally adding leap seconds, so $t_{\rm corr}$ accounts for these discontinuities in order to convert $t_{\rm topo}$ to a smoother time standard, Terrestrial Time (TT).

The $t_{\rm disp}$ term in Equation 1.4 corrects for the observed signal's dispersion due to its path through cold, ionized plasma in the interstellar medium (ISM). Pulsars are "broad-band sources" – they produce multi-frequency emission spanning much of the electromagnetic spectrum. The dispersion delay, $t_{\rm disp} \propto f^{-2}$, where f is observing frequency; low frequency emission is delayed more than high frequency emission and $t_{\rm disp}$ vanishes for a signal at "infinite frequency." Therefore, infinite frequency serves as a convenient reference for all TOAs, regardless of the chosen observing frequency. Dispersion will be discussed in more detail in §1.4.

The last three delays in Equation 1.4 reference a Solar System *ephemeris* (e.g. DE405, published by Jet Propulsion Laboratory) since each one depends on precise locations of all major bodies in the Solar System. Introducing $\Delta_{\rm R\odot}$, no distinction was made between the Sun's position and the SSB (even though Jupiter is large enough that the SSB lies just outside the surface of the Sun); for $\Delta_{\rm R\odot}$, a Solar System ephemeris provides the means for pin-pointing the position of the SSB (center of mass) at any given time in order to properly apply light travel time delays to calculate the Römer delay. The Shapiro Delay ($\Delta_{\rm S\odot}$; Shapiro, 1964) accounts for time delays incurred by a pulsar signal traveling through curved spacetime due to massive objects in the solar system. The gravitational potential at the Earth changes as the Earth moves in an elliptical orbit around the Sun. The Einstein Delay ($\Delta_{\rm E\odot}$) quantifies the varying clock rate on Earth due to the changing gravitational potential, compared to a reference clock in a circular orbit. It also accounts for the time dilation due to the Earth's motion. Both $\Delta_{\rm S\odot}$ and $\Delta_{\rm E\odot}$ are effects predicted by General Relativity, while $\Delta_{\rm R\odot}$ is a classical correction.

---

[3] According to the International Earth Rotations and Reference Systems Service (IERS), variability is caused by gravitational torque exerted by the Sun, Moon and planets, displacement of matter in different parts of the planet and other excitation mechanisms.

1.2.2 Analyzing Barycentric TOAs

For a solitary pulsar, an initial timing solution would include position parameters (Right Ascension and Declination[4]), spin period, dispersion measure (DM) and a reference time (t_0 from equation 1.2), defining the 0th pulse. Achieving a “phase-coherent" timing solution requires unambiguously accounting for every rotation. Therefore, given the uncertainties on discovery parameters, it helps for timing follow-up observations to be closely-spaced early on so that these uncertainties do not exceed a pulse period from one observation to the next.

To begin, it helps to generate multiple TOAs per epoch so that we can phase connect over a single epoch first, then over multiple epochs. Fitting for refined model parameters, we express pulse number as a function of time as in Equation 1.2 and minimize the expression

$$\chi^2 = \sum_i \left(\frac{N(t_i) - n_i}{\sigma_i} \right)^2 . \tag{1.5}$$

Individual TOAs are indexed by i, n_i is the nearest integer to $N(t_i)$ and σ_i is a given TOA’s uncertainty in terms of fractional pulse period. Post-fit timing residuals are obtained by subtracting the model – with fit parameters that minimize Equation 1.5 – from observed TOAs. When an iteration of parameter fitting is successful, the resulting post-fit residuals should be “white" (Gaussian-distributed around zero; see Figure 1.2.2, panel *a*) and the root mean square (RMS) of the residuals should be comparable to TOA uncertainties; usually this means RMS $\sim 0.001 \times P$ for a pulsar with spin period P. It is also good practice to check that the post-fit parameter values are believable before proceeding (e.g., position has not changed by more than a beam width, period derivative is positive, etc.). Uncertainties on fit parameters in a coherent timing solution decrease as the length of the data span increases. Observing over multiple frequencies improves the dispersion measure (DM) uncertainty. Parameter uncertainties are estimated using covariance matrices that are computed during fits.

---

[4] Right Ascension, α, and Declination, δ are a projection of equatorial coordinates on the celestial sphere.

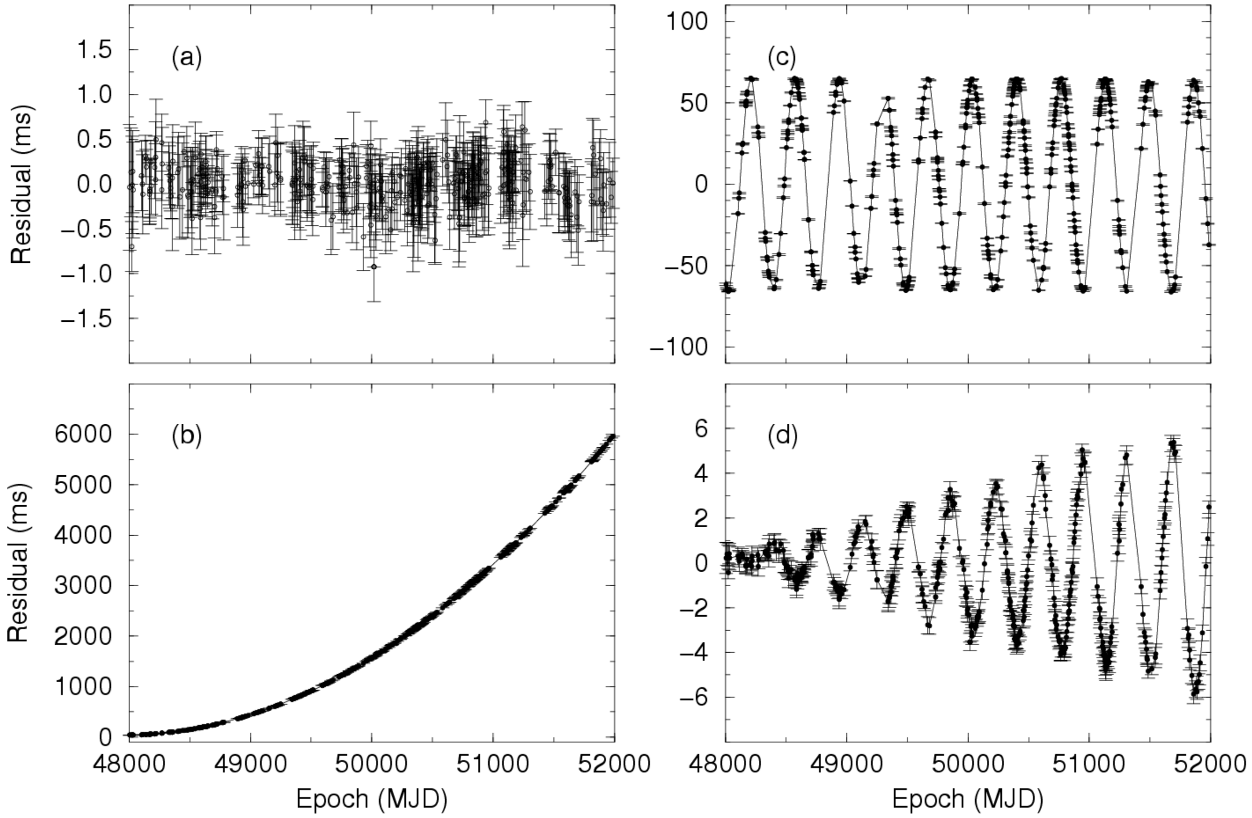

Figure 1.1: Timing residuals resulting from a good fit are Gaussian-distributed around zero or “white" (panel *a*); signatures in the residuals (panels *b*, *c* and *d*) arise due to unfit or incorrect timing model parameters. A quadratic signature in the residuals points to an incorrect spin period derivative (*b*), a sinusoid with an annual period (*c*) means that the pulsar position is incorrect and a similar sinusoid with a linear ramp over time (*d*) indicates that proper motion has not been accounted for. This figure is included with permission from Duncan Lorimer (Lorimer & Kramer, 2004).

Signatures in the residuals point to specific parameters that are poorly-determined or those that should be added to the timing solution in order to achieve a fully phase-coherent timing solution with white residuals (see Figure 1.2.2). For example, a model with an incorrect spin period will produce residuals that show a linear trend with a positive or negative slope, depending on whether the nominal spin period is too small or too large. A quadratic trend in the residuals means that a period derivative should be added to the timing solution and fit. If a pulsar's position is incorrect, the Römer delay will be applied incorrectly (see Equations 1.3 and 1.4), resulting in an annual sinusoid in the residuals. If a pulsar is moving on the sky, its position is changing and therefore, gets less and less correct – a pulsar's proper motion appears as an annual sinusoid that grows linearly over time.

A software package called Tempo[5] automatically converts a list of TOAs into t_{bary} (Equation 1.4), then performs a least squares fit (Equation 1.5) over specified parameters, given an initial timing solution. Tempo2[6] has similar functionality, but provides a GUI for visualizing pre/post-fit residuals (Hobbs et al., 2006).

1.3 The Pulsar Population

Pulsars are born in supernova explosions. Although neutron stars can result from several different types of supernovae, Type Ia supernovae are considered here for instructive purposes, assuming the progenitor core is composed entirely of iron and characteristic of a white dwarf. The star shrinks dramatically as it forms a neutron star – essentially a giant atomic nucleus – with a radius of ~10 km and weighing a billion tons per teaspoonful. This change in size is the largest factor contributing to the resulting pulsar's short spin period and strong surface magnetic field due to the conservation of spin angular momentum and magnetic flux, respectively.

Assuming uniform density and no mass loss, conservation of spin angular momentum deter-

---

[5] http://tempo.sourceforge.net/

[6] https://sourceforge.net/projects/tempo2/

mines the spin period of the resulting neutron star,

$$P_{\rm NS} = P_{\rm WD} \left(\frac{R_{\rm NS}}{R_{\rm WD}} \right)^2, \tag{1.6}$$

in terms of the original spin period of the white dwarf ($P_{\rm WD}$) and the ratio of NS and WD radii. In a similar example, Carroll & Ostlie (2006) calculate $R_{\rm WD}/R_{\rm NS} \sim 512$; assuming an initial progenitor spin period, $P_{\rm WD} = 1350$ s (the rotation period of white dwarf 40 Eridani B), Equation 1.6 gives $P_{\rm NS} \sim 5$ ms!

Magnetic flux through the star's surface will also be conserved in the transition from WD to NS. By ignoring the magnetic field's geometry, we can approximate this conservation law such that the resulting NS's magnetic field strength,

$$B_{\rm NS} = B_{\rm WD} \left(\frac{R_{\rm WD}}{R_{\rm NS}} \right)^2, \tag{1.7}$$

where $B_{\rm WD}$ is the progenitor's initial magnetic field strength and $R_{\rm WD}/R_{\rm NS}$ is the ratio of white dwarf and neutron star radii (~512). The largest magnetic field measured for a WD is about 5×10^8 G (10,000 Gauss = 1 Tesla). If such a WD were to go supernova, the resulting neutron star would have $B_{\rm NS} = 1.3 \times 10^{14}$ G. This result gives an approximate upper limit on the magnetic field strength of a new-born NS; as we will see in discussion that follows, pulsars typically have magnetic field strengths closer to 10^{12} G.

Somewhat astoundingly, two pulsar parameters – spin period and its derivative – are often adequate to determine how an individual source fits into the underlying population. To date, we have discovered $> 2,500$ pulsars and we have measured P and $\dot{P}$ values for about 2,000 of them; a $P - \dot{P}$ diagram with all currently-known pulsars is shown in Figure 1.3.1. Pulsar parameters have been taken from the most recent version of the ATNF catalog (Manchester et al., 2005, V1.53).[7]

---

[7] http://www.atnf.csiro.au/research/pulsar/psrcat

1.3.1 What does spin tell us about a pulsar?

Pulsars are rotation-powered sources. Classical Electrodynamics (Jackson, 1962) tells us that a rotating magnetic dipole will produce an electromagnetic wave at its angular velocity, Ω.[8] Assuming a pulsar's spin-down luminosity ($\dot{E} \equiv -I\Omega\dot{\Omega}$, its total power output) is due to magnetic dipole radiation, we find a differential equation that expresses the evolution of angular velocity,

$$\dot{\Omega} = -\left(\frac{2|m|^2\sin^2\alpha}{3Ic^3}\right)\Omega^3, \tag{1.8}$$

which depends on the pulsar's magnetic moment m, its moment of inertia I, and the angle α between its magnetic pole and rotation axis. Rearranging Equation 1.8 and solving for m, we can estimate the strength of a pulsar's magnetic field since $B \sim |m|/r^3$. Assuming the pulsar is an "orthogonal rotator" ($\alpha = 90^\circ$) and has a typical moment of inertia, $I = 10^{38}$ kg m^2, and radius, $R = 10$ km, we derive a simple expression for surface magnetic field strength,

$$B_{\rm surf} \simeq 10^{12}\,{\rm G}\left(\frac{\dot{P}}{10^{-15}}\right)^{1/2}\left(\frac{P}{\rm s}\right)^{1/2}. \tag{1.9}$$

This is a convenient form of the expression for $B_{\rm surf}$ since the vast majority of known pulsars have spin periods on the order of one second and period derivatives, $\dot{P} \simeq 10^{-15}$ s s^{-1} (see Figure 1.3.1). Recall, Equation 1.9 assumes that a pulsar's spin-down luminosity is *entirely* due to magnetic dipole radiation. We can relax this assumption and re-express Equation 1.8 in terms of spin frequency,

$$\dot{f} = -K f^n, \tag{1.10}$$

where K is a constant that encompasses the terms from Equation 1.8 in parentheses and a factor of $(2\pi)^{n-1}$ and n is called the *braking index*. Note that $n = 3$ for magnetic dipole braking alone. Expressing Equation 1.10 in terms of spin period ($\dot{P} = K P^{2-n}$), separating and integrating, we find

---

[8] There are three prominent conventions for expressing the rapidity of a pulsar's spin: spin period (P), spin frequency (f) and angular velocity (Ω). For clarity, $\Omega = 2\pi f = 2\pi/P$.

a pulsar’s age,

$$\tau = \frac{P}{(n-1)\dot{P}} \left[1 - \left(\frac{P_0}{P}\right)^{n-1}\right] \tag{1.11}$$

in terms of its current P and $\dot{P}$, its birth period (P_0) and braking index, n. As I mentioned at the end of §1.1.2, pulsars are born with short spin periods and large period derivatives, therefore it is reasonable to assume that $P_0 \ll P$ for most pulsars; as in Equation 1.9 we use $n = 3$ to define a pulsar’s *characteristic age*:

$$\tau_c \equiv \frac{P}{2\dot{P}} \simeq 15.8\ \mathrm{Myr} \left(\frac{P}{\mathrm{s}}\right)\left(\frac{\dot{P}}{10^{-15}}\right)^{-1}. \tag{1.12}$$

The take-away message here is that by making some basic assumptions about how pulsars lose rotational kinetic energy (e.g. $n = 3$ for pure magnetic dipole braking), we can get good estimates for magnetic field strength and age (Equations 1.9 and 1.12 respectively) with straightforward measurements of spin parameters P and $\dot{P}$. Pulsar spin parameters provide a source classification tool with fairly minimal timing follow-up requirements.

1.3.2 The $P-\dot{P}$ Diagram

Astronomers generally classify main sequence (MS) stars by using the Hertzsprung-Russell (HR) diagram, which plots stars’ surface temperatures versus luminosities, or equivalently, color versus absolute magnitude. Stars live out their MS lives, fusing hydrogen into helium in their cores. Massive stars appear blue and have high surface temperatures and luminosities, while low-mass stars appear red. Therefore, based on a star’s temperature and luminosity, we can infer its mass and mass tells us everything. From a star’s mass, we can estimate the amount of hydrogen available to burn and therefore, its expected lifetime on the MS. Mass also gives us the expected path (in temperature–luminosity phase space) the star will take to become a red giant in its post-MS life. Finally, mass allows us to predict whether the star will become a white dwarf ($M_* \lesssim 8\ M_\odot$), a neutron star ($8\ M_\odot \lesssim M_* \lesssim 15\ M_\odot$) or a black hole ($M_* \gtrsim 15\ M_\odot$). A more detailed discussion

Figure 1.2: The $P - \dot{P}$ diagram is a log-log plot of measured spin periods versus period derivatives; this plot shows the current sample of $\sim 2,000$ known pulsars with measured P and $\dot{P}$. Lines of constant surface magnetic field strength (B_{surf}; see Equation 1.9) are dashed, lines of constant characteristic age (τ_c; Equation 1.12) are dot-dashed and lines of constant spin-down luminosity are dotted. For all calculations, typical values for a pulsar's moment of inertia (I = 10^{38} kg m^2), radius ($R = 10$ km) and $\alpha = 90^\circ$ are assumed. Equation 1.13 describes the functional form of the death line.

of the final stages of stars' post-MS lives will be relevant for describing pulsar evolution (§1.3.3). Suffice it to say, the HR-Diagram is a powerful tool used by astronomers to classify and understand MS stars based on easily-measurable parameters; for pulsar astronomers, the $P-\dot{P}$ diagram (see Figure 1.3.1) is its analog.

Section 1.3.1 emphasizes the importance of a pulsar's spin parameters; Equations 1.9 and 1.12 define lines of constant surface magnetic field strength and characteristic age in Figure 1.3.1. Unlike stars on the MS however, pulsars move across the $P-\dot{P}$ diagram as they lose rotational kinetic energy due to magnetic dipole radiation; their spin parameters change. Equation 1.11 allows us to plot a course for how a pulsar with an initial spin period and braking index can be expected to traverse $P-\dot{P}$ phase space, but simply plotting a large sample of pulsars gives us a snapshot of the full range of evolutionary possibilities and sub-populations. Early pulsar astronomers had an inkling towards this line of thinking when they used the Crab and Vela pulsars, both associated with supernova remnants (SNRs), to deduce that pulsars were born with short spin periods and large period derivatives. Other pulsars discovered at the time were older; there were no other SNR associations (they had long since dispersed), their spin periods were significantly longer and period derivatives, small enough that they were not yet measurable.

Indeed, *young pulsars* appear near the top of the $P-\dot{P}$ diagram. They typically have $P \sim 0.1$ s and $\dot{P} \sim 10^{-13}$ s s^{-1} with moderate to high surface magnetic field strengths and most of them have SNR associations. The youngest pulsars known have characteristic ages of $\sim 1,000$ years – the supernova that created the Crab pulsar was actually observed as a "guest star" (transient object) by Chinese astronomers in 1054 A.D. "Anomalous X-ray pulsars" (AXPs) have particularly strong magnetic fields and exhibit pulsed X-ray emission with no corresponding radio emission; otherwise all sources plotted in Figure 1.3.1 show pulsed radio emission.

As pulsars age, they move along lines of constant magnetic field strength (assuming no decay) towards longer spin periods and smaller period derivatives. The bulk of the pulsar population (~80%) is made up of solitary, *normal pulsars* (A.K.A. canonical or vanilla pulsars) that have

$P \sim 1$ s and $\dot{P} \sim 10^{-15}$ s s^{-1}. Although most normal pulsars have similar spin parameters, statistical analysis of their profiles, polarization properites, spectra and proper motions provide valuable information about pulsar emission physics, the interstellar medium and the underlying pulsar population.

Averaged pulse shapes (profiles) can vary wildly among pulsars, but normal pulsars tend to have relatively short duty cycles (the fraction of time during their spin periods when pulsars produce radio emission along our line of sight), $\delta_{\mathrm{Normal}} \sim 0.06$ (Lorimer et al., 2006b). The shapes of averaged pulse profiles and their degree of polarization allow us to study pulsars' emission properties and geometry. Rotation measures – Faraday rotation of linearly-polarized emission – provide a probe of the Galactic magnetic field. Pulsar dispersion measures probe electron content in our Galaxy and allow us to model electron density in the ISM (Cordes & Lazio, 2002). Ensemble studies of pulsar proper motions allow "ballistics tests," tracing sources back to their birthplaces in the Galaxy (Chatterjee et al., 2009) and determining the magnitudes of their supernova kicks (Hobbs et al., 2005). Finally, an accurate census of detections from different pulsar surveys provides information necessary to calculate the size of the underlying Galactic pulsar population (Lorimer et al., 2006b; Faucher-Giguère & Kaspi, 2006; Swiggum et al., 2014, and see Chapter 2 of this thesis.).

Depending on their magnetic field strength, normal pulsars will continue to produce radio emission for 10 Myr to 1 Gyr. The "death line" (see Figure 1.3.1) marks the point at which radio emission theoretically switches off and pulsars enter the "pulsar graveyard." Theoretical models that calculate the precise moment radio emission turns off depend heavily on a pulsar's magnetic field strength and structure, but they are well-approximated by

$$\left(\frac{\dot{P}}{10^{-15}}\right)\left(\frac{P}{\mathrm{s}}\right)^{-3} \simeq 2.9 \times 10^{-2}, \tag{1.13}$$

corresponding to a spin-down luminosity of $\sim 1.15 \times 10^{30}$ erg/s, about 3,000 times smaller than the Sun's luminosity (Bhattacharya et al., 1992).

So far, I have presented a picture of pulsars that are born with rapid spin periods and large period derivatives and these objects spend their lifetimes spinning down more and more slowly towards longer periods, until they cross the death line, at which point their radio emission mechanism shuts off. How then do we reconcile the distinct population of pulsars in the lower left corner of the $P-\dot{P}$ diagram (Figure 1.3.1)? Just as early pulsar astronomers recognized the evolutionary implications of short-period pulsars associated with supernova remnants, the fact that the vast majority of objects in the lower left corner of the $P-\dot{P}$ diagram are in binary systems is no coincidence; rather, it defines the evolutionary history of these pulsars.

The fastest-spinning pulsars are called *millisecond pulsars* (MSPs), which are broadly defined as having spin periods $P < 30$ ms (although often shorter by an order of magnitude) and period derivatives, $\dot{P} \sim 10^{-19}$ s s^{-1}. MSPs and objects with slightly longer spin periods that bridge the gap between the normal pulsar and MSP populations are called *recycled* pulsars, named after the process by which all pulsars in the lower left corner of the $P-\dot{P}$ diagram gain their particularly short spin periods, “recycling."

1.3.3 The 3 Rs: Resurrected, Rapid, Recycled! (Binary Pulsar Evolution)

High-mass MS stars burn through their fuel more quickly than low-mass stars, therefore in a binary system with two massive MS stars, the more massive one will evolve off the MS first. In this situation, we refer to the more massive star as the *primary* and the less massive, the *secondary*. The full range of evolutionary possibilities that follow are outlined in Figure 1.3.2. If the primary is sufficiently massive, it will undergo a supernova explosion and usually, the system will disrupt as a result of sudden mass loss and/or a kick due to asymmetries in the explosion. Only about 10% of binary systems will survive the primary star’s supernova explosion (Bailes, 1989); the low survival rate partially explains the small percentage of discovered pulsars that have binary companions (� 10%). Systems that are disrupted will result in a solitary young pulsar and a “runaway OB star" (Blaauw, 1961), both with high velocities.

Systems that survive the primary supernova explosion consist of a young or normal pulsar

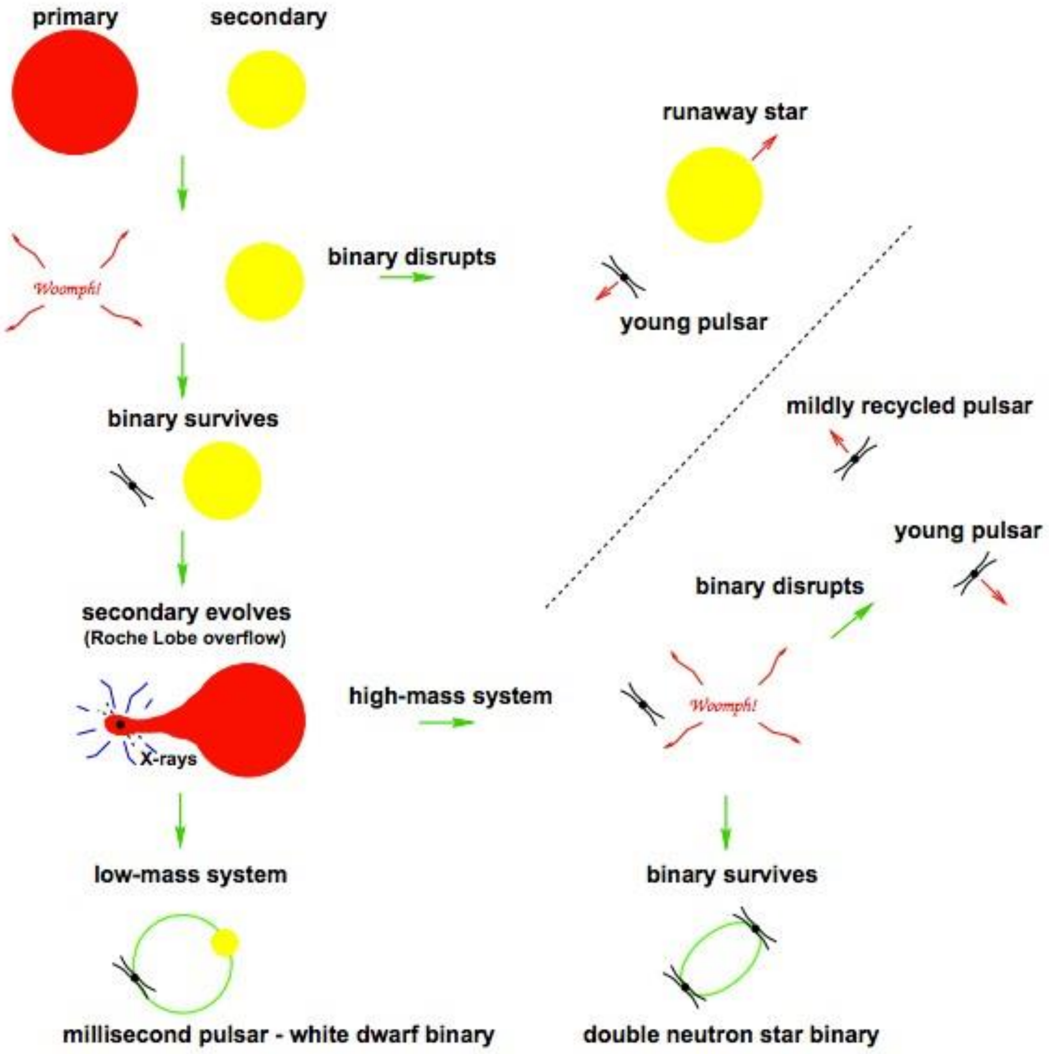

Figure 1.3: A cartoon depiction of the diverse range of systems that can result from binary pulsar evolution. This figure is included with permission from Duncan Lorimer (Lorimer, 2008).

orbiting a MS companion with high eccentricity due to their violent formation scenario. We know of four such systems (Johnston et al., 1992; Kaspi et al., 1994; Stairs et al., 2001; Lorimer et al., 2006a), all of which have young pulsars with low characteristic ages (Equation 1.12) that show no sign of spin-up. As its companion remains on the MS, the pulsar will spin down – in some cases, it will cross the death line (Equation 1.13; see Figure 1.3.1) and cease radio emission before the end of its companion's MS lifetime. As the secondary evolves off the MS and becomes a red giant, its outer layers expand and overflow its Roche lobe such that the pulsar begins to accrete material dispelled from its companion. Accreted material carries angular momentum that is transferred to the pulsar, decreasing its spin period and resurrecting the NS from the pulsar graveyard. The transfer of angular momentum through accretion from a binary companion is called *recycling* (Alpar et al., 1982a). The recycling process is accompanied by X-ray emission due to frictional heating from infalling matter. Although some recycled pulsars have spin periods similar to young pulsars, they have much lower period derivatives (see Figure 1.3.1).

The mass of the secondary determines what happens next. A High-Mass X-ray Binary (HMXB) will form a common envelope during Roche lobe overflow, the orbital separation between the pulsar and secondary will shrink and the orbit will circularize. Eventually, when the secondary's outer layers are dispelled, a helium star remains orbiting the primary NS. In the final stages of stellar evolution, before the secondary undergoes its own supernova explosion, a brief ($\sim 10^4$ years; Alpar et al., 1982b) period of mass transfer (recycling) takes place during which the pulsar is spun up. As with the primary supernova, the system has a low probability of survival when the secondary explodes, but if it does remain intact, the end product of this evolutionary branch is a *double neutron star* (DNS) system. DNS systems are characterized by short orbital periods and high eccentricities and primary pulsars in these systems tend to have spin periods between $10-100$ ms due to their brief recycling periods. Secondary pulsars in DNS systems have longer spin periods, not having undergone recycled. The double pulsar J0737−3039 A/B (Burgay et al., 2003) provides a nice example of the stark contrast between spin periods of the recycled primary ($P_A = 22.7$ ms) and the non-recycled secondary ($P_B = 2773.5$ ms). DNS systems will be discussed in more detail in Chapter 4 of this thesis, as well as the discovery of a new long-period primary DNS pulsar, J1930−1852, which has an unusually wide orbit.

In the more likely case that the HMXB is disrupted by the secondary's supernova explosion, two isolated pulsars with high velocities result – a young pulsar and a *disrupted recycled pulsar* (DRP). Since binary systems are more likely to disrupt than remain intact, one would expect to find many more DRPs than DNS systems, however roughly equal number of DRPs and DNSs have been found (Belczynski et al., 2010). A new DRP, J1821+0155, is discussed in Chapter 3.

Finally, in the case of Low-Mass X-ray Binary (LMXB) systems, the recycling process takes place over a much longer period of time – up to 10^8 years (Lorimer & Kramer, 2004) – and the primary can reach a spin period of several milliseconds by accreting matter from its companion. During this process, the orbit tends to shrink and circularize due to a combination of frictional and tidal effects. Not massive enough to undergo a supernova explosion, the secondary releases its outer layers to complete its stellar evolutionary process and a NS-WD system remains. The majority of MSPs ($P \sim 0.003$ ms, $\dot{P} \sim 10^{-20}$; see Figure 1.3.1) emerge from this evolutionary scenario; they tend to have low-mass WD companions and nearly circular orbits.

1.3.4 MSP Application: Pulsar Timing Arrays

MSPs rotate very regularly, spinning down far more slowly than their normal pulsar counterparts; they typically do not emit giant pulses, exhibit timing glitches or null – behavior observed mainly in young/normal pulsars that would hinder high-precision timing; their rapid rotation allows us to more precisely measure properties intrinsic to the pulsar system, which makes MSPs the best candidates for Pulsar Timing Arrays (PTAs), used for detection of gravitational waves (GWs). By regularly monitoring these pulsars, we hope to measure small, correlated deviations in their collective timing residuals in order to make a direct detection of GWs (Jenet et al., 2005).

PTAs consist of the fastest rotating, brightest and most stable MSPs in our Galaxy, distributed across the sky. PTAs are sensitive to low-frequency GWs (10^{-9}–10^{-7} Hz; waves with frequencies of about one cycle per year, or wavelengths of about 1 pc), which nicely complements other gravitational wave detectors like space-based interferometers (e.g. eLISA) and ground-based interferometers (e.g. LIGO) – both of which are sensitive to successively higher frequencies in the GW *spectrum*. The North American Nanohertz Observatory for Gravitational Waves (NANOGrav) partners with the Parkes Pulsar Timing Array (PPTA) and European Pulsar Timing Array (EPTA) to make up the International Pulsar Timing Array (IPTA) in a “coopetition" to make the first direct detection of gravitational waves.

Unlike other GW experiments, our PTA “detectors" consist of components (MSPs) that we cannot move, improve upon or have any interaction with directly. Therefore, a majority of PTA efforts consist of modeling imperfections in our MSPs such as red spin noise, ISM effects (scintillation, scattering, time variable dispersion), and pulse jitter so that we can mitigate their effects as we try to make an initial GW detection. By correcting for all of these effects, we improve (decrease) the RMS timing residuals ($\sigma_{\rm RMS}$) for individual MSPs. In our current sensitivity regime, now that many of our MSPs have $\sigma_{\rm RMS} < 200$ ns (Arzoumanian et al., 2015), the signal-to-noise ratio of the stochastic GW background with GW amplitude (A) scales like

$$N_{\rm MSP} T^{1/2} \quad A/(\sigma_{\rm RMS}\sqrt{C})^{3/13}, \tag{1.14}$$

where $N_{\rm MSP}$ is the number of MSPs in the PTA, T is the total observing timespan and C is the observing cadence, the inverse of time between observations (McLaughlin, 2014). In other words, we have reached a sensitivity regime for the stochastic background that scales much more strongly with $N_{\rm MSP}$ than $\sigma_{\rm RMS}$ (Siemens et al., 2013), suggesting that finding more (suitable) MSPs is very important.

1.3.5 Population Modeling

Pulsar population modeling for simulation purposes is typically done using one of two standard techniques. The first simulates sources by choosing birth periods and period derivatives from

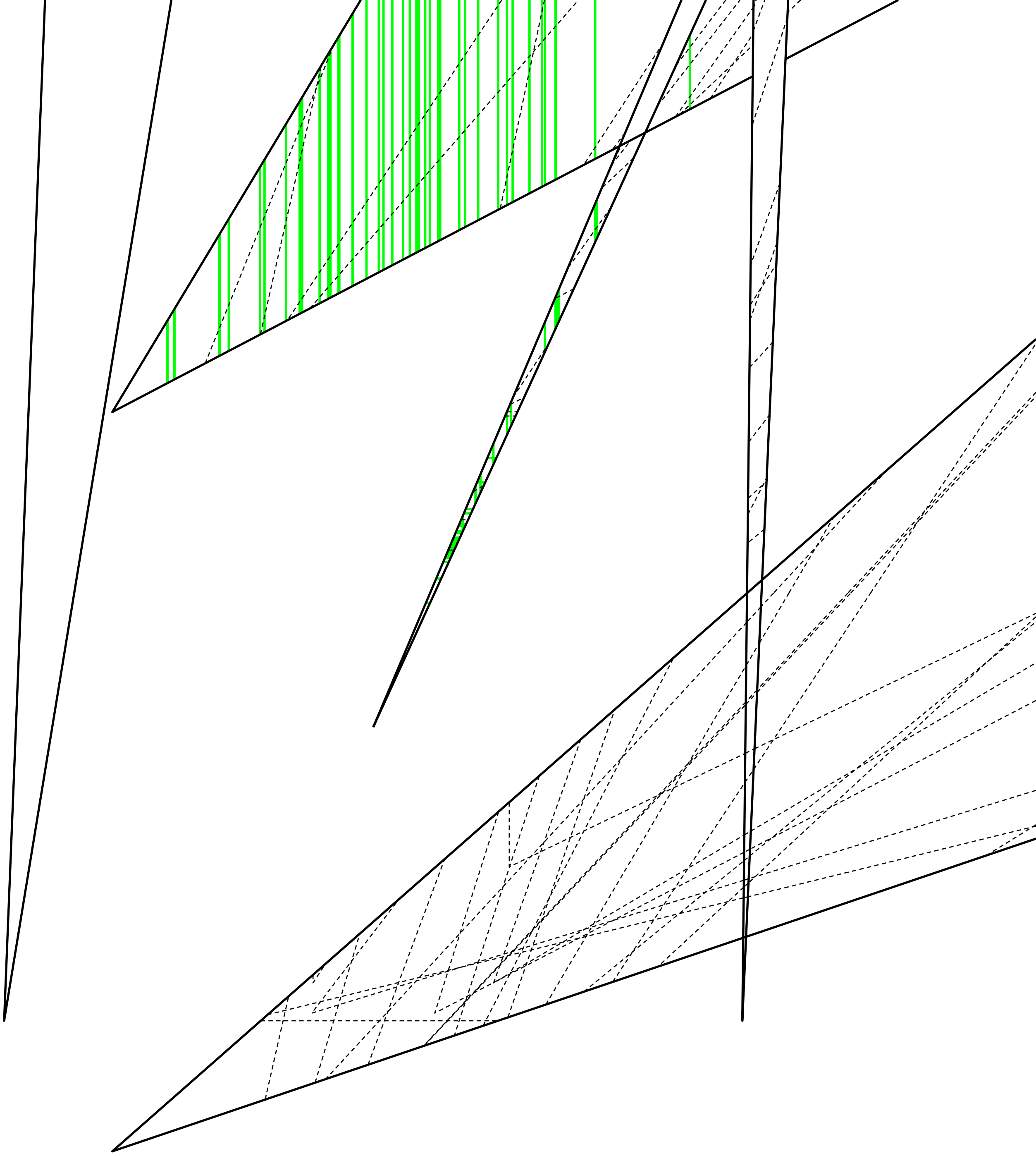

Figure 1.4: Sky maps of the Galactic normal pulsar (top) and MSP (bottom) populations. Only pulsars in the Galactic field are included here. Pulsars found in globular clusters and in the Small and Large Magellanic Clouds have been excluded. A simple spin period cut-off differentiates between millisecond and normal pulsar populations ($P_{\mathrm{MSP}} < 0.03$ s $< P_{\mathrm{Normal}}$).

modeled distributions and evolves them forward in time to the present day (e.g., Faucher-Giguère & Kaspi, 2006). A second technique called the “snapshot" method relies on a statistical analysis of the current, known pulsar population to inform parameter selection (e.g., Lorimer et al., 2006b). Modeled pulsar populations are commonly used to predict pulsar survey yields; for this application, period derivatives are not necessary, so the discussion that follows is limited to the snapshot method, but software to use either method is readily available (Bates et al., 2014).[9,10]

Lorimer et al. (2006b) did the most comprehensive analysis of normal pulsar population parameters to date, using a sample of 1,008 solitary, non-recycled sources discovered by the Parkes Multibeam Pulsar Survey (PMPS) and other Parkes Multibeam surveys using an identical observing set-up. Many of the parameter distributions used to generate synthetic normal pulsars come from models that Lorimer et al. (2006b) found to be good fits when applied to the 1,008-pulsar sample of PM survey discoveries. For example, the radial density of pulsars in the Galaxy is best modeled with a gamma function, while the density of pulsars perpendicular to the plane (in the *z*-direction) is given by an exponential with scale height of 330 pc. The top panel of Figure 1.3.4 shows the current distribution of all known normal pulsars in Galactic coordinates; pulsars are strongly concentrated in the plane, as the scale height measurement suggests.

Since normal and millisecond pulsars have very different sets of typical parameters, we model the two populations separately. The bottom panel of Figure 1.3.4 shows the spatial distribution of MSPs in the Galaxy, which is much more diffuse than that of the normal pulsar population. The scale height for MSPs is 500 pc (Lorimer, 1995; Levin et al., 2013) and the radial density distribution, best modeled by a Gaussian with a standard deviation of 7.5 kpc (Lorimer, 2013).

Normal and millisecond pulsar populations have spin period distributions that are well-described by log-normal distributions,

$$N(\log P) = A \exp \quad -\frac{(\log P - \mu)^2}{2\sigma^2} \quad , \tag{1.15}$$

---

[9] http://psrpop.sourceforge.net/

[10] https://github.com/samb8s/PsrPopPy

where A, μ and σ give the amplitude, mean and standard deviation of the distributions respectively. The normal pulsar population follows a Gaussian distribution in $\log P$ like the one described by Equation 1.15 with $A = 0.52(1)$, $\mu = 2.70(1)$ and $\sigma = 0.34(1)$ (Lorimer et al., 2006b). Notice that $10^{\mu} \sim 500$ ms is the mean pulse period for normal pulsars. Recently, Lorimer et al. (2015) have found $\mu = 1.5(2)$ and $\sigma = 0.58^{+0.12}_{-0.09}$ for the MSP population, fitting a log-normal distribution to a sample of 56 MSPs found by Parkes Multibeam surveys. We model pulse width following the empirical expression for pulsar beam opening angle (inversely related to pulse period) introduced by Kramer et al. (1998), then randomly select an impact parameter β and magnetic inclination angle α (e.g., Smits et al., 2009) to calculate width, W.

Finally, Faucher-Giguère & Kaspi (2006) describe the pulsar luminosity distribution with a log-normal function with mean and standard deviation $\mu = -1.1$ and $\sigma = 0.9$ in log-10 space. With this luminosity function, Faucher-Giguère & Kaspi (2006) estimated 120,000 potentially observable (radio-loud and beaming at Earth) in the Galaxy. The same luminosity function is used for modeling the MSP population; contrary to previous assumptions, Bagchi (2013) showed that luminosities of recycled pulsars in globular clusters followed the same distribution. The predicted population size of potentially detectable MSPs is smaller than for normal pulsars, but still quite uncertain – likely between 15,000 and 100,000 (Levin et al., 2013; Swiggum et al., 2014, and see Chapter 2 of this thesis).

In order to combine and make use of all of this information, we populate the Galaxy with synthetic sources, until reaching the predicted number of potentially detectable sources. Pulsar parameters like spin period, pulse width, Galactic position, etc. are selected at random from modeled distributions, then we find the synthetic pulsar's distance from Earth to calculate its flux (given luminosity) and its dispersion measure (integrating along the line of sight and using the Cordes & Lazio (2002) model for free electrons in the Galaxy. A survey's sensitivity can be calculated from its observing parameters (see §1.4) in order to simulate its performance (number of detections).

1.4 Sensitivity and Pulsar Surveys

Over 2,500 pulsars have been discovered to date by $\sim$ 30 major pulsar surveys (Manchester et al., 2005)[11] and over 1,000 of these were discovered by the Parkes Multibeam Pulsar Survey (PMPS) using the Parkes Radio Telescope in Australia. Designing a new pulsar survey means deciding on a telescope and an accessible region of sky to cover, a center frequency, sampling time, channel bandwidth and dwell times for individual pointings. This section describes how each of these choices affects survey sensitivity and how these parameters can be used to estimate a new survey's performance.

Unlike telescopes sensitive to emission in other parts of the electromagnetic spectrum that use detectors to image a region of sky, single dish radio telescopes have a single, low-resolution pixel on the sky with greatest sensitivity on-axis. The beam sensitivity drops off as a function of angular radius and the sensitivity pattern is well-approximated by a Gaussian function centered on the beam's axis. The beam's angular width at half power $\theta_{\rm FWHM} \sim \lambda/D$, where λ is the wavelength of light being observed ($f = c/\lambda$), D is the effective telescope diameter and $\theta_{\rm FWHM}$ is given in radians. The Green Bank North Celestial Cap survey uses the Green Bank Telescope (GBT; $D \sim 100$ m) to survey the sky at 350 MHz, therefore this pulsar survey has a beam width (resolution) of $\theta_{\rm FWHM} \sim 0.5^\circ$, about the size of the full moon. For the Pulsar Arecibo L-band Feed Array (PALFA) survey, which uses the 300 m Arecibo Observatory to survey the sky at ~ 1.4 GHz, $\theta_{\rm FWHM} \sim 3.35'$.[12] GBNCC's beam is about 10 times wider! When it comes to survey efficiency (covering large areas of sky in relatively little time), smaller telescopes at lower frequencies will cover the sky more quickly than large telescopes at high frequencies.

---

[11] http://www.atnf.csiro.au/people/pulsar/psrcat/download.html

[12] To convert between degrees and arcminutes, $1^\circ = 60'$.

Survey Parameters	AO Drift	GBNCC	GBT 820 MHz	PALFA (Mock)	PMPS	HTRU North (Low-lat)
Sky Coverage	$0^\circ < \delta < 38^\circ$	$\delta > -30^\circ$	$75^\circ < l < 94^\circ$ $-3^\circ < b < 6^\circ$	$32^\circ < l < 77^\circ$ $168^\circ < l < 214^\circ$ $\|b\| < 5^\circ$	$-100^\circ < l < 50^\circ$ $\|b\| < 5^\circ$	$\delta > 0^\circ$ $\|b\| < 3.5^\circ$
Telescope	Arecibo	GBT	GBT	Arecibo	Parkes	Effelsberg
Diameter (m)	300	100	100	300	64	100
θ_{FWHM} (arcmin)	16.5	36	15	3.35	14	9.7
Sampling Time (μs)	256	81.92	64	64	250	54
System Temperature (K)	100	23	22	24	25	20
Center Frequency (MHz)	327	350	820	1374	1374	1400
Bandwidth (MHz)	25	100	200	322	288	300
Channel Bandwidth (MHz)	0.0488	0.0244	0.0977	0.34	3.0	0.586
Number of Channels	512	4096	2048	1024	96	512
Gain (K/Jy)	10	2	2	~8.5	0.6	~1.5
Integration Time (s)	50	120	270	Inner Galaxy: 268 Outer Galaxy: 134	2100	1500
S_{min} (mJy)	0.44	0.47	0.12	0.025	0.12	0.045
$N_{\mathrm{discovered}}$	62	110	—	152	833	—

Table 1.1: Parameters of six major pulsar surveys. S_{min} values correspond to minima from Figure 1.4. The number of discoveries listed for each survey includes both normal pulsars and MSPs at the time of writing. The HTRU-North low latitude and GBT 820 MHz surveys have not yet commenced, so $N_{\mathrm{discovered}}$ has been left blank for these surveys.

Larger telescopes collect many more photons at a time, and therefore, are more sensitive than smaller telescopes. A telescope's sensitivity is most directly related to its effective collecting area (A_e), which is proportional to its *gain* ($G = A_e/2k$).[13] Table 1.1 lists gain values for four different large radio telescopes, showing the clear relationship with collecting area. The minimum detectable source flux density (in mJy[14]) per pointing for a given survey,

$$S_{\rm min} = \beta \frac{(S/N)_{\rm min} T_{\rm sys}}{G\sqrt{n_p t_{\rm int} \Delta f}} \sqrt{\frac{W}{P-W}}, \tag{1.16}$$

where β is a degradation factor due to digitization, n_p is the number of polarizations (usually 2), $t_{\rm int}$ is integration time – time spent observing a given sky position – in seconds and Δf is the bandwidth (MHz). The last term in Equation 1.16 accounts for pulsed (rather than continuous) emission, where P is a source's pulse period and W, its pulse width, both in units seconds. Somewhat arbitrarily, $S_{\rm min}$ usually corresponds to a chosen detection threshold, $(S/N)_{\rm min} = 9$. Finally, system temperature ($T_{\rm sys}$) is the sum of several factors,

$$T_{\rm sys} = T_{\rm CMB} + T_{\rm rec} + T_{\rm sky} + T_{\rm source}. \tag{1.17}$$

Here $T_{\rm CMB} = 2.7$ K is the system temperature contribution from the Cosmic Microwave Background; the receiver's noise temperature contribution is denoted by $T_{\rm rec}$, which varies by telescope and observing frequency, but often, $20\ \mathrm{K} \lesssim T_{\rm rec} \lesssim 100\ \mathrm{K}$; background $T_{\rm sky}$ due to synchrotron emission in the Galaxy depends heavily on both observing frequency and sky position as is clear from Figure 1.4; the source contribution, $T_{\rm source}$, is usually a small fraction of the overall system temperature. At 350 MHz, the background sky temperature is hundreds of Kelvin almost anywhere along the Galactic plane, making low-frequency surveys fairly useless there – like trying to find faint stars by eye during the day. Since background $T_{\rm sky} \propto f^{-2.6}$ (Haslam et al., 1982), higher-frequency surveys cope much better with diffuse radio emission in the Galactic plane and can retain low $S_{\rm min}$.

---

[13] The Boltzmann constant, $k = 1.38064852 \times 10^{-23}$ m^2 kg s^{-2} K^{-1}.

[14] The *Jansky* is a unit of flux density; 1 Jy = 10^{-26}W m^{-2} Hz^{-1}.

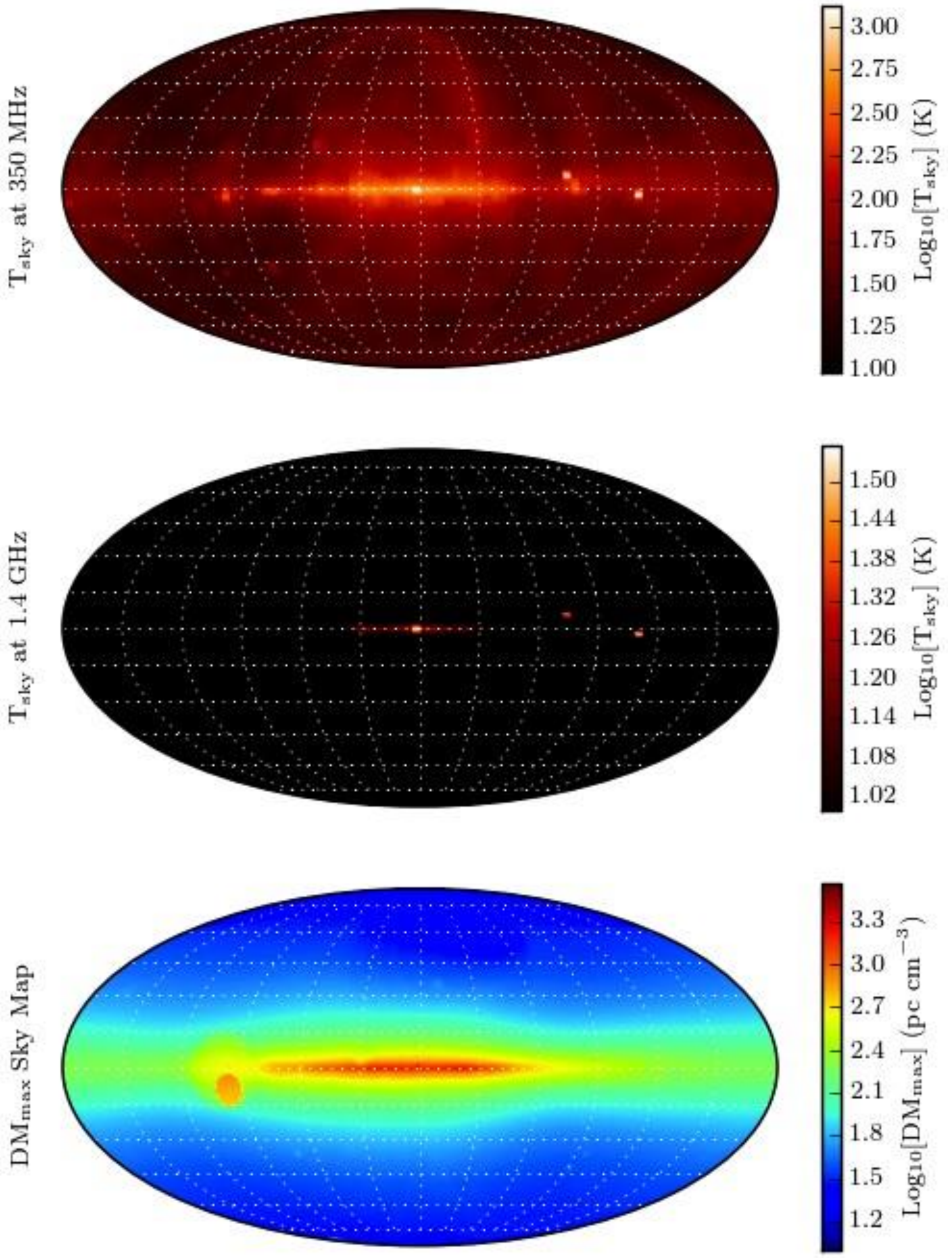

Figure 1.5: Sky maps plotted in Galactic coordinates of background T_{sky} at 350 MHz and 1.4 GHz (Haslam et al., 1982) and maximum dispersion measure (DM) along the line of sight (Cordes & Lazio, 2002).

The third sky map in Figure 1.4 shows maximum dispersion measures (DMs) along any line of sight, using the Cordes & Lazio (2002) model for Galactic electron content. DM is simply a measure of the electron column density along the line of sight to a source at distance d,

$$\mathrm{DM} = \int_0^d n_e \, d\ell, \tag{1.18}$$

where n_e represents the electron number density and $d\ell$ is the differential length along the line of sight. Section 1.2.1 introduced the idea that t_{disp} (Equation 1.4) needs to be accounted for in order to combine multi-frequency data into one timing solution since dispersion induces frequency-dependent delays on radio signals traveling through the ISM. Specifically, $t_{\mathrm{disp}} \equiv D \times \mathrm{DM}/f^2$ – where D is the dispersion constant[15] – relative to a signal of infinite frequency. Dispersion delays can also smear out a pulsar's signal over a bandwidth Δf, since the low frequencies in the band will be delayed relative to the high frequencies. Usually these delays are accounted for by dedispersing survey data before employing search algorithms using closely-spaced trial DMs. On an even smaller scale, dispersion delays,

$$t_{\mathrm{DM}} \approx 8.3 \times 10^6 \ \mathrm{ms} \times \mathrm{DM} \times \Delta f_{\mathrm{chan}} / f^3 \tag{1.19}$$

smear signals over individual frequency channels, where Δf_{chan} is a survey's frequency channel bandwidth (MHz) and f is the survey's center frequency (MHz). These delays can not be corrected and add in quadrature with a pulsar's intrinsic pulse width (W_{int}), effectively smearing the observed pulse width,

$$W = \sqrt{W_{\mathrm{int}}^2 + t_{\mathrm{DM}}^2 + \tau_s^2} \tag{1.20}$$

by a small amount. The third term in Equation 1.20 (τ_s) arises due to scatter-broadening of a pulsar's signal as it travels through the ISM. If a pulsar emits a sharp single pulse, multi-path scattering causes some of that emission to arrive systematically late, so the observed, scatter-broadened pulse

---

[15] $D \equiv e^2/(2\pi m_e c) = (4.148808 \pm 0.000003) \times 10^3 \ \mathrm{MHz}^2 \ \mathrm{pc}^{-1} \ \mathrm{cm}^3 \ \mathrm{s}$.

Figure 1.6: Sensitivities as a function of spin period for the pulsar surveys listed in Table 1.1. The AO Drift and GBT 820 MHz surveys have been omitted because they have $S_{\rm min}$ values similar to the GBNCC survey and PMPS respectively. The bottom-most portion of each survey's colored sensitivity curve is calculated using a trial dispersion measure, $\mathrm{DM}_{\rm low} = 50$ pc cm^{-3} and the top-most part of each curve uses $\mathrm{DM}_{\rm high} = 150$ pc cm^{-3}. The black dashed line gives each survey's sensitivity, considering a test source with DM = 100 pc cm^{-3}.

will have an exponential tail with a scattering timescale, τ_s. Bhat et al. (2004) measured τ_s for 98 pulsars and fit the data to a parabola in log(DM), resulting in the empirical relationship,

$$\log \tau_s = -6.46 + 0.154 \log(\mathrm{DM}) + 1.07 (\log \mathrm{DM})^2 - 3.86 \log f, \tag{1.21}$$

where τ_s is in ms when DM is in pc cm^{-3} and f in GHz. Although Equation 1.21 implies a clean functional form for τ_s, the fitted data show considerable scatter in τ_s for any given DM.

For long-period pulsars ($P > 0.1$ s), the magnitudes of $t_{\rm DM}$ and τ_s have little effect on $S_{\rm min}$, but for MSPs, dispersive smearing and scatter-broadening can make W a significant fraction of

Figure 1.7: P_{lim} (Equation 1.22) plotted as a function of DM for example surveys from Table 1.1. A duty cycle, $\delta = 0.1$, which is typical for MSPs, is used to compute P_{lim}. The dashed lines highlight spin periods of known MSPs, $1.5 < P < 30$ ms. For a given DM, colored curves show sources that can not be detected with $P < P_{\mathrm{lim}}$ for corresponding surveys. For the PMPS, dotted and dash-dotted lines show the magnitudes of t_{DM} and τ_s respectively.

the pulse period, resulting in a sharp rise in S_{min} for short spin periods. This effect can be seen clearly in Figure 1.4; compared to other surveys listed in Table 1.1, the PMPS has relatively large channel bandwidths and S_{min} suffers at short spin periods because of dispersive smearing. The GBNCC survey's broad sensitivity curve shows how DM has a greater relative effect on sensitivity for surveys at lower observing frequencies.

Looking back at Equation 1.16, note that a source with $W \geq P$ will be completely smeared out and therefore undetectable. There are DMs at which pulsars with spin periods shorter than some "limiting" spin period $P_{\mathrm{lim}} = W$ can not be detected due to the effects of t_{DM} and τ_s. Setting

Equation 1.20 equal to P_{lim}, substituting $W_{\mathrm{int}} = \delta P_{\mathrm{lim}}$ and solving for P_{lim} gives the expression,

$$P_{\mathrm{lim}} = \sqrt{\frac{t_{\mathrm{DM}}^2 + \tau_s^2}{(1-\delta)^2}} \tag{1.22}$$

where δ represents a source's intrinsic duty cycle. Plotting P_{lim} (see Figure 1.4), we can see exactly how t_{DM} and τ_{s} affect MSP detection in six example surveys. Due to its large channel bandwidths, the PMPS starts losing the ability to detect rapid MSPs at DM~ 150 pc cm^{-3} because of dispersive smearing. In all other cases, scatter-broadening plays a more significant role and precludes rapid MSP detection for low-frequency surveys at DM~ 100 pc cm^{-3}. Since τ_{s} is heavily dependent on f, P_{lim} ‴ 1.5 ms for PALFA and HTRU-North (both ~ 1.4 GHz surveys) around DM~ 300 pc cm^{-3}. These surveys probe significantly deeper into the Galactic plane than low-frequency counterparts. In fact, the PALFA survey has discovered a 2 ms MSP with DM = 297.5 pc cm^{-3} (Freire et al., 2011), a source just above P_{lim} and the MSP with the highest DM known to date.

Based on the lower sky temperatures at 1.4 GHz and less severe smearing due to dispersion and scatter-broadening, high frequency surveys are more well-suited for finding pulsars in the Galactic plane. Low frequency surveys have their own advantages as well. With larger beams, surveys like AO Drift and GBNCC can fully cover a region of sky much more quickly than high frequency surveys like PALFA. At $|b| > 30^{\circ}$, DM$_{\mathrm{max}}$ � 50 pc cm^{-3} and sky temperatures are more reasonable, such that low-frequency surveys can take full advantage of their sensitivities. Also, because pulsars are steep-spectrum objects, they usually have significantly higher flux densities at low frequency. Bates et al. (2013) found that normal pulsars have spectral indices of $\alpha = -1.4$, meaning that $S_{350}/S_{1400} = (f_{350}/f_{1400})^{\alpha} \sim 7$, which makes GBNCC's effective S_{min} comparable to HTRU-North's. MSPs are thought to have even steeper spectral indices, $\alpha = -1.9$ (Toscano et al., 1998).

Pulsar surveys with different observing parameters come with unique sets of advantages and disadvantages and therefore complement one another in discovering new and interesting systems.

1.5 Outline

In Chapter 2, I describe the Pulsar Arecibo L-band Feed Array (PALFA) precursor survey – specifically, its sky coverage, observing parameters, data processing pipeline, detections/discoveries and sensitivity. I re-evaluate expected yield for the full survey using population synthesis techniques and estimate the sizes of normal and millisecond pulsar populations such that they are consistent with the number of precursor detections.

Chapter 3 describes the Pulsar Search Collaboratory (PSC), which is a joint outreach program between NRAO and WVU that involves high school students in searching 350 MHz GBT drift scan data for new pulsars. I briefly describe survey parameters and the analysis process, but focus on results from students' seven pulsar discoveries, including a bright, nearby MSP that may prove a suitable addition to PTAs in the search for gravitational waves. We find that the students' discovery rate (per square degree of sky) is comparable to that of astronomers, who analyzed a larger fraction of the 350 MHz GBT drift scan survey data.

Two years ago, PSC students discovered PSR J1930$-$1852, a double neutron star (DNS) binary system with the widest orbit known among DNSs. I devote the entirety of Chapter 4 to this system, describing our timing follow-up procedure, optical follow-up and a detailed timing solution, including a measurement of the system's advance of periastron predicted by General Relativity. This measurement places constraints on the total mass of the system; I outline typical DNS formation scenarios and describe the ways in which J1930$-$1852 challenges current DNS evolutionary theory.

Making use of larger bandwidths (and soon new telescopes!), pulsar surveys continue to probe deeper into the underlying pulsar population, offering glimpses at new, exotic systems that test our understanding of binary evolution, the pulsar life cycle and emission mechanism. A larger sample size of MSPs in particular will provide a clearer picture of the Galactic distribution of MSPs and their luminosity function. Additional MSP discoveries can improve the sensitivity of PTAs, but a more accurate description of the underlying population will allow us to characterize the potential sensitivity of our “gravitational wave detector."

Since pulsar survey data analysis and follow-up timing of discoveries can be approachable tasks for beginning scientists, pulsar surveys are not only vital to PTAs because of the MSPs they provide, but also because of their potential for involving the next generation of scientists in real, hands-on research. In order to sustain long-term projects like NANOGrav, it is essential that the PSC and Arecibo Remote Command Center (ARCC)[16] become increasingly involved in current pulsar surveys and related projects since they will supply our next generation of pulsar and gravitational wave astronomers.

---

[16] ARCC involves undergraduates from the University of Texas – Rio Grande Valley, Franklin & Marshall College, University of Wisconsin – Milwaukee and other institutions in pulsar survey candidate selection, follow-up timing and observing.

Chapter 2

Arecibo Pulsar Survey Using ALFA. III.

Precursor Survey and Population Synthesis

Swiggum et al. 2014, ApJ, 787, 137

2.1 Introduction

Our current knowledge of the non-recycled (hereafter *normal*) pulsar and millisecond pulsar (MSP) Galactic populations[1] — their spatial, period and luminosity distributions — primarily comes from the results of the Parkes Multibeam Pulsar Survey (PMPS; Manchester et al., 2001; Morris et al., 2002; Kramer et al., 2003; Hobbs et al., 2004; Faulkner et al., 2004; Lorimer et al., 2006b). Analyses of these results have shown that the Galactic normal pulsar population is made up of 30,000±1,100 sources beaming toward Earth with luminosities above 0.1 mJy kpc^2; their radial density profile is best described by a gamma function and their distance from the Galactic plane, by an exponential function with a scale height of 0.33 kpc (Lorimer et al., 2006b). A more physically realistic treatment of pulsar luminosities involves using a log-normal luminosity function, which is demonstrated from pulsar population syntheses (e.g., Faucher-Giguère & Kaspi, 2006). The advantage of this approach is that it allows predictions of the *total* normal pulsar population size — not just the number above a certain luminosity cutoff; Faucher-Giguère & Kaspi (2006) predict that there are 120,000±20,000 detectable, normal pulsars in the Galaxy.

---

[1] Although a number of traits separate normal from millisecond pulsars, the most distinct is an MSP's short spin period, which is the result of angular momentum transferred by material from a binary companion. For the remainder of this paper, we use P = 30 ms and $B_{\rm surf} = 10^{10}$ G as period and surface magnetic field thresholds to differentiate between MSPs (P < 30 ms, $B_{\rm surf} < 10^{10}$ G) and normal pulsars (P > 30 ms, $B_{\rm surf} > 10^{10}$ G), although there are certainly exceptions to this simple separation. A complete list of currently known Galactic MSPs can be found at http://astro.phys.wvu.edu/GalacticMSPs

Since there are only ~ 10% as many known MSPs as normal pulsars (Manchester et al., 2005), we do not have the same level of knowledge about recycled pulsars' population parameters. The High Time Resolution Universe (HTRU) Survey (Keith et al., 2010) has added more normal pulsar discoveries to the PMPS haul and many MSPs as well (e.g., Bates et al., 2011; Burgay et al., 2013; Morris et al., 2002; Hobbs et al., 2004; Mickaliger et al., 2012). Recent analysis of the intermediate latitude portion of HTRU MSP detections by Levin et al. (2013) uses a scale factor method (Vivekanand & Narayan, 1981; Lorimer et al., 1993) and 50 detected MSPs to place a lower limit of 30,000±7,000 on the Galactic MSP population size (considering sources whose luminosities exceed 0.2 mJy kpc^2). The scale height of the MSP population is fairly well established to be 500 pc (Lorimer, 2005; Cordes & Chernoff, 1997), but the spatial, period and luminosity functions are currently less well understood. Although many models can be ruled out, plausible MSP populations with a variety of underlying distributions are consistent with the observed sample (Lorimer, 2010).

Despite the fact that Arecibo's latitude does not permit observations close to Galactic center like those at Parkes, the unique combination of Arecibo's sensitivity, paired with the high spectral resolution of its back-ends, provides a much deeper view through the Galaxy's dispersive medium, which often smears out signals from distant sources. Although the PMPS and HTRU surveys have sampled much of the sky surrounding the Galactic center — an area of the sky with high pulsar density — and have discovered over 1,000 pulsars, PALFA provides a glimpse of the population density at larger Galactic radii ($R > 5$ kpc), which will help improve the spatial features of future pulsar population models. Arecibo's ability to reach competitive sensitivity limits with short integration times (1–5 minutes) makes acceleration searches for binaries unnecessary for all but the most exotic systems. Finally, Arecibo's unrivaled sensitivity allows PALFA to probe the low-luminosity end of the Galactic pulsar population, leading to a better understanding of the underlying luminosity distribution.

With Arecibo's unique capabilities, PALFA has great potential to discover many normal pulsars as well as MSPs, thus improving our statistical picture of each population's characteristics.

Given the number of discoveries by PMPS, it has historically been used to refine pulsar population modeling assumptions for normal pulsars. Recent efforts have been made to discover additional MSPs in archival PMPS data (Mickaliger et al., 2012) with motivation to improve MSP population models. With higher sensitivity to dispersed sources and MSPs, the PALFA survey's influence on normal and millisecond pulsar population studies will complement those of the PMPS and HTRU surveys. MSPs are essential for the direct detection of gravitational waves by pulsar timing array projects (e.g., Demorest et al., 2013). The best way to increase our sensitivity to the stochastic background is to add new MSPs to the array (Siemens et al., 2013).

In this chapter, we present the detections and discoveries from the initial phase of the PALFA survey, hereafter referred to as the "precursor survey". In §2.9, we describe the PALFA precursor survey parameters and sky coverage and introduce two pipelines used to process the raw data. We present the 45 detections made by the precursor survey in §2.10 and include an evaluation of the survey's efficacy based on measured and theoretically calculated signal-to-noise (S/N) ratios. In §2.11 we discuss the portion of sky in the precursor survey that overlapped with the PMPS and show preliminary evidence that PALFA will indeed be probing more distant, fainter sources. Comparing population simulations to precursor survey detection statistics, we generate probability density functions (PDFs) for normal and millisecond pulsar populations in §2.12. These PDFs inform the predictions we make about the total number of pulsars (normal and MSP) we expect to have detected when the full PALFA survey is complete. We conclude in §2.13, stating the most probable normal and millisecond pulsar population sizes according to the precursor survey results.

2.2 Sky Coverage and Data Analysis

The PALFA precursor survey covered portions of two Galactic sectors — an inner Galaxy region, 36° � £ � 75°, tiled with 865 pointings, and an outer Galaxy region, 170° � £ � 210°, covered by 919 pointings. All pointings were within one degree of the Galactic plane ($|b| < 1^\circ$) and had dwell times of 134 and 67 seconds for inner- and outer-Galaxy regions respectively. The precursor survey used the Arecibo L-band Feed Array (ALFA) 7-beam receiver in conjunction with the Wideband Arecibo Pulsar Processor (WAPP) back-end (Dowd et al., 2000), which was set up to record 256 channels covering a 100 MHz bandwidth, centered at 1.42 GHz, every 64 μs. Each ALFA pointing includes seven distinct beam positions in a hexagonal pattern. As PALFA continues, the sky coverage will increase slightly in Galactic longitude (32° � *£* � 77° and 168° � *£* � 214°) and will extend to Galactic latitude $\pm 5^{\circ}$. For the remainder of the paper, we will refer to this extended spatial coverage (accompanied by a three-fold increase in bandwidth) as the *full PALFA survey*. The precursor survey, optimized for maximum efficiency and sensitivity, used a "sparse sampling" technique described in detail in Cordes et al. (2006); gaps left by the precursor survey will be covered in multiple passes by the full PALFA survey. PMPS overlaps with the southernmost regions covered by Arecibo in the PALFA precursor survey, corresponding to 36° � *£* � 50°. In §2.10, we will compare the performance of the two surveys in this overlap region to make a statement about the efficacy of the PALFA precursor survey.

Data from the PALFA precursor were previously analyzed in Cordes et al. (2006). That analysis used a quasi-real-time QUICKLOOK pulsar search pipeline in which the data were decimated in time and frequency by factors of 8 and 16, respectively, yielding 32 spectral channels and 1024 μs time resolution. Using the decimated data, 11 pulsars were discovered and 29 previously known pulsars were detected. Timing and spectral characteristics from follow-up observations of the newly discovered pulsars are given in Nice et al. (2013).

We have analyzed these same data files at native full time- and frequency-resolution using the PALFA survey's PRESTO 1 pipeline. The full resolution search of the precursor survey data did not yield any pulsar discoveries (and in fact missed some sources flagged by the QUICKLOOK pipeline), but revealed two more previously known normal pulsars (J1946+2611, B1924+16) and the bright MSP B1937+21. The PRESTO 1 zaplist, a list of frequencies and their harmonics related to known sources of RFI, may be responsible for this scant improvement over QUICKLOOK results since it was fairly restrictive, "zapping" $\sim 8\%$ of the spectral region between $0-10$ Hz ($\sim 84\%$ of known pulsars have spin frequencies in this range). At least one previously known source, B1925+188, fell inside a zapped portion of the spectrum, but its fourth harmonic was still detectable in PRESTO 1 results. Four other sources that were detected by QUICKLOOK (J1913+1000, B1919+14, J2002+30 and J2009+3326) were not detectable in PRESTO 1 results. Of the 12,488 PALFA precursor beams, 183 (1.5%) were not processed by the PRESTO 1 pipeline, including beams where J1913+1000 and B1919+14 should have been detected. PSRs J2002+30 and J2009+3326 were processed by PRESTO 1 and their spin frequencies were outside zapped portions of the spectrum; why these two sources were not detectable remains unknown, although it is plausible that harmonics of their true spin frequencies could have been "zapped," causing these sources to fall below a detectable threshold.

After the precursor survey was complete, raw data products were decimated to 4-bit resolution and saved in that form. In the process, some files were lost or corrupted (i.e. detection data files for J1913+1000, B1919+14 and B1924+16), so results from Cordes et al. (2006) were used when necessary. We used a complete list of precursor beam positions to determine minimum offset angles from each known source in the survey region, then refolded corresponding 4-bit data files, yielding two additional detections (J1906+0649 and J1924+1631). Table 2.3 outlines the means by which all sources in the PALFA precursor survey were detected.

2.2.1 PRESTO 1 Pipeline

The PALFA PRESTO 1 pipeline[2] used to analyze precursor survey data first converted WAPP-format data to SIGPROC filterbank-format (Lorimer, 2001). Each filterbank file, one per beam, was then processed independently using various programs from the PRESTO suite of pulsar analysis software[3] (Ransom et al., 2002). Strong narrow-band impulsive and periodic signals were identified as interference by `rfifind`. The filterbank files were then cleaned and reduced-frequency-resolution sub-band files were created at various dispersion measures (DMs). Each group of sub-

---

[2] Many of the aspects of the PALFA precursor survey data processing described here have since been augmented (e.g., Lazarus (2013)), including a new complementary pipeline based on the Einstein@Home distributed volunteer computing platform, e.g. Allen et al. (2013).

[3] https://github.com/scottransom/presto

band files was then used to create time series with DMs close to the DM of the sub-band file. In total 1056 trial DM values were used between $0 \leq \mathrm{DM} \leq 1003.2\,\mathrm{pc\ cm^{-3}}$. The upper limit was chosen to reflect the maximum expected DM in the sky region surveyed (Cordes & Lazio, 2002).

Each dedispersed time series was searched for single pulses using single_pulse_search.py. Significant pulses ($\sigma > 6$) with widths up to 0.1 s were identified and a diagnostic plot was generated for human inspection. The time series were also Fourier transformed and searched for periodic signals using accelsearch. The periodicity search was done in two parts, one for unaccelerated pulsars using up to 16 summed harmonics and the other for accelerated pulsars using up to 8 summed harmonics. The high-acceleration search used a Fourier-domain algorithm (Ransom et al., 2002) with a maximum drift of 50 FFT bins. Non-pulsar-like signals were removed from the candidate lists generated from the low and high-acceleration searches. The manicured low and high-acceleration candidate lists were then combined. Candidates harmonically related to a stronger candidate were discarded, while the top 50 candidates with $\sigma > 6$ were "folded" modulo the best Fourier-detected period using prepfold, which effectively provides a fully-coherent harmonic sum of the signal power. The resulting plots, along with basic metadata about the observations were loaded into a database hosted at Cornell University, where volunteers selected and inspected candidate plots.

2.2.2 Detection S/N Measurements

For all sources detected by the Quicklook and Presto 1 processing pipelines, we refolded data files from beam positions nearest those sources using known pulsar parameters and calculated measured signal-to-noise $(\mathrm{S/N})_{\mathrm{meas}}$ values. For each pulse profile, we used a simple algorithm to determine on- and off-pulse bins, then summed on-pulse intensities and divided by the maximum profile intensity to get an equivalent top-hat pulse width W_{eq} (in bins). Finally, $(\mathrm{S/N})_{\mathrm{meas}}$ is computed with

$$(\mathrm{S/N})_{\mathrm{meas}} = \frac{1}{\sigma_p \sqrt{W_{\mathrm{eq}}}} \sum_{i=1}^{n_{\mathrm{bins}}} (p_i - \bar{p}), \tag{2.1}$$

as in Lorimer & Kramer (2004), where $\bar{p}$ and σ_p are the mean and standard deviation of off-pulse intensities respectively, p_i is the intensity of an individual profile bin and each profile had $n_{\rm bins} = 128$. We divided $W_{\rm eq}$ by the number of bins in a profile $n_{\rm bins}$ to convert to duty cycle δ for each detection. Computed δ and $({\rm S/N})_{\rm meas}$ values are listed in Table 2.3.

2.3 Survey Results

To measure the effectiveness of a pulsar survey, we look at the known sources that fall inside the survey region and compare the number of detections to the number of expected detections. Effectiveness will then be evaluated by whether the survey meets/exceeds expectations for detecting individual sources.

2.3.1 Defining Detectability

The PALFA multibeam receiver is composed of seven beams, each with an average full width half maximum (FWHM) of $\sim 3.35^{1}$; adjacent beams are separated by $\sim 5.5^{1}$, or ~ 1.6 half-power beam widths. Outer beams and the central beam have gains of 8.2 and 10.4 K Jy^{-1} respectively (Cordes et al., 2006). Although previous population studies have modeled gain patterns using Gaussian functions (e.g., Lorimer et al., 2006b), we use an Airy disk function to better model the additional gain from the side lobes of individual beams. Although this is not a perfect representation of the PALFA survey's true gain pattern — in fact, the side lobes of the outer ALFA beams are highly asymmetric (see Spitler et al. (2014) for a more precise model) — the Airy disk captures Arecibo's off-axis gain better than the Gaussian model and still provides the simplicity required to run population simulations quickly.

The theoretical signal-to-noise ratio $({\rm S/N})_{\rm th}$ for a given pulsar with flux density (S_{1400}) mea-

PSR Name	P (s)	DM (pc cm^{-3})	(°)	b (°)	$\Delta\theta$ ($'$)	Duty Cycle (%)	Flux Density (mJy)	(S/N)$_{\rm th}$	(S/N)$_{\rm meas}$	Pipeline Detected? (QL / P1 / Refold)	PALFA Discovery?
J0540+3207	0.524	61	176.7	0.8	1.43	2.1	0.34	62.6	32.8	QL, P1, Refold	Yes
J0628+0909	1.241	88	202.2	–0.9	2.30	1.4	0.06	4.6	21.0	QL, P1, Refold	Yes
J0631+1036	0.288	125	201.2	0.5	1.51	3.3	0.80	85.1	104.1	QL, P1, Refold	
J1855+0307	0.845	402	36.2	0.5	3.24	1.7	0.97	12.4	48.4	QL, P1, Refold	
J1901+0621	0.832	94	39.7	0.8	1.76	5.6	0.47	35.2	21.3	QL, P1, Refold	Yes
B1859+07	0.644	252	40.6	1.1	2.29	3.0	0.90	55.1	38.8	QL, P1, Refold	
J1904+0738	0.209	278	41.2	0.7	0.90	1.9	0.23	54.2	20.1	QL, P1, Refold	Yes
J1904+0800	0.263	438	41.5	0.9	1.99	2.8	0.36	41.0	21.2	QL, P1, Refold	
J1905+0616	0.990	256	40.1	–0.2	1.80	1.5	0.51	69.7	47.4	QL, P1, Refold	
B1903+07	0.648	245	40.9	0.1	0.52	5.6	1.80	266.2	171.3	QL, P1, Refold	
J1905+0902	0.218	433	42.6	1.1	0.50	1.9	0.10	21.1	22.2	QL, P1, Refold	Yes
B1904+06	0.267	472	40.6	–0.3	2.43	5.6	1.70	61.8	104.1	QL, P1, Refold	
J1906+0649	1.287	249	40.7	–0.2	2.53	6.3	0.30	9.2	20.2	Refold	
J1906+0746	0.144	217	41.6	0.1	2.60	1.6	0.55	28.8	15.0	QL, P1, Refold	Yes
J1906+0912	0.775	265	42.8	0.9	2.37	2.5	0.32	19.4	14.4	QL, P1, Refold	
J1907+0740	0.575	332	41.6	–0.1	2.24	2.2	0.41	30.5	25.3	QL, P1, Refold	
J1907+0918	0.226	357	43.0	0.7	3.00	1.6	0.29	7.5	21.8	QL, P1, Refold	
J1908+0734	0.212	11	41.6	–0.3	1.05	3.1	0.54	90.1	23.1	QL, P1, Refold	
J1908+0909	0.337	467	43.0	0.5	1.70	2.2	0.22	28.5	60.9	QL, P1, Refold	
B1907+10	0.284	149	44.8	1.0	1.92	2.3	1.90	206.9	83.8	QL, P1, Refold	
J1910+0714	2.712	124	41.5	–0.9	1.72	1.4	0.36	59.8	15.8	QL, P1, Refold	
B1910+10	0.409	147	44.8	0.2	2.32	3.7	0.22	11.0	—	—	
J1913+1000	0.837	422	44.3	–0.2	1.69	3.8	0.53	66.5	26.0	QL	
J1913+1011	0.036	178	44.5	–0.2	2.69	4.1	0.50	14.1	19.9	QL, P1, Refold	
J1913+1145	0.306	637	45.9	0.5	2.06	4.7	0.43	23.4	—	—	
B1911+11	0.601	100	45.6	0.2	1.90	4.2	0.55	43.9	—	—	
B1913+10	0.405	241	44.7	–0.7	1.51	1.6	1.30	238.2	34.6	QL, P1, Refold	
B1914+13	0.282	237	47.6	0.5	1.78	2.4	1.20	152.8	230.4	QL, P1, Refold	
B1915+13	0.195	94	48.3	0.6	2.29	2.5	1.90	131.6	239.9	QL, P1, Refold	
B1916+14	1.181	27	49.1	0.9	3.04	1.4	1.00	26.9	21.7	QL, P1, Refold	
B1919+14	0.618	91	49.1	0.0	0.45	3.6	0.68	140.2	41.0	QL	
B1921+17	0.547	143	51.7	1.0	3.01	3.6	—	—	46.8	QL, P1, Refold	
J1924+1631	2.935	518	51.4	0.3	0.65	1.0	0.09	35.4	10.5	Refold	
B1924+16	0.580	176	51.9	0.1	0.83	2.5	1.30	363.5	90.9	P1	
B1925+188	0.298	99	53.8	0.9	1.92	5.9	—	—	27.8	QL, P1, Refold	
J1928+1746	0.069	176	52.9	0.1	0.70	5.2	0.28	46.9	29.6	QL, P1, Refold	Yes
B1929+20	0.268	211	55.6	0.6	3.78	2.0	1.20	1.7	24.0	QL, P1, Refold	
B1937+21	0.00156	71	57.5	–0.3	2.41	14.9	13.20	327.0	180.5	P1, Refold	
J1946+2611	0.435	165	62.3	0.6	2.61	2.4	—	—	18.5	P1, Refold	
B1952+29	0.427	7	66	0.8	2.53	4.5	8.00	325.8	117.3	QL, P1, Refold	
J1957+2831	0.308	138	65.5	–0.2	1.57	3.6	1.00	131.2	30.0	QL, P1, Refold	
J2002+30	0.422	196.0	67.9	–0.2	1.21	3.7	—	—	60.7	QL, Refold	
B2000+32	0.697	142	69.3	0.9	2.16	1.8	1.20	121.7	49.1	QL, P1, Refold	
B2002+31	2.111	234	69.0	0.0	3.30	1.3	1.80	26.3	94.4	QL, P1, Refold	
J2009+3326	1.438	263	71.1	0.1	0.82	3.0	0.15	32.4	23.9	QL, Refold	Yes
J2010+3230	1.442	371	70.4	–0.5	0.60	2.2	0.12	32.6	23.4	QL, P1, Refold	Yes
J2011+3331	0.932	298	71.3	–0.0	2.50	2.6	0.38	21.2	39.4	QL, P1, Refold	Yes
J2018+3431	0.388	222	73.0	–0.8	1.70	2.0	0.24	47.4	31.7	QL, P1, Refold	Yes

Table 2.1: A comprehensive list of all pulsars detected by the precursor survey as well as those we expected to detect, given their high (S/N)$_{\rm th}$ quantities. We list each pulsar's period (P), dispersion measure (DM), Galactic longitude (£), Galactic latitude (b), angular offset from the closest beam ($\Delta\theta$) and duty cycle (δ), as well as (S/N)$_{\rm th}$, (S/N)$_{\rm meas}$. PALFA precursor data were run through two processing pipelines, Quicklook and Presto 1 (described in §2.9), then converted into 4-bit files and stored. Pulsars detected by Quicklook (QL) or Presto 1 (P1) pipelines are marked accordingly; those detected after refolding archived, 4-bit data files have "Refold" in the "Pipeline Detected?" column. Previously unknown pulsars discovered by the precursor survey are marked with a "Yes" in the last column. For sources without an available flux density measurement, we did not compute (S/N)$_{\rm th}$. Previously determined parameters (P, DM, £, b and flux density) were obtained from the ATNF Pulsar Catalog (Manchester et al., 2005). Missing parameters, (S/N)$_{\rm th}$ and (S/N)$_{\rm meas}$ for example, are denoted by dashes (—).

sured in mJy at 1400 MHz, spin period P, and pulse width W is given by

$$(\mathrm{S/N})_{\mathrm{th}} = \frac{S_{1400}\, G \sqrt{n_p\, t_{\mathrm{obs}}\, \Delta f}}{\beta\, T_{\mathrm{sys}}} \sqrt{\frac{1-\delta}{\delta}}, \tag{2.2}$$

where $\delta = W/P$ is the pulse duty cycle; G is the gain in K Jy^{-1} of a specific beam, $n_p = 2$ is the number of summed polarizations, t_{obs} is the integration time (134 s and 67 s for inner- and outer-Galaxy observations, respectively), Δf = 100 MHz is the bandwidth, β = 1.16 is a correction factor that accounts for losses in the digitization process and T_{sys} is the system temperature measured in K (Dewey et al., 1985). Flux densities S_{1400} were obtained from the ATNF Pulsar Catalog (Manchester et al., 2005) for known pulsars and Nice et al. (2013) for pulsars discovered by the PALFA precursor survey. Equation 2.6 is an approximation since this treatment assumes top-hat pulse profiles and ignores the considerable variability in pulse shape. The majority of pulsars have Gaussian-shaped profiles however, so this approximation works well in most cases.

Hereafter $(\mathrm{S/N})_{\mathrm{th}}$ will refer to theoretical signal-to-noise ratios, computed using Equation 2.6, while $(\mathrm{S/N})_{\mathrm{meas}}$ refers to signal-to-noise ratios measured from PALFA detections as described in §2.9.2 and specifically, Equation 2.5.

Since gain is a function of a source's angular offset from the beam center, we model it as an Airy disk so that the gain

$$G = G_0 \left[\frac{2\, J_1(k\, a\, \sin(\theta))}{k\, a\, \sin(\theta)}\right]^2, \tag{2.3}$$

where J_1 is a Bessel function of the first kind, G_0 is the maximum on-axis gain of the beam, $k = 2\pi/\lambda$ is the wavenumber (λ, the observation wavelength), a is the effective aperture radius ($\sim$ 220 m), and θ is the angular offset of a source from the beam center, measured in radians. In predicting S/N for a given pulsar, the pulsed nature of its emission must be taken into account, as shown by the final term in Equation 2.6. For all pulsars that were detected in the precursor survey, we computed W_{eq}, then δ as described in §2.9.2. For sources that were not detected, we divide the pulse width at half maximum (W50), from the ATNF Pulsar Catalog (Manchester et al., 2005), by the period to compute δ, then $(\mathrm{S/N})_{\mathrm{th}}$. Finally, T_{sys} includes the receiver temperature

Figure 2.1: The left plot shows theoretical versus measured S/Ns for each source with both quantities available. If the two values match for a given source, the data point for that source should lie along the solid line with slope unity. The loose correlation shown here is a result of a combination of effects, but most notably, there can be as much as $\sim 30\%$ fractional error in $(\mathrm{S/N})_{\mathrm{th}}$ due to uncertainties in initial flux measurements, which were taken from the ATNF Pulsar Catalog (Manchester et al., 2005); interstellar scintillation and RFI also contribute to the large scatter. Dashed lines give a reference for sources whose theoretical and measured S/N values are different by a factor of 10. The right plot emphasizes the fact that, in addition to the significant dispersion, $(\mathrm{S/N})_{\mathrm{meas}}$ is smaller than $(\mathrm{S/N})_{\mathrm{th}}$ in many cases. This systematic offset implies a poor understanding of the noise environment and suggests that the maximum sensitivity limits of the survey have not yet been realized.

($T_{\mathrm{rec}} = 24\,\mathrm{K}$) and sky temperature ($T_{\mathrm{sky}}$), which varies as a function of position and frequency as shown by Haslam et al. (1982). Since this sky temperature map describes T_{sky} at 408 MHz, we convert these values into 1.4 GHz sky temperatures using an assumed spectral index of $\alpha = 2.6$, that is $T_{\mathrm{sky}} \propto \nu^{-\alpha}$.

Although there are many factors involved, we assume a 1:1 relationship between $(\mathrm{S/N})_{\mathrm{meas}}$ and $(\mathrm{S/N})_{\mathrm{th}}$ in order to use S/N as a prediction tool for the detectability of known sources. The true relationship between $(\mathrm{S/N})_{\mathrm{meas}}$ and $(\mathrm{S/N})_{\mathrm{th}}$ can be seen in Figure 2.6.

Using a complete list of beam positions, we found the survey observations carried out closest to known pulsars in the precursor region (i.e. minimizing angular offset, θ). For each of these positions, we found the maximum expected gain for a given pulsar using Equation 2.7. Previously measured parameters for known pulsars allowed us to compute a theoretical signal-to-noise,

Figure 2.2: Beam positions for the PMPS (light gray) and PALFA precursor survey (dark gray) are shown here with known pulsar positions superimposed. The Parkes beam radii are about 4 times as large as those of Arecibo; the points indicating beam positions have been scaled appropriately relative to one another. Only PMPS beams within 1.2° of the Galactic plane are plotted since this more than covers the Galactic latitude limits of the PALFA precursor survey. Of the 58 previously known pulsars plotted here, many were too far from the nearest precursor survey beam center, making them undetectable. Only 24 of 59 were deemed detectable, given the precursor survey's patchy coverage of this Galactic sector, and were considered in comparing the two surveys. Known pulsars detected by the precursor survey are marked with crosses, while expected detections that were missed are marked with open circles. Filled circles indicate the positions of PALFA precursor survey discoveries in the region overlapping with PMPS.

$(S/N)_{\rm th}$, as shown in Equation 2.6. We define a known pulsar to be detectable if we find $(S/N)_{\rm th} > 9$ for that pulsar. A full list of pulsars detected by the precursor survey as well as those considered detectable due to their $(S/N)_{\rm th}$ values can be found in Table 2.3. Before PALFA began, there were 84 known pulsars positioned inside the target precursor survey region, although this sky area was not covered uniformly; 31 of 84 were deemed detectable, while 33 were actually detected, and seven had no previous flux measurements. Of the 51 non-detections, most can be attributed simply to the sources not being close to a PALFA precursor survey beam pointing, as the survey had only limited coverage in this region. Figure 2.7 shows the portion of the precursor survey that overlaps with the PMPS), an example of this limited coverage. Three of the 51 non-detections (B1910+10, J1913+1145, and B1911+11) were unexpected, since $(S/N)_{\rm th} > 9$ for these sources; one of the 33 detections (B1929+20) was also unexpected, given its low $(S/N)_{\rm th}$ value. The non-detections could be due to a variety of factors — most likely RFI. Scintillation could have also suppressed the expected signal during precursor survey observations or boosted the signal during initial flux measurements. It is unlikely scintillation affected the detectability of J1913+1145, however, because of this source's high DM (637 pc cm^{-3}). Given the short integration time near each of these sources (134 s), the pulse-to-pulse variability may have strongly affected $(S/N)_{\rm meas}$ since relatively few pulses were recorded. Also, because of the large error bars on $(S/N)_{\rm th}$ ($\sim 30\%$ fractional error) due to uncertainties in flux measurements, the sources may simply be weaker than expected.

Although most sources with high $(S/N)_{\rm th}$ values were detected by the precursor survey's processing pipelines, five such sources were not. For each of these cases, we employed the same procedure as introduced in Section 2.9.2, using known periods and dispersion measures to dedisperse and fold the data from the closest pointing to each source. For the three sources mentioned earlier (B1910+10, B1911+11, and J1913+1145), no pulsations were detected; for the other two, J1906+0649 and J1924+1631, pulsations are evident, but relatively weak. PSR J1906+0649 was likely missed because of the RFI environment at Arecibo.

In addition to the 33 re-detected pulsars in the region, PSR J1924+1631 was discovered shortly after the precursor survey was completed, when the PALFA survey underwent an upgrade to a new

Prior Distribution Parameter	Normal PSR Simulations	MSP Simulations
Luminosity	Log Normal: $\mu = -1.1; \sigma = 0.9$	Log Normal: $\mu = -1.1; \sigma = 0.9$
Period	Log Normal: $\mu = 2.7, \sigma = 0.34$	(see Figure 2.9)
Radial	Gamma Function: (see Lorimer et al., 2006b)	Gaussian: $\sigma = 6.5$ kpc
Scale height	0.33 kpc	0.5 kpc
Duty Cycle	(explained in §2.12.1)	(explained in §2.12.1)
Electron Model	NE2001	NE2001

Table 2.2: Assumed parameter values/distributions for normal and millisecond pulsar populations respectively. These parameters are used as input values to the appropriate PsrPopPy functions, which generate an underlying, synthetic population. Changing input parameters directly affects the number of detections expected from a given simulated survey.

backend with three times more bandwidth. This source was then retroactively found in precursor survey data with $(S/N)_{\mathrm{meas}}$ just above the detection threshold and has therefore been included in analysis that follows. Strong RFI present in the refolded precursor data explains why this source was not discovered earlier. Lazarus et al. (2015) describe the most recent processing pipeline in detail, address the RFI environment and its effect on the PALFA survey's "true" sensitivity.

2.4 PMPS Overlap Region

The PALFA precursor survey region overlaps the region covered by the PMPS in Galactic longitude, 36° � £ � 50°. Although there were 58 previously known pulsars in this longitude range and within $\sim 1^\circ$ of the Galactic plane when the precursor survey took place (see Figure 2.7), we compare the PMPS and precursor survey detections only based on sources deemed detectable by the precursor survey. We justify this criterion based on the fact that, due to patchy coverage, only ~10% of the overlap region lies within an angular offset $\Delta\theta \sim 1.2^{1}$ of a precursor beam center. We choose 1.2^{1} since this is the average angular offset $(\Delta\theta) = \mathrm{FWHM}/2\sqrt{2}$ for the precursor survey. Half of all sources that fall within a radius $R = \mathrm{FWHM}/2$ of the nearest beam center will also be within the average angular offset $(\Delta\theta)$.

The PMPS discovered or detected all 24 of the previously known pulsars in this region considered detectable by the PALFA precursor survey. The precursor survey detected 21 of these, and discovered an additional four sources in this region. The PMPS retroactively detected two of these four precursor discoveries in archival data (e.g., Lorimer et al., 2006b).

One of the three detectable known pulsars that the precursor survey missed, B1910+10, had a $(S/N)_{th}$ value of ~ 11 (see Table 2.3), just above the detectability threshold of $(S/N)_{th} = 9$; the other two, J1913+1145 and B1911+11, were expected to be detected with $(S/N)_{th} = 23$ and 36 respectively. Error in $(S/N)_{th}$ is $\sim 30\%$, which reflects the error in flux measurements and can easily explain the first non-detection. It is much harder to explain why J1913+1145 and B1911+11 were not detected, given their high $(S/N)_{th}$ values, but other systematics such as RFI and scintillation may explain these discrepancies.

The four precursor survey discoveries — J1901+0621, J1904+0738, J1905+0902 and J1906+0746 — have relatively high dispersion measures and were all detected near the signal-to-noise threshold with $15 < (S/N)_{meas} < 22$, so it is not surprising that they were not detected by previous surveys. PSR J1906+0746 is a 144 ms pulsar in a relativistic, 3.98 hr orbit and was initially missed during manual inspection of PMPS candidate plots due to RFI with a period similar to that of the pulsar (Lorimer et al., 2006a). Both J1906+0746 and J1901+0621 were found retroactively in Parkes data, which was expected, given that both are moderately bright sources with flux densities at 1400 MHz of about 0.5 mJy. The other two discoveries, J1904+0738 and J1905+0902, are much fainter — 0.23 and 0.097 mJy respectively (Nice et al., 2013). These discoveries show preliminary evidence that with Arecibo's high sensitivity, the PALFA precursor survey probed a deeper and lower-luminosity pulsar population than previous surveys. However, the three unexpected non-detections suggest that the PALFA precursor survey did not realize its full sensitivity and more work is required to better understand Arecibo's RFI environment and develop mitigation techniques.

The relative sensitivity limits as a function of period and DM for the PMPS and precursor surveys are compared in Figure 2.8. To generate these curves, we used an average T_{sky} value for

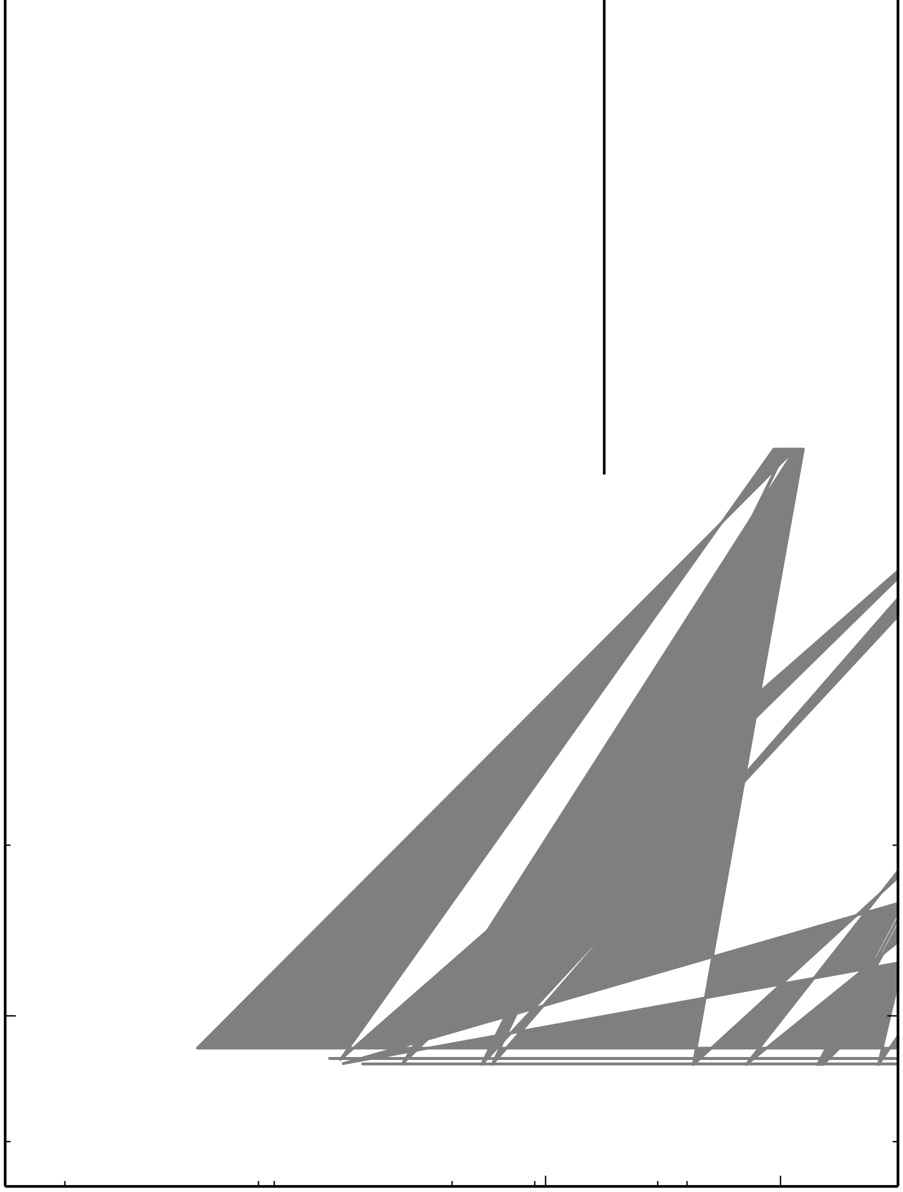

Figure 2.3: Sensitivity as a function of period for the precursor survey is shown in dark gray; the PMPS curve (light gray) is shown here for comparison. The dashed lines in each case show the sensitivity to DM = 100 pc cm^{-3} sources, while upper and lower limits of the shaded regions give minimum flux density sensitivity to pulsars with DM = 150 or 50 pc cm^{-3} respectively. These curves are plotted using the average angular offset $(\Delta\theta)$ between a source and a beam position. For a random distribution of pulsars on the sky, ~ 50% should fall within an angle $(\Delta\theta)$ from the nearest beam position. Precursor survey discoveries are superimposed; expected detections B1910+10, B1911+11 and J1913+1145 that were missed by the PALFA precursor survey, but detected by PMPS are shown with open circles.

each survey region, assumed a constant pulse duty cycle of $\delta = 0.05$, and applied the empirical pulse broadening function from Bhat et al. (2004) to account for multipath scattering in the interstellar medium. For the three objects that were detected at Parkes, but not in the PALFA precursor survey (B1910+10, J1913+1145 and B1911+11), all have periods between 300 and 600 ms, a regime where the PMPS nominal sensitivity limit in Figure 2.8 is about twice as high as the precursor survey's. However, the angular offsets to these sources (6.6^{1}, 4.7^{1} and 2.5^{1} respectively for PMPS and precursor values can be found in Table 2.3) imply that both surveys were equally sensitive to them since the PALFA precursor beam (FWHM$\sim 3.35^{1}$) is much narrower than that of the PMPS (FWHM$\sim 14.4^{1}$) and its sensitivity therefore drops off more quickly as a function of $\Delta\theta$. Taking angular offsets into account, B1910+10 ($S_{1400} = 0.22$ mJy) falls below the adjusted minimum sensitivity limit (~ 0.26 mJy for both surveys), but B1911+11 and J1913+1145 do not, so angular offsets alone do not explain why these sources went undetected. Since other sources with lower flux densities and similar angular offsets *were* detected (i.e. J0628+0909, J1906+0649, J1906+0912, J1907+0740, J1907+0918, J2011+3331), we conclude that transient effects such as RFI decreased the signal-to-noise ratios of B1910+10, B1911+11 and J1913+1145 and possibly scintillation for the former two.

2.5 Population Analysis

The analysis presented here uses PsrPopPy — a package that models the Galactic population and evolution of pulsars. With this software, we populated a synthetic galaxy with pulsars whose attributes like cylindrical spatial coordinates, period, DM, luminosity, etc. were chosen from predetermined PDFs (Lorimer et al., 2006b). PsrPopPy[4] is a Python implementation of PSRPOP[5], which was written in Fortran (Lorimer et al., 2006b); it shares much of the same functionality, but the object-oriented nature of Python and improved modularity of the code make it more readable and easier to write plug-ins for specific modeling purposes. Additional details describing the

---

[4] https://github.com/samb8s/PsrPopPy

[5] http://lorimer+11.sourceforge.net/

PsrPopPy software package can be found in (Bates et al., 2014).

2.5.1 Generating Pulsar Population PDFs

In order to deduce the sizes of the underlying Galactic normal and millisecond pulsar populations, we compared the results of PsrPopPy simulations to the PALFA precursor survey's detection statistics for each of these two classes of pulsar. In each case, we made a set of assumptions about the underlying population (see Table 2.4) and drew spatial and intrinsic pulsar parameters from assumed distributions to form a synthetic Galactic population. We simulated a survey of this synthetic population by computing $(S/N)_{th}$ as was discussed in §2.10. Again, detections were then defined as sources with $(S/N)_{th} > 9$. The assumptions that went into our simulations, outlined in Table 2.4, were largely drawn from the work by Lorimer et al. (2006b) for the normal pulsar population. In that paper, however, the luminosity distribution for normal pulsars was assumed to behave as a power law with a low-luminosity cutoff of 0.1 mJy kpc^2. Since the PALFA precursor survey's sensitivity dips below this cutoff value in some cases, we instead adopt a log-normal luminosity distribution, introduced by Faucher-Giguère & Kaspi (2006).

Since far fewer MSPs are known, we have very little information about the population's spatial and intrinsic parameter distributions, so some assumptions are simply adopted from the normal pulsar population (luminosity and radial distributions), while others are grounded in some preliminary experimental results (scale height, period and duty cycle distributions). In this case, we used a Gaussian radial distribution with a standard deviation of 6.5 kpc and an exponential scale height larger than that of normal pulsars to reflect the fact that MSPs are distributed more uniformly across the sky. The Gaussian radial model for MSPs in the Galaxy is similar to that of normal pulsars, but makes no assumption about a deficiency of sources toward the Galactic center, an effect observed from full *normal* pulsar population synthesis and modeled with a Gamma function (Lorimer et al., 2006b).

We adopted the period distribution shown in Figure 2.9 from Lorimer (2013), where it was

Figure 2.4: This histogram shows the ad-hoc MSP period distribution used in simulations, which peaks at periods close to 3–ms. A more precise, empirically-based distribution is forthcoming and will be based on MSPs detected in the PMPS and HTRU surveys.

initially realized by adjusting the weights of various bins from a flat distribution (in $\log P$) until preliminary simulations matched the sample of observed MSPs from PMPS. Unlike normal pulsar duty cycles, which show inverse proportionality to the square root of spin period (i.e. shorter-period pulsars have wider pulses), MSPs tend to exhibit relatively constant duty cycle across period, with larger scatter about some mean value than the normal pulsar population (Kramer et al., 1998; Smits et al., 2009). Therefore, our simulations assumed MSP duty cycles to be independent of period.

To make the simulated detections as realistic as possible, we used precursor survey parameters in signal-to-noise ratio calculations, and modified PsrPopPy to accept the survey's true pointing positions, as well as corresponding integration times and specific beam gain values. For each population class, we performed simulated precursor surveys across a range of trial population sizes (85,000–130,000 for normal pulsars and 5,000–50,000 for MSPs). For each trial, we performed 2,000 simulated realizations of independent Galactic populations for MSPs and normal pulsars respectively. To form a likelihood function describing pulsar population size, we compared the results of these simulations to the true number of detections for each population class in the precursor survey. The precursor survey only detected a single MSP (B1937+21), so the likelihood was computed by dividing the number of simulations that resulted in a single detection by the total number of simulations at that population size.

Of the 45 detections listed in Table 2.3, we exclude B1937+21 (MSP) from our normal pulsar analysis. Although J1906+0746 is in a binary system, it is a young pulsar with a characteristic age of 112 kyr and has likely not undergone recycling from its companion, so we include it in our analysis. The likelihood function was formed by dividing the number of simulations that detected 44 pulsars by the total number of simulations at a given trial population size. We fit binomial distributions to simulated likelihood functions for normal and MSP populations (shown in Figure 2.10) in order to smooth simulation results and provide integrable functions to determine confidence intervals. For an underlying population of size N, a given simulation has n successes (detections) and $N - n$ failures (non-detections); these kinds of binary outcomes are nicely modeled by binomial distributions.

The binomial distributions provide the functional form

$$p(n|N,\theta) = \frac{N!}{n!(N-n)!}\theta^n(1-\theta)^{N-n}, \tag{2.4}$$

which describes the probability of drawing n pulsars from a total population of N given some detection probability θ. To select the θ value that produces posterior PDFs that best match the simulated data, we chose the one that minimized χ^2, computed by comparing simulated to expected population distributions. Finally, the posterior population size PDFs are normalized so that they could be used to quote confidence intervals. With some number n_{success} of successful realizations (simulations in which the target number of detections is reached), the Poissonian error is given by $\sqrt{n_{\mathrm{success}}}$. Data points that reflect the probability of detecting exactly the target number of pulsars at a trial population size and their error bars are multiplied by the same constant required to normalize the best fit PDF. After looking at multiple realizations of the simulated data presented in Figure 2.10

and comparing the standard deviation of data points at each population size to assumed Poissonian error bar magnitudes, we determined that the Poisson model accurately reflects the uncertainties in population sizes.

By integrating the PDFs shown in Figure 2.10, we find the mode and 95% confidence interval for the normal pulsar population size to be $107,000^{+36,000}_{-25,000}$. We find a lower mode for the MSP population size, $15,000^{+85,000}_{-6,000}$ and the high uncertainty in the corresponding 95% confidence interval reflects the fact that our prediction depends on a single MSP detection in the precursor survey. These results describe the respective Galactic pulsar populations that are beaming towards Earth and errors on most likely population sizes account only for statistical uncertainties due to the limited number of detections in the PALFA precursor survey, not for other sources (e.g. uncertainties in scale height, luminosity distribution, electron density model, etc.).

The confidence interval that the precursor survey places on the normal pulsar population is consistent with earlier results; Faucher-Giguère & Kaspi (2006) predict $120,000 \pm 20,000$ detectable normal pulsars, also using a log-normal distribution to model the pulsar luminosity function. The predicted MSP population size is also consistent with previous estimates; the upper limit we find easily encompasses the population size prediction made by Levin et al. (2013), although the lower limit quoted in that paper, $30,000 \pm 7,000$, is more constraining. Neither of these 95% confidence intervals is tight enough to put strict constraints on normal or millisecond pulsar population sizes, but the consistency is encouraging and we expect the full PALFA survey to place much more stringent constraints on these populations when complete.

Figure 2.5: In each plot, black ‘*x*’s show results of 2,000 population simulations at 10 different trial pulsar population sizes. The normal pulsar population PDF (left plot) was constructed with trial simulations using population sizes between 85,000 and 130,000 sources, while the MSP PDF (right plot) used between 5,000 and 50,000 sources in trial simulations. In both cases the black dashed line shows a normalized binomial distribution fit to the data. Using these fits, we find that the most probable *detectable* Galactic normal and millisecond pulsar population sizes are $\sim 107,000$ and $\sim 15,000$ respectively.

2.6 Results & Discussion

Using input parameters from Table 2.4 to generate a synthetic, Galactic normal pulsar population, we found that the PALFA precursor survey should be expected to detect ~ 40 sources. Through periodicity searches, 43 were found, which indicates that current population parameters, initially determined using PMPS results, are already quite accurate. As we mentioned in §2.10.1, three sources that we expected to detect were not detected, but it is common for $(S/N)_{th}$ and $(S/N)_{meas}$ values to not match perfectly. Due to uncertainties in initial flux measurements, there can be as much as ~ 30% fractional error in $(S/N)_{th}$. Referring again to Figure 2.6, we show a general trend towards a slope of unity when plotting theoretical versus measured S/N for the detections made by the precursor survey, but there is significant scatter in these comparisons. Scatter like this can be caused by scintillation, RFI, poor prior flux measurements or some combination of all of these.

The precursor survey discovered 11 pulsars, four of which fell inside the region overlapping PMPS, allowing us to directly compare their respective sensitivities. While PMPS detected almost three times as many sources in this region, this discrepancy was largely due to the differences in sky coverage — PMPS covered this area uniformly, while the precursor survey had large blocks of coverage missing and slight gaps between pointings due to a “sparse sampling” technique. In fact, only ~ 25% of the overlap region was covered by the precursor survey to a sensitivity greater than or equal to that of PMPS. Even so, the PALFA precursor survey discovered four pulsars that PMPS missed; two of these four were retroactively found by reanalyzing archival data but the others (J1904+0738 and J1905+0902) have high dispersion measures and very low fluxes — an encouraging, albeit small, piece of evidence that Arecibo’s sensitivity gives PALFA a glimpse at fainter and more distant pulsars. Figure 3 in Nice et al. (2013) uses more recent PALFA discoveries to show further evidence of PALFA probing deeper than previous surveys as do recent discoveries mentioned in Crawford et al. (2012).

We simulated a range of Galactic pulsar populations — both non-recycled and recycled —

of various sizes and used the PALFA precursor survey's detection statistics to place limits on normal and millisecond pulsar population sizes respectively. By comparing experimental results to simulations, we formed PDFs for normal and MSP population sizes, then integrated these PDFs to define confidence intervals.

Assuming the most probable normal and millisecond population sizes according to the simulations described in §2.12.1 are correct, we ran 1,000 trials with the same distribution parameter assumptions for each population to determine the most likely number of detections by the beginning of 2014 and after PALFA is complete. Averaging the results of these 1,000 trials in each case, we determine a predicted number of detections, then quote errors that are directly proportional to the 95% confidence limits from normal and millisecond pulsar population PDFs. Following this procedure, we expect the full PALFA survey to detect $1,000^{+330}_{-23}$ normal pulsars (this includes previously known sources that are re-detected) and 30^{+200}_{-20} MSPs. Identical estimation techniques predict that 490^{+160}_{-115} normal pulsars and 12^{+70}_{-5} MSPs should have been detected by the beginning of 2014, but at the time, PALFA had detected 283 normal pulsars and 31 MSPs, respectively[6].

The discrepancy between observed and predicted detection rates is notable for the normal pulsar population. Given the numbers quoted here, PALFA has currently detected just over 50% of the expected number of normal pulsars, according to simulations. These simulations do not yet take into account the local RFI environment of the PALFA survey, which certainly plays a role in the perceived dearth of pulsar detections as of early 2014. Two pulsars that went undetected by both QUICKLOOK and PRESTO 1 pipelines in the precursor survey, J1906+0649 and J1924+1631, provide evidence that initial processing techniques were not optimal and improvements are necessary. In repeated simulations of precursor detections in the inner Galaxy region, we find $30-50\%$ of simulated, detectable sources had S/N values between 9 and 15 (just above the detection threshold). In the precursor survey, only about 10% of detections had $(\mathrm{S/N})_{\mathrm{meas}}$ values in this regime. Although the precursor survey discovered mostly low flux density sources, the fact that only a small fraction of detections were near the S/N threshold suggests that some sources were missed

---

[6] See http://www.naic.edu/~palfa/newpulsars for discoveries; re-detected sources are as yet unpublished.

or assumptions that determine our sensitivity curves are not entirely correct.

A potential factor of two lower sensitivity to normal pulsars because of RFI would bring the survey yield and simulated population into agreement. The most recent PALFA survey pipeline is described in depth in Lazarus et al. (2015) and that paper also constructs PALFA's "true" sensitivity curve, taking into account the RFI environment by injecting artificial signals of varying strength into real data. In future work, we will reprocess precursor survey data with the current pipeline to see if it improves the shortcomings of earlier versions (e.g. inconsistent detection statistics, noted in Table 2.3).

The assumed radial distribution of pulsars in the Galaxy (see Table 2.4) could also contribute to the discrepancy between expected (simulated) and true pulsar yields. Since the distribution is based on extrapolated results from the PMPS, which surveyed higher-populated regions of the sky, population density estimates for longitudes farther from Galactic center may be inaccurate. Over-estimated pulsar population densities in the Galactic longitude range surveyed by the PALFA precursor survey could be a factor in the discrepancies we find between expected and actual pulsar detections there. Future refinement of pulsar population models using PALFA results will provide consistency checks for existing population model parameters.

We note that the current number of MSPs detected by PALFA is consistent with predictions, but this is not surprising, given the high uncertainties in our model due to the precursor survey only detecting one MSP. As the number of detections increases, future predictions will be far more constraining so that we can re-examine initial assumptions about the MSP population characteristics.

Future population studies with the complete PALFA survey will contribute substantially to current population models because of the Galactic longitude ranges covered and Arecibo's unrivaled sensitivity (especially in the millisecond pulse period regime). As the number of normal and millisecond pulsar detections increases, our ability to refine specific, simulated model parameters that describe each underlying population will improve significantly.

2.7 Acknowledgements

The Arecibo Observatory is operated by SRI International under a cooperative agreement with the National Science Foundation (AST–1100968), and in alliance with Ana G. Méndez-Universidad Metropolitana, and the Universities Space Research Association. MAM and JKS are supported through NSF PIRE award #0968296. DJN is supported through NSF grant #0647820. VMK was supported by an NSERC Discovery and Accelerator Grant, the Canadian Institute for Advanced Research, a Canada Research Chair, Fonds de Recherche Nature et Technologies, and the Lorne Trottier Chair in Astrophysics. JWTH acknowledges funding from NWO and ERC. Work at Cornell was supported by NSF Grants #0507747 and #1104617 and made use of the Cornell Center for Advanced Computing. Pulsar research at UBC is supported by an NSERC Discovery Grant and Discovery Accelerator Supplement and by the Canada Foundation for Innovation. PL acknowledges support of IMPRS Bonn/Cologne and NSERC PGS–D.

2.8 Introduction

Our current knowledge of the non-recycled (hereafter *normal*) pulsar and millisecond pulsar (MSP) Galactic populations[1] — their spatial, period and luminosity distributions — primarily comes from the results of the Parkes Multibeam Pulsar Survey (PMPS; Manchester et al., 2001; Morris et al., 2002; Kramer et al., 2003; Hobbs et al., 2004; Faulkner et al., 2004; Lorimer et al., 2006b). Analyses of these results have shown that the Galactic normal pulsar population is made up of 30,000±1,100 sources beaming toward Earth with luminosities above 0.1 mJy kpc^2; their radial density profile is best described by a gamma function and their distance from the Galactic plane, by an exponential function with a scale height of 0.33 kpc (Lorimer et al., 2006b). A more physically

---

[1] Although a number of traits separate normal from millisecond pulsars, the most distinct is an MSP's short spin period, which is the result of angular momentum transferred by material from a binary companion. For the remainder of this paper, we use $P = 30$ ms and $B_{\rm surf} = 10^{10}$ G as period and surface magnetic field thresholds to differentiate between MSPs ($P < 30$ ms, $B_{\rm surf} < 10^{10}$ G) and normal pulsars ($P > 30$ ms, $B_{\rm surf} > 10^{10}$ G), although there are certainly exceptions to this simple separation. A complete list of currently known Galactic MSPs can be found at http://astro.phys.wvu.edu/GalacticMSPs

realistic treatment of pulsar luminosities involves using a log-normal luminosity function, which is demonstrated from pulsar population syntheses (e.g., Faucher-Giguère & Kaspi, 2006). The advantage of this approach is that it allows predictions of the *total* normal pulsar population size — not just the number above a certain luminosity cutoff; Faucher-Giguère & Kaspi (2006) predict that there are 120,000±20,000 detectable, normal pulsars in the Galaxy.

Since there are only ~ 10% as many known MSPs as normal pulsars (Manchester et al., 2005), we do not have the same level of knowledge about recycled pulsars' population parameters. The High Time Resolution Universe (HTRU) Survey (Keith et al., 2010) has added more normal pulsar discoveries to the PMPS haul and many MSPs as well (e.g., Bates et al., 2011; Burgay et al., 2013; Morris et al., 2002; Hobbs et al., 2004; Mickaliger et al., 2012). Recent analysis of the intermediate latitude portion of HTRU MSP detections by Levin et al. (2013) uses a scale factor method (Vivekanand & Narayan, 1981; Lorimer et al., 1993) and 50 detected MSPs to place a lower limit of 30,000±7,000 on the Galactic MSP population size (considering sources whose luminosities exceed 0.2 mJy kpc^2). The scale height of the MSP population is fairly well established to be 500 pc (Lorimer, 2005; Cordes & Chernoff, 1997), but the spatial, period and luminosity functions are currently less well understood. Although many models can be ruled out, plausible MSP populations with a variety of underlying distributions are consistent with the observed sample (Lorimer, 2010).

Despite the fact that Arecibo's latitude does not permit observations close to Galactic center like those at Parkes, the unique combination of Arecibo's sensitivity, paired with the high spectral resolution of its back-ends, provides a much deeper view through the Galaxy's dispersive medium, which often smears out signals from distant sources. Although the PMPS and HTRU surveys have sampled much of the sky surrounding the Galactic center — an area of the sky with high pulsar density — and have discovered over 1,000 pulsars, PALFA provides a glimpse of the population density at larger Galactic radii ($R > 5$ kpc), which will help improve the spatial features of future pulsar population models. Arecibo's ability to reach competitive sensitivity limits with short integration times (1–5 minutes) makes acceleration searches for binaries unnecessary for all but the most exotic systems. Finally, Arecibo's unrivaled sensitivity allows PALFA to probe the low-luminosity end of the Galactic pulsar population, leading to a better understanding of the underlying luminosity distribution.

With Arecibo's unique capabilities, PALFA has great potential to discover many normal pulsars as well as MSPs, thus improving our statistical picture of each population's characteristics. Given the number of discoveries by PMPS, it has historically been used to refine pulsar population modeling assumptions for normal pulsars. Recent efforts have been made to discover additional MSPs in archival PMPS data (Mickaliger et al., 2012) with motivation to improve MSP population models. With higher sensitivity to dispersed sources and MSPs, the PALFA survey's influence on normal and millisecond pulsar population studies will complement those of the PMPS and HTRU surveys. MSPs are essential for the direct detection of gravitational waves by pulsar timing array projects (e.g., Demorest et al., 2013). The best way to increase our sensitivity to the stochastic background is to add new MSPs to the array (Siemens et al., 2013).

In this chapter, we present the detections and discoveries from the initial phase of the PALFA survey, hereafter referred to as the "precursor survey". In §2.9, we describe the PALFA precursor survey parameters and sky coverage and introduce two pipelines used to process the raw data. We present the 45 detections made by the precursor survey in §2.10 and include an evaluation of the survey's efficacy based on measured and theoretically calculated signal-to-noise (S/N) ratios. In §2.11 we discuss the portion of sky in the precursor survey that overlapped with the PMPS and show preliminary evidence that PALFA will indeed be probing more distant, fainter sources. Comparing population simulations to precursor survey detection statistics, we generate probability density functions (PDFs) for normal and millisecond pulsar populations in §2.12. These PDFs inform the predictions we make about the total number of pulsars (normal and MSP) we expect to have detected when the full PALFA survey is complete. We conclude in §2.13, stating the most probable normal and millisecond pulsar population sizes according to the precursor survey results.

2.9 Sky Coverage and Data Analysis

The PALFA precursor survey covered portions of two Galactic sectors — an inner Galaxy region, 36° � £ � 75°, tiled with 865 pointings, and an outer Galaxy region, 170° � £ � 210°, covered by 919 pointings. All pointings were within one degree of the Galactic plane ($|b| < 1^\circ$) and had dwell times of 134 and 67 seconds for inner- and outer-Galaxy regions respectively. The precursor survey used the Arecibo L-band Feed Array (ALFA) 7-beam receiver in conjunction with the Wideband Arecibo Pulsar Processor (WAPP) back-end (Dowd et al., 2000), which was set up to record 256 channels covering a 100 MHz bandwidth, centered at 1.42 GHz, every 64 μs. Each ALFA pointing includes seven distinct beam positions in a hexagonal pattern. As PALFA continues, the sky coverage will increase slightly in Galactic longitude (32° � £ � 77° and 168° � £ � 214°) and will extend to Galactic latitude ±5°. For the remainder of the paper, we will refer to this extended spatial coverage (accompanied by a three-fold increase in bandwidth) as the *full PALFA survey*. The precursor survey, optimized for maximum efficiency and sensitivity, used a “sparse sampling” technique described in detail in Cordes et al. (2006); gaps left by the precursor survey will be covered in multiple passes by the full PALFA survey. PMPS overlaps with the southernmost regions covered by Arecibo in the PALFA precursor survey, corresponding to 36° � £ � 50°. In §2.10, we will compare the performance of the two surveys in this overlap region to make a statement about the efficacy of the PALFA precursor survey.

Data from the PALFA precursor were previously analyzed in Cordes et al. (2006). That analysis used a quasi-real-time Quicklook pulsar search pipeline in which the data were decimated in time and frequency by factors of 8 and 16, respectively, yielding 32 spectral channels and 1024 μs time resolution. Using the decimated data, 11 pulsars were discovered and 29 previously known pulsars were detected. Timing and spectral characteristics from follow-up observations of the newly discovered pulsars are given in Nice et al. (2013).

We have analyzed these same data files at native full time- and frequency-resolution using the PALFA survey’s Presto 1 pipeline. The full resolution search of the precursor survey data did not yield any pulsar discoveries (and in fact missed some sources flagged by the QUICKLOOK pipeline), but revealed two more previously known normal pulsars (J1946+2611, B1924+16) and the bright MSP B1937+21. The PRESTO 1 zaplist, a list of frequencies and their harmonics related to known sources of RFI, may be responsible for this scant improvement over QUICKLOOK results since it was fairly restrictive, “zapping” $\sim 8\%$ of the spectral region between $0-10\,\mathrm{Hz}$ ($\sim 84\%$ of known pulsars have spin frequencies in this range). At least one previously known source, B1925+188, fell inside a zapped portion of the spectrum, but its fourth harmonic was still detectable in PRESTO 1 results. Four other sources that were detected by QUICKLOOK (J1913+1000, B1919+14, J2002+30 and J2009+3326) were not detectable in PRESTO 1 results. Of the 12,488 PALFA precursor beams, 183 (1.5%) were not processed by the PRESTO 1 pipeline, including beams where J1913+1000 and B1919+14 should have been detected. PSRs J2002+30 and J2009+3326 were processed by PRESTO 1 and their spin frequencies were outside zapped portions of the spectrum; why these two sources were not detectable remains unknown, although it is plausible that harmonics of their true spin frequencies could have been “zapped,” causing these sources to fall below a detectable threshold.

After the precursor survey was complete, raw data products were decimated to 4-bit resolution and saved in that form. In the process, some files were lost or corrupted (i.e. detection data files for J1913+1000, B1919+14 and B1924+16), so results from Cordes et al. (2006) were used when necessary. We used a complete list of precursor beam positions to determine minimum offset angles from each known source in the survey region, then refolded corresponding 4-bit data files, yielding two additional detections (J1906+0649 and J1924+1631). Table 2.3 outlines the means by which all sources in the PALFA precursor survey were detected.

2.9.1 PRESTO 1 Pipeline

The PALFA PRESTO 1 pipeline[2] used to analyze precursor survey data first converted WAPP-format data to SIGPROC filterbank-format (Lorimer, 2001). Each filterbank file, one per beam, was then processed independently using various programs from the PRESTO suite of pulsar analysis software[3] (Ransom et al., 2002). Strong narrow-band impulsive and periodic signals were identified as interference by `rfifind`. The filterbank files were then cleaned and reduced-frequency-resolution sub-band files were created at various dispersion measures (DMs). Each group of sub-band files was then used to create time series with DMs close to the DM of the sub-band file. In total 1056 trial DM values were used between $0 \leq \mathrm{DM} \leq 1003.2\,\mathrm{pc\,cm}^{-3}$. The upper limit was chosen to reflect the maximum expected DM in the sky region surveyed (Cordes & Lazio, 2002).

Each dedispersed time series was searched for single pulses using `single_pulse_search.py`. Significant pulses ($\sigma > 6$) with widths up to 0.1 s were identified and a diagnostic plot was generated for human inspection. The time series were also Fourier transformed and searched for periodic signals using `accelsearch`. The periodicity search was done in two parts, one for unaccelerated pulsars using up to 16 summed harmonics and the other for accelerated pulsars using up to 8 summed harmonics. The high-acceleration search used a Fourier-domain algorithm (Ransom et al., 2002) with a maximum drift of 50 FFT bins. Non-pulsar-like signals were removed from the candidate lists generated from the low and high-acceleration searches. The manicured low and high-acceleration candidate lists were then combined. Candidates harmonically related to a stronger candidate were discarded, while the top 50 candidates with $\sigma > 6$ were "folded" modulo the best Fourier-detected period using `prepfold`, which effectively provides a fully-coherent harmonic sum of the signal power. The resulting plots, along with basic metadata about the observations were loaded into a database hosted at Cornell University, where volunteers selected and inspected candidate plots.

---

[2] Many of the aspects of the PALFA precursor survey data processing described here have since been augmented (e.g., Lazarus (2013)), including a new complementary pipeline based on the Einstein@Home distributed volunteer computing platform, e.g. Allen et al. (2013).

[3] https://github.com/scottransom/presto

2.9.2 Detection S/N Measurements

For all sources detected by the Quicklook and PRESTO 1 processing pipelines, we refolded data files from beam positions nearest those sources using known pulsar parameters and calculated measured signal-to-noise $(S/N)_{\rm meas}$ values. For each pulse profile, we used a simple algorithm to determine on- and off-pulse bins, then summed on-pulse intensities and divided by the maximum profile intensity to get an equivalent top-hat pulse width $W_{\rm eq}$ (in bins). Finally, $(S/N)_{\rm meas}$ is computed with

$$(S/N)_{\rm meas} = \frac{1}{\sigma_p \sqrt{W_{\rm eq}}} \sum_{i=1}^{n_{\rm bins}} (p_i - \bar{p}), \tag{2.5}$$

as in Lorimer & Kramer (2004), where $\bar{p}$ and σ_p are the mean and standard deviation of off-pulse intensities respectively, p_i is the intensity of an individual profile bin and each profile had $n_{\rm bins} = 128$. We divided $W_{\rm eq}$ by the number of bins in a profile $n_{\rm bins}$ to convert to duty cycle δ for each detection. Computed δ and $(S/N)_{\rm meas}$ values are listed in Table 2.3.

2.10 Survey Results

To measure the effectiveness of a pulsar survey, we look at the known sources that fall inside the survey region and compare the number of detections to the number of expected detections. Effectiveness will then be evaluated by whether the survey meets/exceeds expectations for detecting individual sources.

2.10.1 Defining Detectability

The PALFA multibeam receiver is composed of seven beams, each with an average full width half maximum (FWHM) of $\sim 3.35^{1}$; adjacent beams are separated by $\sim 5.5^{1}$, or ~ 1.6 half-power beam widths. Outer beams and the central beam have gains of 8.2 and 10.4 K Jy^{-1} respectively (Cordes et al., 2006). Although previous population studies have modeled gain patterns using

PSR Name	*P* (s)	DM (pc cm^{-3})	(°)	*b* (°)	$\Delta\theta$ ($'$)	Duty Cycle (%)	Flux Density (mJy)	(S/N)$_{\rm th}$	(S/N)$_{\rm meas}$	Pipeline Detected? (QL / P1 / Refold)	PALFA Discovery?
J0540+3207	0.524	61	176.7	0.8	1.43	2.1	0.34	62.6	32.8	QL, P1, Refold	Yes
J0628+0909	1.241	88	202.2	–0.9	2.30	1.4	0.06	4.6	21.0	QL, P1, Refold	Yes
J0631+1036	0.288	125	201.2	0.5	1.51	3.3	0.80	85.1	104.1	QL, P1, Refold	
J1855+0307	0.845	402	36.2	0.5	3.24	1.7	0.97	12.4	48.4	QL, P1, Refold	
J1901+0621	0.832	94	39.7	0.8	1.76	5.6	0.47	35.2	21.3	QL, P1, Refold	Yes
B1859+07	0.644	252	40.6	1.1	2.29	3.0	0.90	55.1	38.8	QL, P1, Refold	
J1904+0738	0.209	278	41.2	0.7	0.90	1.9	0.23	54.2	20.1	QL, P1, Refold	Yes
J1904+0800	0.263	438	41.5	0.9	1.99	2.8	0.36	41.0	21.2	QL, P1, Refold	
J1905+0616	0.990	256	40.1	–0.2	1.80	1.5	0.51	69.7	47.4	QL, P1, Refold	
B1903+07	0.648	245	40.9	0.1	0.52	5.6	1.80	266.2	171.3	QL, P1, Refold	
J1905+0902	0.218	433	42.6	1.1	0.50	1.9	0.10	21.1	22.2	QL, P1, Refold	Yes
B1904+06	0.267	472	40.6	–0.3	2.43	5.6	1.70	61.8	104.1	QL, P1, Refold	
J1906+0649	1.287	249	40.7	–0.2	2.53	6.3	0.30	9.2	20.2	Refold	
J1906+0746	0.144	217	41.6	0.1	2.60	1.6	0.55	28.8	15.0	QL, P1, Refold	Yes
J1906+0912	0.775	265	42.8	0.9	2.37	2.5	0.32	19.4	14.4	QL, P1, Refold	
J1907+0740	0.575	332	41.6	–0.1	2.24	2.2	0.41	30.5	25.3	QL, P1, Refold	
J1907+0918	0.226	357	43.0	0.7	3.00	1.6	0.29	7.5	21.8	QL, P1, Refold	
J1908+0734	0.212	11	41.6	–0.3	1.05	3.1	0.54	90.1	23.1	QL, P1, Refold	
J1908+0909	0.337	467	43.0	0.5	1.70	2.2	0.22	28.5	60.9	QL, P1, Refold	
B1907+10	0.284	149	44.8	1.0	1.92	2.3	1.90	206.9	83.8	QL, P1, Refold	
J1910+0714	2.712	124	41.5	–0.9	1.72	1.4	0.36	59.8	15.8	QL, P1, Refold	
B1910+10	0.409	147	44.8	0.2	2.32	3.7	0.22	11.0	—	—	
J1913+1000	0.837	422	44.3	–0.2	1.69	3.8	0.53	66.5	26.0	QL	
J1913+1011	0.036	178	44.5	–0.2	2.69	4.1	0.50	14.1	19.9	QL, P1, Refold	
J1913+1145	0.306	637	45.9	0.5	2.06	4.7	0.43	23.4	—	—	
B1911+11	0.601	100	45.6	0.2	1.90	4.2	0.55	43.9	—	—	
B1913+10	0.405	241	44.7	–0.7	1.51	1.6	1.30	238.2	34.6	QL, P1, Refold	
B1914+13	0.282	237	47.6	0.5	1.78	2.4	1.20	152.8	230.4	QL, P1, Refold	
B1915+13	0.195	94	48.3	0.6	2.29	2.5	1.90	131.6	239.9	QL, P1, Refold	
B1916+14	1.181	27	49.1	0.9	3.04	1.4	1.00	26.9	21.7	QL, P1, Refold	
B1919+14	0.618	91	49.1	0.0	0.45	3.6	0.68	140.2	41.0	QL	
B1921+17	0.547	143	51.7	1.0	3.01	3.6	—	—	46.8	QL, P1, Refold	
J1924+1631	2.935	518	51.4	0.3	0.65	1.0	0.09	35.4	10.5	Refold	
B1924+16	0.580	176	51.9	0.1	0.83	2.5	1.30	363.5	90.9	P1	
B1925+188	0.298	99	53.8	0.9	1.92	5.9	—	—	27.8	QL, P1, Refold	
J1928+1746	0.069	176	52.9	0.1	0.70	5.2	0.28	46.9	29.6	QL, P1, Refold	Yes
B1929+20	0.268	211	55.6	0.6	3.78	2.0	1.20	1.7	24.0	QL, P1, Refold	
B1937+21	0.00156	71	57.5	–0.3	2.41	14.9	13.20	327.0	180.5	P1, Refold	
J1946+2611	0.435	165	62.3	0.6	2.61	2.4	—	—	18.5	P1, Refold	
B1952+29	0.427	7	66	0.8	2.53	4.5	8.00	325.8	117.3	QL, P1, Refold	
J1957+2831	0.308	138	65.5	–0.2	1.57	3.6	1.00	131.2	30.0	QL, P1, Refold	
J2002+30	0.422	196.0	67.9	–0.2	1.21	3.7	—	—	60.7	QL, Refold	
B2000+32	0.697	142	69.3	0.9	2.16	1.8	1.20	121.7	49.1	QL, P1, Refold	
B2002+31	2.111	234	69.0	0.0	3.30	1.3	1.80	26.3	94.4	QL, P1, Refold	
J2009+3326	1.438	263	71.1	0.1	0.82	3.0	0.15	32.4	23.9	QL, Refold	Yes
J2010+3230	1.442	371	70.4	–0.5	0.60	2.2	0.12	32.6	23.4	QL, P1, Refold	Yes
J2011+3331	0.932	298	71.3	–0.0	2.50	2.6	0.38	21.2	39.4	QL, P1, Refold	Yes
J2018+3431	0.388	222	73.0	–0.8	1.70	2.0	0.24	47.4	31.7	QL, P1, Refold	Yes

Table 2.3: A comprehensive list of all pulsars detected by the precursor survey as well as those we expected to detect, given their high (S/N)$_{\rm th}$ quantities. We list each pulsar's period (*P*), dispersion measure (DM), Galactic longitude (£), Galactic latitude (*b*), angular offset from the closest beam ($\Delta\theta$) and duty cycle (δ), as well as (S/N)$_{\rm th}$, (S/N)$_{\rm meas}$. PALFA precursor data were run through two processing pipelines, Quicklook and PRESTO 1 (described in §2.9), then converted into 4-bit files and stored. Pulsars detected by Quicklook (QL) or PRESTO 1 (P1) pipelines are marked accordingly; those detected after refolding archived, 4-bit data files have "Refold" in the "Pipeline Detected?" column. Previously unknown pulsars discovered by the precursor survey are marked with a "Yes" in the last column. For sources without an available flux density measurement, we did not compute (S/N)$_{\rm th}$. Previously determined parameters (*P*, DM, £, *b* and flux density) were obtained from the ATNF Pulsar Catalog (Manchester et al., 2005). Missing parameters, (S/N)$_{\rm th}$ and (S/N)$_{\rm meas}$ for example, are denoted by dashes (—).

Gaussian functions (e.g., Lorimer et al., 2006b), we use an Airy disk function to better model the additional gain from the side lobes of individual beams. Although this is not a perfect representation of the PALFA survey's true gain pattern — in fact, the side lobes of the outer ALFA beams are highly asymmetric (see Spitler et al. (2014) for a more precise model) — the Airy disk captures Arecibo's off-axis gain better than the Gaussian model and still provides the simplicity required to run population simulations quickly.

The theoretical signal-to-noise ratio $(\mathrm{S/N})_{\mathrm{th}}$ for a given pulsar with flux density (S_{1400}) measured in mJy at 1400 MHz, spin period P, and pulse width W is given by

$$(\mathrm{S/N})_{\mathrm{th}} = \frac{S_{1400}\, G \sqrt{n_p\, t_{\mathrm{obs}}\, \Delta f}}{\beta\, T_{\mathrm{sys}}} \sqrt{\frac{1-\delta}{\delta}}\,, \qquad (2.6)$$

where $\delta = W/P$ is the pulse duty cycle; G is the gain in K Jy^{-1} of a specific beam, $n_p = 2$ is the number of summed polarizations, t_{obs} is the integration time (134 s and 67 s for inner- and outer-Galaxy observations, respectively), $\Delta f = 100$ MHz is the bandwidth, $\beta = 1.16$ is a correction factor that accounts for losses in the digitization process and T_{sys} is the system temperature measured in K (Dewey et al., 1985). Flux densities S_{1400} were obtained from the ATNF Pulsar Catalog (Manchester et al., 2005) for known pulsars and Nice et al. (2013) for pulsars discovered by the PALFA precursor survey. Equation 2.6 is an approximation since this treatment assumes top-hat pulse profiles and ignores the considerable variability in pulse shape. The majority of pulsars have Gaussian-shaped profiles however, so this approximation works well in most cases.

Hereafter $(\mathrm{S/N})_{\mathrm{th}}$ will refer to theoretical signal-to-noise ratios, computed using Equation 2.6, while $(\mathrm{S/N})_{\mathrm{meas}}$ refers to signal-to-noise ratios measured from PALFA detections as described in §2.9.2 and specifically, Equation 2.5.

Since gain is a function of a source's angular offset from the beam center, we model it as an Airy disk so that the gain

$$G = G_0 \left[\frac{2\, \mathrm{J}_1(k\, a\, \sin(\theta))}{k\, a\, \sin(\theta)}\right]^2, \qquad (2.7)$$

where J_1 is a Bessel function of the first kind, G_0 is the maximum on-axis gain of the beam, $k = 2\pi/\lambda$ is the wavenumber (λ, the observation wavelength), a is the effective aperture radius (~ 220 m), and θ is the angular offset of a source from the beam center, measured in radians. In predicting S/N for a given pulsar, the pulsed nature of its emission must be taken into account, as shown by the final term in Equation 2.6. For all pulsars that were detected in the precursor survey, we computed W_{eq}, then δ as described in §2.9.2. For sources that were not detected, we divide the pulse width at half maximum (W50), from the ATNF Pulsar Catalog (Manchester et al., 2005), by the period to compute δ, then $(S/N)_{\mathrm{th}}$. Finally, T_{sys} includes the receiver temperature ($T_{\mathrm{rec}} = 24$ K) and sky temperature (T_{sky}), which varies as a function of position and frequency as shown by Haslam et al. (1982). Since this sky temperature map describes T_{sky} at 408 MHz, we convert these values into 1.4 GHz sky temperatures using an assumed spectral index of $\alpha = 2.6$, that is $T_{\mathrm{sky}} \propto \nu^{-\alpha}$.

Although there are many factors involved, we assume a 1:1 relationship between $(S/N)_{\mathrm{meas}}$ and $(S/N)_{\mathrm{th}}$ in order to use S/N as a prediction tool for the detectability of known sources. The true relationship between $(S/N)_{\mathrm{meas}}$ and $(S/N)_{\mathrm{th}}$ can be seen in Figure 2.6.

Using a complete list of beam positions, we found the survey observations carried out closest to known pulsars in the precursor region (i.e. minimizing angular offset, θ). For each of these positions, we found the maximum expected gain for a given pulsar using Equation 2.7. Previously measured parameters for known pulsars allowed us to compute a theoretical signal-to-noise, $(S/N)_{\mathrm{th}}$, as shown in Equation 2.6. We define a known pulsar to be detectable if we find $(S/N)_{\mathrm{th}} > 9$ for that pulsar. A full list of pulsars detected by the precursor survey as well as those considered detectable due to their $(S/N)_{\mathrm{th}}$ values can be found in Table 2.3. Before PALFA began, there were 84 known pulsars positioned inside the target precursor survey region, although this sky area was not covered uniformly; 31 of 84 were deemed detectable, while 33 were actually detected, and seven had no previous flux measurements. Of the 51 non-detections, most can be attributed simply to the sources not being close to a PALFA precursor survey beam pointing, as the survey had only limited coverage in this region. Figure 2.7 shows the portion of the precursor survey that overlaps

Figure 2.6: The left plot shows theoretical versus measured S/Ns for each source with both quantities available. If the two values match for a given source, the data point for that source should lie along the solid line with slope unity. The loose correlation shown here is a result of a combination of effects, but most notably, there can be as much as ~ 30% fractional error in $(S/N)_{\rm th}$ due to uncertainties in initial flux measurements, which were taken from the ATNF Pulsar Catalog (Manchester et al., 2005); interstellar scintillation and RFI also contribute to the large scatter. Dashed lines give a reference for sources whose theoretical and measured S/N values are different by a factor of 10. The right plot emphasizes the fact that, in addition to the significant dispersion, $(S/N)_{\rm meas}$ is smaller than $(S/N)_{\rm th}$ in many cases. This systematic offset implies a poor understanding of the noise environment and suggests that the maximum sensitivity limits of the survey have not yet been realized.

with the PMPS), an example of this limited coverage. Three of the 51 non-detections (B1910+10, J1913+1145, and B1911+11) were unexpected, since $(S/N)_{\rm th} > 9$ for these sources; one of the 33 detections (B1929+20) was also unexpected, given its low $(S/N)_{\rm th}$ value. The non-detections could be due to a variety of factors — most likely RFI. Scintillation could have also suppressed the expected signal during precursor survey observations or boosted the signal during initial flux measurements. It is unlikely scintillation affected the detectability of J1913+1145, however, because of this source's high DM (637 pc cm^{-3}). Given the short integration time near each of these sources (134 s), the pulse-to-pulse variability may have strongly affected $(S/N)_{\rm meas}$ since relatively few pulses were recorded. Also, because of the large error bars on $(S/N)_{\rm th}$ (~ 30% fractional error) due to uncertainties in flux measurements, the sources may simply be weaker than expected.

Although most sources with high $(S/N)_{\rm th}$ values were detected by the precursor survey's pro-

Figure 2.7: Beam positions for the PMPS (light gray) and PALFA precursor survey (dark gray) are shown here with known pulsar positions superimposed. The Parkes beam radii are about 4 times as large as those of Arecibo; the points indicating beam positions have been scaled appropriately relative to one another. Only PMPS beams within 1.2° of the Galactic plane are plotted since this more than covers the Galactic latitude limits of the PALFA precursor survey. Of the 58 previously known pulsars plotted here, many were too far from the nearest precursor survey beam center, making them undetectable. Only 24 of 59 were deemed detectable, given the precursor survey's patchy coverage of this Galactic sector, and were considered in comparing the two surveys. Known pulsars detected by the precursor survey are marked with crosses, while expected detections that were missed are marked with open circles. Filled circles indicate the positions of PALFA precursor survey discoveries in the region overlapping with PMPS.

Prior Distribution Parameter	Normal PSR Simulations	MSP Simulations
Luminosity	Log Normal: $\mu=-1.1;\sigma=0.9$	Log Normal: $\mu=-1.1;\sigma=0.9$
Period	Log Normal: $\mu=2.7,\sigma=0.34$	(see Figure 2.9)
Radial	Gamma Function: (see Lorimer et al., 2006b)	Gaussian: $\sigma=6.5$ kpc
Scale height	0.33 kpc	0.5 kpc
Duty Cycle	(explained in §2.12.1)	(explained in §2.12.1)
Electron Model	NE2001	NE2001

Table 2.4: Assumed parameter values/distributions for normal and millisecond pulsar populations respectively. These parameters are used as input values to the appropriate PsrPopPy functions, which generate an underlying, synthetic population. Changing input parameters directly affects the number of detections expected from a given simulated survey.

cessing pipelines, five such sources were not. For each of these cases, we employed the same procedure as introduced in Section 2.9.2, using known periods and dispersion measures to dedisperse and fold the data from the closest pointing to each source. For the three sources mentioned earlier (B1910+10, B1911+11, and J1913+1145), no pulsations were detected; for the other two, J1906+0649 and J1924+1631, pulsations are evident, but relatively weak. PSR J1906+0649 was likely missed because of the RFI environment at Arecibo.

In addition to the 33 re-detected pulsars in the region, PSR J1924+1631 was discovered shortly after the precursor survey was completed, when the PALFA survey underwent an upgrade to a new backend with three times more bandwidth. This source was then retroactively found in precursor survey data with $(S/N)_{\rm meas}$ just above the detection threshold and has therefore been included in analysis that follows. Strong RFI present in the refolded precursor data explains why this source was not discovered earlier. Lazarus et al. (2015) describe the most recent processing pipeline in detail, address the RFI environment and its effect on the PALFA survey's "true" sensitivity.

2.11 PMPS Overlap Region

The PALFA precursor survey region overlaps the region covered by the PMPS in Galactic longitude, 36° � £ � 50°. Although there were 58 previously known pulsars in this longitude range and within $\sim 1^\circ$ of the Galactic plane when the precursor survey took place (see Figure 2.7), we compare the PMPS and precursor survey detections only based on sources deemed detectable by the precursor survey. We justify this criterion based on the fact that, due to patchy coverage, only ~10% of the overlap region lies within an angular offset $\Delta\theta \sim 1.2^{1}$ of a precursor beam center. We choose 1.2^{1} since this is the average angular offset $(\Delta\theta) = \mathrm{FWHM}/2\sqrt{2}$ for the precursor survey. Half of all sources that fall within a radius R = FWHM/2 of the nearest beam center will also be within the average angular offset $(\Delta\theta)$.

The PMPS discovered or detected all 24 of the previously known pulsars in this region considered detectable by the PALFA precursor survey. The precursor survey detected 21 of these, and discovered an additional four sources in this region. The PMPS retroactively detected two of these four precursor discoveries in archival data (e.g., Lorimer et al., 2006b).

One of the three detectable known pulsars that the precursor survey missed, B1910+10, had a $(S/N)_{th}$ value of ~ 11 (see Table 2.3), just above the detectability threshold of $(S/N)_{th} = 9$; the other two, J1913+1145 and B1911+11, were expected to be detected with $(S/N)_{th}$ = 23 and 36 respectively. Error in $(S/N)_{th}$ is ~ 30%, which reflects the error in flux measurements and can easily explain the first non-detection. It is much harder to explain why J1913+1145 and B1911+11 were not detected, given their high $(S/N)_{th}$ values, but other systematics such as RFI and scintillation may explain these discrepancies.

The four precursor survey discoveries — J1901+0621, J1904+0738, J1905+0902 and J1906+0746 — have relatively high dispersion measures and were all detected near the signal-to-noise threshold with $15 < (S/N)_{meas} < 22$, so it is not surprising that they were not detected by previous surveys. PSR J1906+0746 is a 144 ms pulsar in a relativistic, 3.98 hr orbit and was initially missed during manual inspection of PMPS candidate plots due to RFI with a period similar to that of the pulsar (Lorimer et al., 2006a). Both J1906+0746 and J1901+0621 were found retroactively in Parkes data, which was expected, given that both are moderately bright sources with flux densities at 1400 MHz of about 0.5 mJy. The other two discoveries, J1904+0738 and J1905+0902,

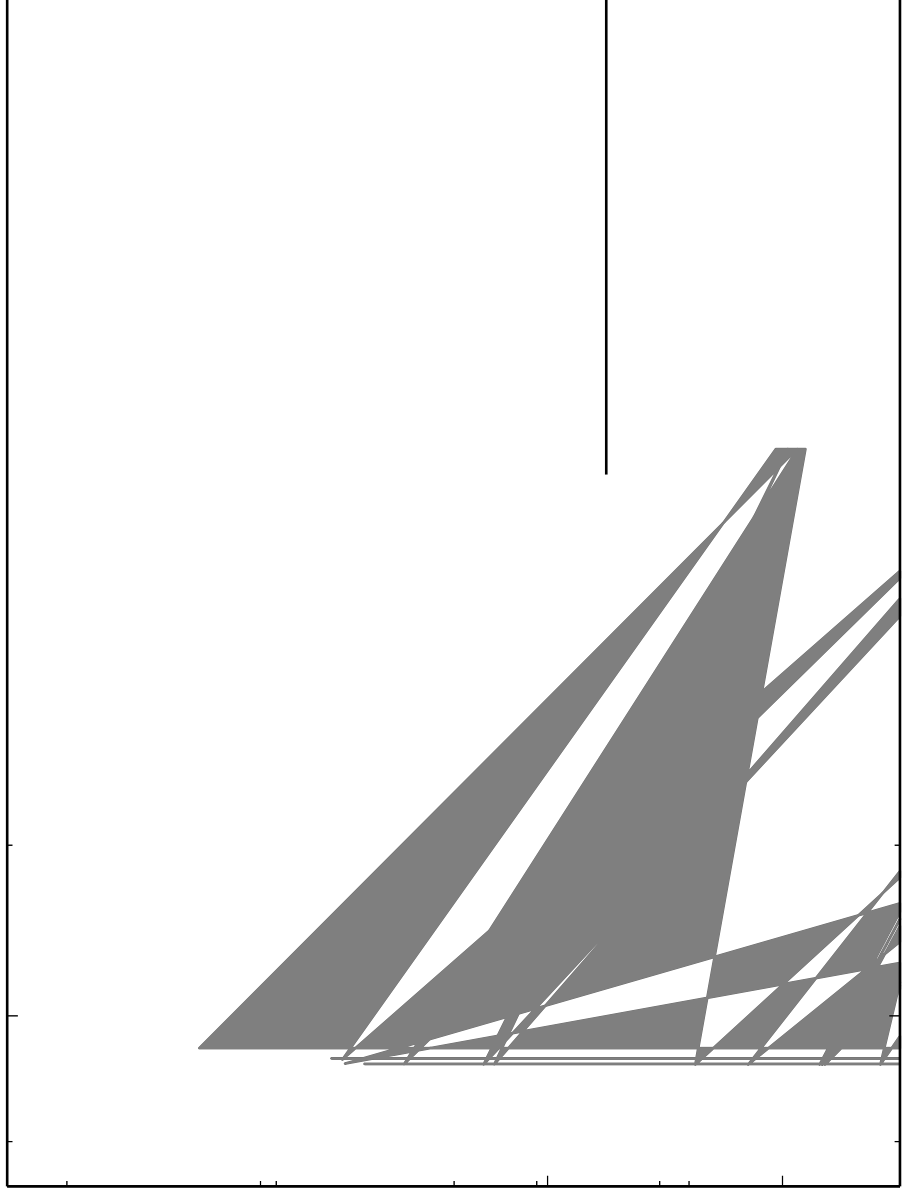

Figure 2.8: Sensitivity as a function of period for the precursor survey is shown in dark gray; the PMPS curve (light gray) is shown here for comparison. The dashed lines in each case show the sensitivity to DM = 100 pc cm^{-3} sources, while upper and lower limits of the shaded regions give minimum flux density sensitivity to pulsars with DM = 150 or 50 pc cm^{-3} respectively. These curves are plotted using the average angular offset $(\Delta\theta)$ between a source and a beam position. For a random distribution of pulsars on the sky, ~ 50% should fall within an angle $(\Delta\theta)$ from the nearest beam position. Precursor survey discoveries are superimposed; expected detections B1910+10, B1911+11 and J1913+1145 that were missed by the PALFA precursor survey, but detected by PMPS are shown with open circles.

are much fainter — 0.23 and 0.097 mJy respectively (Nice et al., 2013). These discoveries show preliminary evidence that with Arecibo's high sensitivity, the PALFA precursor survey probed a deeper and lower-luminosity pulsar population than previous surveys. However, the three unexpected non-detections suggest that the PALFA precursor survey did not realize its full sensitivity and more work is required to better understand Arecibo's RFI environment and develop mitigation techniques.

The relative sensitivity limits as a function of period and DM for the PMPS and precursor surveys are compared in Figure 2.8. To generate these curves, we used an average $T_{\rm sky}$ value for each survey region, assumed a constant pulse duty cycle of $\delta = 0.05$, and applied the empirical pulse broadening function from Bhat et al. (2004) to account for multipath scattering in the interstellar medium. For the three objects that were detected at Parkes, but not in the PALFA precursor survey (B1910+10, J1913+1145 and B1911+11), all have periods between 300 and 600 ms, a regime where the PMPS nominal sensitivity limit in Figure 2.8 is about twice as high as the precursor survey's. However, the angular offsets to these sources (6.6^{1}, 4.7^{1} and 2.5^{1} respectively for PMPS and precursor values can be found in Table 2.3) imply that both surveys were equally sensitive to them since the PALFA precursor beam (FWHM$\sim 3.35^{1}$) is much narrower than that of the PMPS (FWHM$\sim 14.4^{1}$) and its sensitivity therefore drops off more quickly as a function of $\Delta\theta$. Taking angular offsets into account, B1910+10 ($S_{1400} = 0.22$ mJy) falls below the adjusted minimum sensitivity limit (~ 0.26 mJy for both surveys), but B1911+11 and J1913+1145 do not, so angular offsets alone do not explain why these sources went undetected. Since other sources with lower flux densities and similar angular offsets *were* detected (i.e. J0628+0909, J1906+0649, J1906+0912, J1907+0740, J1907+0918, J2011+3331), we conclude that transient effects such as RFI decreased the signal-to-noise ratios of B1910+10, B1911+11 and J1913+1145 and possibly scintillation for the former two.

2.12 Population Analysis

The analysis presented here uses PsrPopPy — a package that models the Galactic population and evolution of pulsars. With this software, we populated a synthetic galaxy with pulsars whose attributes like cylindrical spatial coordinates, period, DM, luminosity, etc. were chosen from predetermined PDFs (Lorimer et al., 2006b). PsrPopPy[4] is a Python implementation of PSRPOP[5], which was written in Fortran (Lorimer et al., 2006b); it shares much of the same functionality, but the object-oriented nature of Python and improved modularity of the code make it more readable and easier to write plug-ins for specific modeling purposes. Additional details describing the PsrPopPy software package can be found in (Bates et al., 2014).

2.12.1 Generating Pulsar Population PDFs

In order to deduce the sizes of the underlying Galactic normal and millisecond pulsar populations, we compared the results of PsrPopPy simulations to the PALFA precursor survey's detection statistics for each of these two classes of pulsar. In each case, we made a set of assumptions about the underlying population (see Table 2.4) and drew spatial and intrinsic pulsar parameters from assumed distributions to form a synthetic Galactic population. We simulated a survey of this synthetic population by computing $(S/N)_{\mathrm{th}}$ as was discussed in §2.10. Again, detections were then defined as sources with $(S/N)_{\mathrm{th}} > 9$. The assumptions that went into our simulations, outlined in Table 2.4, were largely drawn from the work by Lorimer et al. (2006b) for the normal pulsar population. In that paper, however, the luminosity distribution for normal pulsars was assumed to behave as a power law with a low-luminosity cutoff of 0.1 mJy kpc^2. Since the PALFA precursor survey's sensitivity dips below this cutoff value in some cases, we instead adopt a log-normal luminosity distribution, introduced by Faucher-Giguère & Kaspi (2006).

Since far fewer MSPs are known, we have very little information about the population's spatial

---

[4] https://github.com/samb8s/PsrPopPy

[5] http://lorimer+11.sourceforge.net/

and intrinsic parameter distributions, so some assumptions are simply adopted from the normal pulsar population (luminosity and radial distributions), while others are grounded in some preliminary experimental results (scale height, period and duty cycle distributions). In this case, we used a Gaussian radial distribution with a standard deviation of 6.5 kpc and an exponential scale height larger than that of normal pulsars to reflect the fact that MSPs are distributed more uniformly across the sky. The Gaussian radial model for MSPs in the Galaxy is similar to that of normal pulsars, but makes no assumption about a deficiency of sources toward the Galactic center, an effect observed from full *normal* pulsar population synthesis and modeled with a Gamma function (Lorimer et al., 2006b).

We adopted the period distribution shown in Figure 2.9 from Lorimer (2013), where it was initially realized by adjusting the weights of various bins from a flat distribution (in $\log P$) until preliminary simulations matched the sample of observed MSPs from PMPS. Unlike normal pulsar duty cycles, which show inverse proportionality to the square root of spin period (i.e. shorter-period pulsars have wider pulses), MSPs tend to exhibit relatively constant duty cycle across period, with larger scatter about some mean value than the normal pulsar population (Kramer et al., 1998; Smits et al., 2009). Therefore, our simulations assumed MSP duty cycles to be independent of period.

To make the simulated detections as realistic as possible, we used precursor survey parameters in signal-to-noise ratio calculations, and modified PsrPopPy to accept the survey's true pointing positions, as well as corresponding integration times and specific beam gain values. For each population class, we performed simulated precursor surveys across a range of trial population sizes (85,000–130,000 for normal pulsars and 5,000–50,000 for MSPs). For each trial, we performed 2,000 simulated realizations of independent Galactic populations for MSPs and normal pulsars respectively. To form a likelihood function describing pulsar population size, we compared the results of these simulations to the true number of detections for each population class in the precursor survey. The precursor survey only detected a single MSP (B1937+21), so the likelihood was computed by dividing the number of simulations that resulted in a single detection by the total number of simulations at that population size.

Figure 2.9: This histogram shows the ad-hoc MSP period distribution used in simulations, which peaks at periods close to 3–ms. A more precise, empirically-based distribution is forthcoming and will be based on MSPs detected in the PMPS and HTRU surveys.

Of the 45 detections listed in Table 2.3, we exclude B1937+21 (MSP) from our normal pulsar analysis. Although J1906+0746 is in a binary system, it is a young pulsar with a characteristic age of 112 kyr and has likely not undergone recycling from its companion, so we include it in our analysis. The likelihood function was formed by dividing the number of simulations that detected 44 pulsars by the total number of simulations at a given trial population size. We fit binomial distributions to simulated likelihood functions for normal and MSP populations (shown in Figure 2.10) in order to smooth simulation results and provide integrable functions to determine confidence intervals. For an underlying population of size N, a given simulation has n successes (detections) and $N - n$ failures (non-detections); these kinds of binary outcomes are nicely modeled by binomial distributions.

The binomial distributions provide the functional form

$$p(n|N,\theta) = \frac{N!}{n!(N-n)!}\theta^{n}(1 - \theta)^{N-n}, \qquad (2.8)$$

which describes the probability of drawing n pulsars from a total population of N given some detection probability θ. To select the θ value that produces posterior PDFs that best match the simulated data, we chose the one that minimized χ^2, computed by comparing simulated to expected population distributions. Finally, the posterior population size PDFs are normalized so that they could be used to quote confidence intervals. With some number n_{success} of successful realizations (simulations in which the target number of detections is reached), the Poissonian error is given by $\sqrt{n_{\mathrm{success}}}$. Data points that reflect the probability of detecting exactly the target number of pulsars at a trial population size and their error bars are multiplied by the same constant required to normalize the best fit PDF. After looking at multiple realizations of the simulated data presented in Figure 2.10 and comparing the standard deviation of data points at each population size to assumed Poissonian error bar magnitudes, we determined that the Poisson model accurately reflects the uncertainties in population sizes.

By integrating the PDFs shown in Figure 2.10, we find the mode and 95% confidence interval for the normal pulsar population size to be $107,000^{+36,000}_{-25,000}$. We find a lower mode for the MSP population size, $15,000^{+85,000}_{-6,000}$ and the high uncertainty in the corresponding 95% confidence interval reflects the fact that our prediction depends on a single MSP detection in the precursor survey. These results describe the respective Galactic pulsar populations that are beaming towards Earth and errors on most likely population sizes account only for statistical uncertainties due to the limited number of detections in the PALFA precursor survey, not for other sources (e.g. uncertainties in scale height, luminosity distribution, electron density model, etc.).

The confidence interval that the precursor survey places on the normal pulsar population is consistent with earlier results; Faucher-Giguère & Kaspi (2006) predict $120,000 \pm 20,000$ detectable normal pulsars, also using a log-normal distribution to model the pulsar luminosity function. The predicted MSP population size is also consistent with previous estimates; the upper limit we find easily encompasses the population size prediction made by Levin et al. (2013), although the lower limit quoted in that paper, $30,000 \pm 7,000$, is more constraining. Neither of these 95% confidence intervals is tight enough to put strict constraints on normal or millisecond pulsar population sizes, but the consistency is encouraging and we expect the full PALFA survey to place much more stringent constraints on these populations when complete.

Figure 2.10: In each plot, black ‘*x*’s show results of 2,000 population simulations at 10 different trial pulsar population sizes. The normal pulsar population PDF (left plot) was constructed with trial simulations using population sizes between 85,000 and 130,000 sources, while the MSP PDF (right plot) used between 5,000 and 50,000 sources in trial simulations. In both cases the black dashed line shows a normalized binomial distribution fit to the data. Using these fits, we find that the most probable *detectable* Galactic normal and millisecond pulsar population sizes are $\sim 107,000$ and $\sim 15,000$ respectively.

2.13 Results & Discussion

Using input parameters from Table 2.4 to generate a synthetic, Galactic normal pulsar population, we found that the PALFA precursor survey should be expected to detect ~ 40 sources. Through periodicity searches, 43 were found, which indicates that current population parameters, initially determined using PMPS results, are already quite accurate. As we mentioned in §2.10.1, three sources that we expected to detect were not detected, but it is common for $(S/N)_{th}$ and $(S/N)_{meas}$ values to not match perfectly. Due to uncertainties in initial flux measurements, there can be as much as ~ 30% fractional error in $(S/N)_{th}$. Referring again to Figure 2.6, we show a general trend towards a slope of unity when plotting theoretical versus measured S/N for the detections made by the precursor survey, but there is significant scatter in these comparisons. Scatter like this can be caused by scintillation, RFI, poor prior flux measurements or some combination of all of these.

The precursor survey discovered 11 pulsars, four of which fell inside the region overlapping PMPS, allowing us to directly compare their respective sensitivities. While PMPS detected almost three times as many sources in this region, this discrepancy was largely due to the differences in sky coverage — PMPS covered this area uniformly, while the precursor survey had large blocks of coverage missing and slight gaps between pointings due to a “sparse sampling” technique. In fact, only ~ 25% of the overlap region was covered by the precursor survey to a sensitivity greater than or equal to that of PMPS. Even so, the PALFA precursor survey discovered four pulsars that PMPS missed; two of these four were retroactively found by reanalyzing archival data but the others (J1904+0738 and J1905+0902) have high dispersion measures and very low fluxes — an encouraging, albeit small, piece of evidence that Arecibo’s sensitivity gives PALFA a glimpse at fainter and more distant pulsars. Figure 3 in Nice et al. (2013) uses more recent PALFA discoveries to show further evidence of PALFA probing deeper than previous surveys as do recent discoveries mentioned in Crawford et al. (2012).

We simulated a range of Galactic pulsar populations — both non-recycled and recycled —

of various sizes and used the PALFA precursor survey's detection statistics to place limits on normal and millisecond pulsar population sizes respectively. By comparing experimental results to simulations, we formed PDFs for normal and MSP population sizes, then integrated these PDFs to define confidence intervals.

Assuming the most probable normal and millisecond population sizes according to the simulations described in §2.12.1 are correct, we ran 1,000 trials with the same distribution parameter assumptions for each population to determine the most likely number of detections by the beginning of 2014 and after PALFA is complete. Averaging the results of these 1,000 trials in each case, we determine a predicted number of detections, then quote errors that are directly proportional to the 95% confidence limits from normal and millisecond pulsar population PDFs. Following this procedure, we expect the full PALFA survey to detect $1,000^{+330}_{-23}$ normal pulsars (this includes previously known sources that are re-detected) and 30^{+200}_{-20} MSPs. Identical estimation techniques predict that 490^{+160}_{-115} normal pulsars and 12^{+70}_{-5} MSPs should have been detected by the beginning of 2014, but at the time, PALFA had detected 283 normal pulsars and 31 MSPs, respectively[6].

The discrepancy between observed and predicted detection rates is notable for the normal pulsar population. Given the numbers quoted here, PALFA has currently detected just over 50% of the expected number of normal pulsars, according to simulations. These simulations do not yet take into account the local RFI environment of the PALFA survey, which certainly plays a role in the perceived dearth of pulsar detections as of early 2014. Two pulsars that went undetected by both QUICKLOOK and PRESTO 1 pipelines in the precursor survey, J1906+0649 and J1924+1631, provide evidence that initial processing techniques were not optimal and improvements are necessary. In repeated simulations of precursor detections in the inner Galaxy region, we find $30-50\%$ of simulated, detectable sources had S/N values between 9 and 15 (just above the detection threshold). In the precursor survey, only about 10% of detections had $(S/N)_{\rm meas}$ values in this regime. Although the precursor survey discovered mostly low flux density sources, the fact that only a small fraction of detections were near the S/N threshold suggests that some sources were missed

---

[6] See http://www.naic.edu/~palfa/newpulsars for discoveries; re-detected sources are as yet unpublished.

or assumptions that determine our sensitivity curves are not entirely correct.

A potential factor of two lower sensitivity to normal pulsars because of RFI would bring the survey yield and simulated population into agreement. The most recent PALFA survey pipeline is described in depth in Lazarus et al. (2015) and that paper also constructs PALFA's "true" sensitivity curve, taking into account the RFI environment by injecting artificial signals of varying strength into real data. In future work, we will reprocess precursor survey data with the current pipeline to see if it improves the shortcomings of earlier versions (e.g. inconsistent detection statistics, noted in Table 2.3).

The assumed radial distribution of pulsars in the Galaxy (see Table 2.4) could also contribute to the discrepancy between expected (simulated) and true pulsar yields. Since the distribution is based on extrapolated results from the PMPS, which surveyed higher-populated regions of the sky, population density estimates for longitudes farther from Galactic center may be inaccurate. Over-estimated pulsar population densities in the Galactic longitude range surveyed by the PALFA precursor survey could be a factor in the discrepancies we find between expected and actual pulsar detections there. Future refinement of pulsar population models using PALFA results will provide consistency checks for existing population model parameters.

We note that the current number of MSPs detected by PALFA is consistent with predictions, but this is not surprising, given the high uncertainties in our model due to the precursor survey only detecting one MSP. As the number of detections increases, future predictions will be far more constraining so that we can re-examine initial assumptions about the MSP population characteristics.

Future population studies with the complete PALFA survey will contribute substantially to current population models because of the Galactic longitude ranges covered and Arecibo's unrivaled sensitivity (especially in the millisecond pulse period regime). As the number of normal and millisecond pulsar detections increases, our ability to refine specific, simulated model parameters that describe each underlying population will improve significantly.

2.14 Acknowledgements

The Arecibo Observatory is operated by SRI International under a cooperative agreement with the National Science Foundation (AST–1100968), and in alliance with Ana G. Méndez-Universidad Metropolitana, and the Universities Space Research Association. MAM and JKS are supported through NSF PIRE award #0968296. DJN is supported through NSF grant #0647820. VMK was supported by an NSERC Discovery and Accelerator Grant, the Canadian Institute for Advanced Research, a Canada Research Chair, Fonds de Recherche Nature et Technologies, and the Lorne Trottier Chair in Astrophysics. JWTH acknowledges funding from NWO and ERC. Work at Cornell was supported by NSF Grants #0507747 and #1104617 and made use of the Cornell Center for Advanced Computing. Pulsar research at UBC is supported by an NSERC Discovery Grant and Discovery Accelerator Supplement and by the Canada Foundation for Innovation. PL acknowledges support of IMPRS Bonn/Cologne and NSERC PGS–D.

Chapter 3

The Pulsar Search Collaboratory

Rosen et al. 2013, ApJ, 768, 85[1]

3.1 Introduction

The Pulsar Search Collaboratory (PSC) is a joint outreach program between NRAO and WVU; it involves high school students directly in pulsar data analysis in the hopes of getting these students interested in science, technology, engineering and mathematics (STEM) related career paths. The project was initially funded by a 3-year NSF ITEST grant (#0737641), which was extended for an additional two years to continue running summer workshops in Green Bank, WV and "capstone" events at WVU through the 2012–2013 school year. During these events, students were exposed to STEM-related talks, demonstrations and activities with a focus on radio astronomy, stellar evolution, pulsars and data analysis. At the culmination of each session, students presented scientific results in the form of talks and posters to their peers.

A full description of the PSC program and its educational impact on students and STEM careers is detailed in Rosen et al. (2010). Between 2008 and 2013, over 2,500 students and 100 teachers from 18 states participated in the PSC program. From both a scientific and educational perspective, the PSC has been a success. In addition to the scientific discoveries outlined in this paper, the PSC program has reached significant educational goals. These are discussed in Rosen et al. (2010) and the highlights are: the PSC is reaching low-income students and attracts students who are first generation college-goers; the PSC succeeds in building confidence in students, rapport with the

---

[1] The results presented in this chapter come from timing analysis I contributed to Rosen et al. (2013). I have added an initial timing solution for the recent discovery J1955+10 and updated solutions for J1400–1432 and J1821+0155. Thanks to Rachel Rosen, Maura McLaughlin, Duncan Lorimer and Sue Ann Heatherly, who built the Pulsar Search Collaboratory. Thanks to Paul Ray, who performed the detailed γ-ray analysis of 2FGL J1400.7$-$1438.

scientists involved in the project, and greater comfort with teamwork; we see additional gains in girls as they see themselves more as scientists after participating in the PSC program. This result is exciting and significant as self-efficacy is an important predictor of success in STEM fields.

In this chapter, we first describe the 350 MHz drift scan survey in §3.2, including the portions of sky covered, observing set-up, the processing pipeline and data analysis procedure. In §3.3 we discuss survey sky coverage, the total number of detections and shared properties of those sources. In §3.4, we discuss individual PSC discoveries in detail, paying special attention to a bright and nearby millisecond pulsar, a rapidly-spinning, isolated “disrupted recycled pulsar" and a long-period pulsar with a high nulling fraction. Chapter 4 of this thesis will be entirely devoted to J1930−1852, a mildly-recycled pulsar in a double neutron star system; that pulsar will only be mentioned in passing here.

3.2 The 350 MHz drift scan survey

The 100 m Robert C. Byrd Green Bank Telescope (GBT) is a 17 Million pound scientific instrument; it has approximately two acres of collecting area and stands nearly as tall as the Washington Monument, making it the largest movable structure in the world. In 2007, the track beneath the GBT needed to be replaced due to unanticipated wear and tear. That summer, the telescope needed to remain stowed for long stretches of time, so pulsar astronomers took advantage of this downtime to conduct the 350 MHz drift scan survey.

Most pulsar surveys are pointed, meaning particular sky positions are tracked over the course of an observing scan, but blind in the sense that we have no prior knowledge of where a pulsar will be in the survey area. In a drift scan survey, the telescope remains fixed while the Earth rotates and the sky drifts by overhead. During the summer of 2007, the telescope was parked at an azimuth of $\sim 229^\circ$ for the first half of the summer, allowing drift scan observing between declinations $-8^\circ < \delta < +38^\circ$. For the second half of the summer it was parked at azimuth $\sim 192^\circ$, providing access to declinations $-21^\circ < \delta < +38^\circ$ for the remaining observations.

Since the sky drifts at a rate of ~0.25 °/min and the full width of the GBT's 350 MHz beam is just over 0.5 ° (roughly the angular size of a full moon), a point source like a pulsar takes 140 s to drift across the beam and through its axis. Therefore, long scans were broken into 140 s chunks called pseudo-pointings, equal to a pulsar's transit. Consecutive pseudo-pointings overlapped by 50% to ensure that pulsar signals were not split significantly between pointings. To retain full sensitivity in this way, overlapping scans were processed separately, so 350 MHz drift scan data were effectively processed twice.

In §1.4, I provided a detailed comparison between low- and high-frequency pulsar surveys – strategic advantages and disadvantages of each and respective sensitivities as functions of P and DM. For regions of sky off the Galactic plane (where the combined effects of high background sky temperatures, scattering and dispersive smearing degrade low-frequency survey sensitivity), conducting a pulsar survey at 350 MHz has several advantages. Since the beam size is inversely proportional to the observing frequency, a larger area of sky can be covered in less time with a low-frequency survey; for a drift scan survey, a larger beam also means a longer dwell time on a specific sky position drifting overhead. Finally, pulsars are steep-spectrum objects, so they are typically much brighter at low frequencies.

Between May and August of 2007, the 350 MHz drift scan survey collected 1,491 hours (134 TB) of data, covering a total sky area of 10,347 deg^2. Although the majority of these data were analyzed by professional astronomers, about 20% (~2,800 deg^2) were set aside for trained high-school students involved in the PSC to analyze. Before analysis, all pseudo-pointings were processed by the same pipeline using the PRESTO[2] pulsar software package (Ransom, 2001).

3.2.1 Data processing and analysis

The 350 MHz drift scan survey used the Spigot autocorrelation spectrometer (50 MHz bandwidth), accumulating 2048 three-level auto-correlation functions in 8-bit registers every 81.92 μs.

---

[2] https://github.com/scottransom/presto

After breaking long scans into overlapping, 140 s pseudo-pointings, PRESTO's `rfifind` was run on each pointing to identify obvious radio frequency interference (RFI). Bad channels and subintegrations were masked, and then pointings were downsampled (consecutive samples summed) by factors of 2, 4, 8, 16 and 32. At progressively higher DMs, dispersion broadening (Equation 1.19) causes smearing over individual frequency channels; downsampling helps speed up the search process without sacrificing sensitivity. The 350 MHz drift scan survey processing pipeline dedispersed every pseudo-pointing with a search scheme that included 9,700 DMs from $0-1015.5\,\mathrm{pc\,cm^{-3}}$.

All the dedispersed timeseries were Fourier-transformed to look for periodicities in the data. In the frequency domain, low-frequency candidates were ignored and obvious RFI and harmonics, masked in known frequency regimes (e.g. 60 Hz spike due to alternating current in power lines). Next, we searched the frequency-domain power spectrum for strong, harmonically related signals and summed up to 16 harmonics, optimizing our sensitivity to pulsars with narrow pulses. To retain sensitivity to “accelerated" sources – e.g. pulsars in tight binary orbits – we repeated the process, this time allowing a drift of up to 50 Fast Fourier Transform (FFT) bins and summing up to 8 harmonics. The top 20 candidates from the non-accelerated search and 10 candidates from the acceleration search were folded with PRESTO's `prepfold` routine and diagnostic plots were created for inspection.

Although the vast majority of pulsars have been detected with similar FFT searches, a subpopulation – Rotating Radio Transients (McLaughlin et al., 2006, RRATS) – is characterized by more sporadic, bursty emission with long pulse periods (1–10 s). Therefore, we also searched dedispersed timeseries for high-significance single pulse candidates. A matched-filter technique used boxcar functions of varying width to identify and save single pulse events with high signal-to-noise, S/N> 5. Single pulse candidates were summarized in an additional 5 diagnostic plots per pseudo-pointing, each covering different DM ranges.

After this process, PSC students began analyzing diagnostic plots from ∼300 hours of drift scan data. Since 35 diagnostic plots were generated for each of ∼16,500 pointings and due to

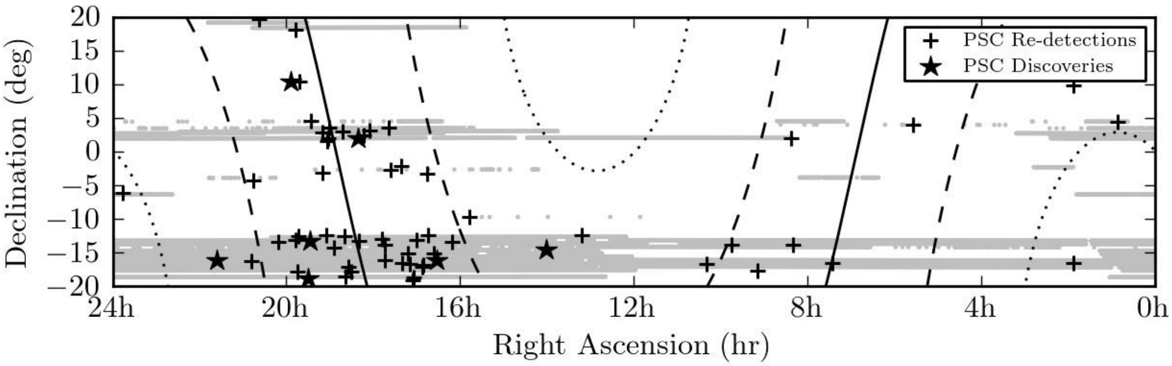

Figure 3.1: PSC drift scan pseudo-pointings are shown in gray; stars and crosses show positions of PSC discoveries and re-detections of known sources respectively. The Galactic plane is overlaid as a solid line. Dashed lines show ±30 ° latitude and dotted, ±60 °. Galactic Center is located at RA 17:45:40.04, Dec −29:00:28.1, which explains why the low declination region between RA 16−20 h contains the highest density collection of PSC detections.

overlapping pseudo-pointings, pointings were effectively processed twice, students had over a million candidate plots to analyze. Before gaining access to the database, PSC students are trained and must demonstrate their understanding of pulsar survey data analysis by passing two pre-tests, which each consist of 35 hand-picked candidate plots with examples of noise, RFI and known pulsars to be identified. The database holds 1,000-1,500 pointings at a time and each must be scored five times before it is considered “fully analyzed” and replaced, but only one student from each school can score a given pseudo-pointing.

Redundancy is built into the analysis procedure to prevent weak sources from being overlooked. Analyzing individual plots consists of assigning a score (1-3) to subplots of single pulse/periodicity candidates respectively, where 1 is not similar and 3 is similar to characteristics expected of pulsars. Students also classify the candidate as noise, RFI or a new/known pulsar so that it can be properly categorized in the database. The highest-ranked new pulsar candidates are then considered for follow-up observations.

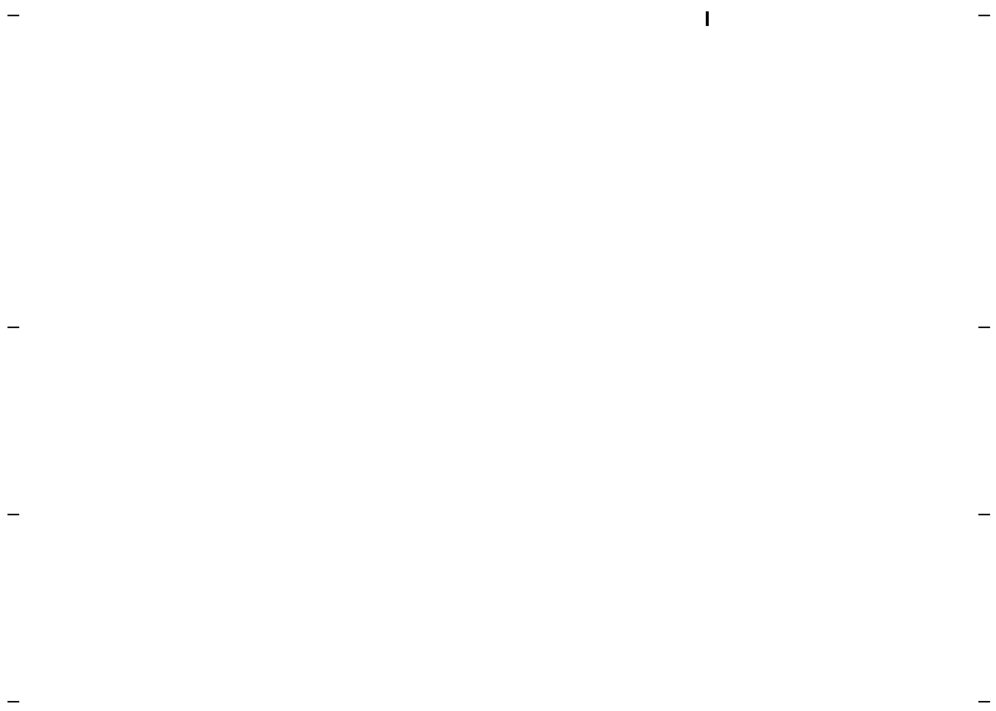

Figure 3.2: Periods and period derivatives of all known pulsars in the Galactic disk (dots), PSC discoveries (stars) and re-detections (crosses). The dashed lines represent constant magnetic field strength and dot-dash lines, constant characteristic age (e.g. Lorimer & Kramer (2004)). The PSC discoveries and re-detections cover most of the evolutionary outcomes seen in the entire pulsar population. Students have discovered three canonical pulsars, one long-period nulling pulsar, a pulsar in a wide double neutron star system, a disrupted recycled pulsar and a millisecond pulsar. No pulsars with characteristic ages less than ~1 Myr were detected.

3.3 Survey Sky Coverage and Detections

Of the approximately 16,500 pseudo-pointings in the PSC database, the students have completely analyzed $\sim$85% of the data available. As a result, students have discovered seven new pulsars, on average one new pulsar per 2,000 pseudo-pointings, where a given pulsar can be discovered by multiple students. By comparison, the astronomical community analyzed approximately 61,200 pseudo-pointings in the remaining drift scan data, discovering 31 new pulsars (Boyles et al., 2013; Lynch et al., 2013), resulting in a discovery rate of one new pulsar per 1,970 pseudo-pointings. Given the random distribution of data between the astronomers and the PSC, and the random pseudo-pointings that students have already analyzed, the detection rate of pulsars from the PSC students is on par with that of the astronomers.

In addition to their seven discoveries, Pulsar Search Collaboratory students have identified an additional 56 previously-known sources, totaling 63 detections. All detections are plotted along with the survey's sky coverage in Figure 3.1 and with the full, Galactic pulsar population in a P-$\dot{P}$ plot shown in Figure 3.2. Although detections from the PSC's portion of the 350 MHz drift scan survey are representative of much of the pulsar population, including sources with a wide variety of evolutionary histories, young pulsars (i.e. those with characteristic ages �1 Myr) are entirely unrepresented. The 350 MHz drift scan survey covers a relatively large fraction of sky off the Galactic plane (see Figure 3.1) and operates at low frequency where sky temperatures are relatively high on the plane. Both of these factors bias PSC detections towards an older subset of the underlying pulsar population since pulsars are born in the Galactic plane and therefore young pulsars are more highly concentrated there. High sky temperatures near the Galactic plane reduce sensitivity to such sources.

3.4 PSC Discoveries

When students identified a promising pulsar candidate and demonstrated that no known pulsars had matching spin period, DM and position, we conducted a confirmation observation at 350 MHz with the GBT. If detected at 350 MHz, we followed up with a second observation at 820 MHz. Because of the smaller beam size at 820 MHz (∼15’), we took a series of gridding observations to determine a more precise location (Morris et al., 2002). A “grid" consists of seven pointings that fully cover the larger 350 MHz beam and a pulsar’s position can be improved by averaging the positions of all grid pointing detections, weighted by their signal-to-noise. Having a more precise initial position allows more flexibility to observe the pulsar at different frequencies, it ensures that the beam axis is closer to the pulsar’s true position during timing observations (resulting in higher significance detections) and it facilitates the process of achieving initial phase connection with pulsar timing. Upon confirmation at 820 MHz, timing observations (§1.2) commenced for each new PSC pulsar.

In addition to further refining a pulsar’s sky position, timing solutions provide measurements of pulsar parameters such as dispersion measure, spin period, period derivative, proper motion, and any orbital parameters of pulsars in binary systems. All gridding observations were conducted at 820 MHz using the Green Bank Ultimate Pulsar Processing Instrument (GUPPI; DuPlain et al., 2008) with 200 MHz bandwidth sampled every 81.92 μs. Routine timing observations for all the pulsars except the MSP (J1400−1432) were conducted at 820 MHz in the same configuration as the gridding observations. For J1400−1432, we carried out timing observations at 350 MHz (using GUPPI, 100 MHz bandwidth and 81.92 μs time resolution) due to the fact that we detected the pulsar more reliably and with higher significance at the lower frequency.

Most of the PSC pulsar timing campaigns began with a series of closely spaced observations followed by monthly observations. Each observation lasts approximately 10–20 minutes. After folding the data modulo each pulsar’s spin period, we selected high S/N detections, summed the data over all subintegrations and frequency channels, then fit 1-3 Gaussians to the resulting pulse profiles in order to create noiseless standard profiles for timing purposes. We generated independent standard profiles for different observing frequencies, then aligned them before using them to generate pulse times-of-arrival (TOAs) with PSRCHIVE[3] (Hotan et al., 2004a).

We follow the procedure for the timing analysis outlined in Boyles et al. (2013), where phase connected timing solutions were created using TEMPO2[4] and the DE405 Solar System ephemeris[5], with the modification that we create three TOAs per epoch for all pulsars if possible, not just binary systems. All of our timing solutions are referenced to UTC(NIST). Global EFACs (multiplicative factors) have been applied to individual TOA errors such that the resulting χ^2 value is one. The parameter uncertainties shown in Tables 3.1, 3.3 and 3.2 reflect 1-σ uncertainties on measured parameters.

In the data that they have examined so far, the students have discovered seven new pulsars, one of which (J1400−1432) is an MSP. We are conducting timing observations on all of them and they are shown on the P-$\dot{P}$ diagram in Figure 3.2. The pulsars discovered by the PSC are indicated with stars and re-detected known pulsars, with crosses. The timing parameters of the four unrecycled pulsars, including their RMS residuals are outlined in Table 3.1 (see §1.2.2 for a detailed description of timing residuals). The three remaining discoveries show evidence of partial to full recycling and we discuss each one separately.

The most recently discovered pulsar, J1955+10, was found in the summer of 2014 and confirmed in the fall (see Figure 3.3). The original candidate showed up only in single pulse plots, but not in the periodicity search. Because of this, we assumed the source was likely a rotating radio transient (RRAT; McLaughlin et al., 2006) and the student who made the discovery led the effort to find the underlying spin period by analyzing single pulse data. After follow-up observations, we solved for the pulsar's spin period. The pulsar was detectable through folding in all subsequent observations.

---

[3] http://psrchive.sourceforge.net

[4] http://tempo2.sourceforge.net

[5] http://iau-comm4.jpl.nasa.gov/de405iom/

We find that the positions obtained with gridding and now timing (timing position listed in Table 3.1) are significantly different from the discovery position (R.A.= $19^{\rm h}55^{\rm m}11.1^{\rm s}$, Decl.= $+10^\circ 19' 08''$), by $\sim 7'$ and $\sim 9'$ respectively. For observations at 350 MHz with the GBT, the telescope's sensitivity to a compact source $9'$ off-axis is reduced by ~15%. It is possible that a weak source that also emits a small percentage of single pulses that exceed our detection threshold could initially appear to exhibit RRAT-like behavior.

We have not yet further investigated J1955+10's single pulse behavior. Based on our spin period and period derivative measurements (see Table 3.3) and its position on the $P-\dot{P}$ diagram (Figure 3.2), it looks like a common example of a canonical pulsar.

Figure 3.3: Residuals in milliseconds for the four, unrecycled PSC discoveries. Shortly after publishing solutions for J1631−1612, J1926−1314 and J2136−1606 (Rosen et al., 2013), timing campaigns for these sources were concluded. For the most recent PSC discovery, J1955+10, we have about a one year span of TOAs — residuals here reflect preliminary fits for position and period derivative (Table 3.1). All residuals represent phase-connected timing solutions with RMS residuals of roughly milli-period precision for each source.

Figure 3.4: Residuals in microseconds for the three recycled pulsars PSC discoveries. Both J1400−1432 and J1821+0155 have RMS residuals of $\sim 3\,\mu$s, close to the precision level of pulsars in PTAs (e.g., Arzoumanian et al., 2015). Detailed timing solutions for these sources can be found in Tables 3.3 and 3.2 and Chapter 4 of this thesis, respectively.

Spin & Astrometric Parameters	PSR J1631−1612	PSR J1926−1314	PSR J1955+10	PSR J2136−1606
Right Ascension (J2000)	16:31:52.47(3)	19:26:53.835(3)	19:54:36.59(8)	21:36:00.22(10)
Declination (J2000)	−16:12:52.0(3.0)	−13:14:03.8(1.8)	+10:21:18(6)	−16:06:13.0(4.0)
Pulsar Period (s)	0.67768391249(4)	4.86428379983(10)	1.04972007500(19)	1.22723540015(6)
Period Derivative (s s^{-1})	$1.096(4)\times10^{-15}$	$3.6440(5)\times10^{-14}$	$6.7(1.9)\times10^{-16}$	$1.6(3)\times10^{-17}$
Dispersion Measure (pc cm^{-3})	33.77(2)	40.83(5)	79.64(4)	18.48(5)
Reference Epoch (MJD)	55766	55791	57033	55764
Span of Timing Data (MJD)	55634–56128	55150–56291	56903–57164	55647–56291
Number of TOAs	65	75	38	71
RMS Residual (ms)	0.8	1.6	2.0	0.7
EFAC	2.9	1.7	0.9	1.9
Derived Parameters				
Inferred Surface Magnetic Field (10^{12} Gauss)	0.87	13.5	0.84	0.14
Spin-down Luminosity (10^{32} erg s^{-1})	1.39	0.13	0.23	0.0035
Characteristic Age (Myr)	10	2.1	25	1180
DM-derived Distance (kpc)	1.9	2.1	3.6	1.3

Table 3.1: Parameters for unrecycled PSC discoveries are shown here. The DM-derived distances were calculated using the NE2001 model of Galactic free electron density (Cordes & Lazio, 2002) and typically have ~20% uncertainty.

3.4.1 PSR J1400−1432

PSR J1400−1432 is the only MSP discovered in the PSC portion of the drift-scan data to date. It has an orbital period of 9.5 days and a projected semi-major axis of 8.4 lt-s, indicating a minimum mass of 0.26 M_0(see Table 3.2 for the orbital parameters), implying that the companion is a WD star. The minimum companion mass and orbital period for PSR J1400−1432 match with the published core-mass–orbital-period relation (Tauris & Savonije, 1999). Tauris & Savonije (1999) show that the companion mass varies slightly for an orbital period, depending on the composition of the donor star. The minimum companion mass of PSR J1400−1432 is 0.26 M_0, which falls between projections for a Population I donor star (0.243 M_0) and a Population II donor star (0.267 M_0).

At a distance of roughly 0.3 kpc (DM of 4.9 pc cm^{-3}; Cordes & Lazio, 2002) and with fluxes of 4.6 mJy and 1.2 mJy at 350 MHz and 820 MHz respectively, it is a bright, nearby pulsar with a moderate spectral index ($\alpha \sim -1.6$). Only four other MSPs have lower DMs than PSR J1400−1432 and three of these are currently included in pulsar timing arrays (PTAs) in the search for gravitational waves.

Rosen et al. (2013) expressed skepticism about J1400−1432's inclusion in PTAs because of its apparent steep spectrum and scintillation behavior. In fact, J1400−1432 was briefly included in NANOGrav[6] PTA observations in 2012, but was dropped soon after being added due to unreliable detections at 820 MHz and none at 1.4 GHz. In the past year, we have revitalized the timing effort on this source after work by Gentile & Swiggum (in prep.) indicated that the timing position published in Rosen et al. (2013) was likely incorrect by $\sim 8^{1}$. A position error would explain frequency-dependent detectability issues, since a radio telescope's beam size is inversely proportional to observing frequency. The vast majority of our follow-up timing effort over the past year has been conducted at low frequency (350 MHz; Figure 3.4) to avoid sensitivity issues due to a possible position error.

---

[6] The North American Nanohertz Observatory for Gravitational Waves.

PSR J1400−1432 Timing Solution

Spin & Astrometric Parameters	
Ecliptic Longitude (J2000)	213.11368136(8)
Ecliptic Latitude (J2000)	−2.1064287(19)
Proper Motion in Ecliptic Lon. (mas/yr)	34.8(2)
Proper Motion in Ecliptic Lat. (mas/yr)	−46(6)
Spin Period (s)	0.00308423326039313(12)
Period Derivative (s/s)	$7.255(4)\times10^{-21}$
Dispersion Measure (pc cm^{-3})	4.93218(4)
Reference Epoch (MJD)	56960
Span of Timing Data (MJD)	55950–57180
Number of TOAs	159
RMS Residual (μs)	3.5

Binary Parameters	
Orbital Period (days)	9.5474676748(15)
Projected Semi-major Axis (lt-s)	8.4212546(4)
Epoch of Ascending Node (MJD)	56958.38397645(7)
First Laplace Parameter	$5.4(9)\times10^{-7}$
Second Laplace Parameter	$5.9(9)\times10^{-7}$

Derived Parameters	
Right Ascension (J2000)	14:00:37.00399(15)
Declination (J2000)	−14:31:47.026(6)
Inferred Surface Magnetic Field (10^9 Gauss)	< 0.08
Spin-down Luminosity (10^{32} erg/s)	< 31
Characteristic Age (Gyr)	> 21
DM-derived Distance (kpc)	0.3
Total Proper Motion (mas/yr)	58(5)
Transverse Velocity (km/s)	74(16)
Shklovskii Effect (s/s)	$6.7(1.7)\times10^{-21}$
Intrinsic Spin-down (s/s)	$< 2.3\times10^{-21}$
Mass Function (M_8)	0.0070345565(10)
Minimum Companion Mass (M_8)	0.26

Table 3.2: All timing solutions use the DE405 solar system ephemeris and the UTC (NIST) time system. For J1400−1432, we use the ELL1 binary timing model, because it is preferable for low-eccentricity orbits. The DM-derived distance was calculated using the NE2001 model of Galactic free electron density (Cordes & Lazio, 2002). We assume ~20% uncertainty on the DM-derived distance and use this value and its error to estimate transverse velocity and the Shklovskii effect and their errors. The minimum companion mass was calculated assuming a pulsar mass, $m_p = 1.35M_0$.

In this chapter, we present a new, phase-connected timing solution for J1400−1432, which incorporates recent TOAs, those presented in Rosen et al. (2013) and TOAs from several early scans at 820 MHz from that study that were not included due to large uncertainties (see Figure 3.4). With TOAs spanning about four years, we have precise measurements of position, period derivative and proper motion in ecliptic longitude; we also show preliminary measurements of proper motion in ecliptic latitude and first and second Laplace parameters. All measured and derived parameters are shown in Table 3.2. The current RMS residuals level (3.5 μs) is above most NANOGrav pulsars — only eight out of 37 have RMS residuals > 1 μs — but due to the significant position error in the preliminary solution from Rosen et al. (2013), J1400−1432 has been off-axis for the majority of observations. At 350 MHz (2048 channels), where we have conducted most of our follow-up timing so far, the dispersive smearing per channel is only ~ 10 μs, so switching from an incoherent to a coherent observing mode to correct for this smearing will not affect our timing precision appreciably. We have not yet made a concerted effort to measure DM as a function of time for J1400−1432, but given its low ecliptic latitude and the signal's significant interaction with the solar wind for several months each year, accounting for its variable DM will improve timing precision. In future observations, with the corrected position and accounting for DM variations over time, we expect the RMS residuals to reach a level competitive with other PTA pulsars.

Although our current fit for proper motion in ecliptic latitude is relatively uncertain as well as our DM-derived distance, the transverse velocity resulting from these quantities, $v_t \sim 75$ km/s is believable and falls inside the expected range for MSPs (85 ± 13 km/s; Toscano et al., 1999). Because of its transverse motion and distance we find that a significant portion (over 90%) of J1400−1432's measured period derivative is due to the Shklovskii Effect (secular acceleration).

Given J1400−1432's DM-derived distance, we expect a signature due to parallax to have an amplitude in the timing residuals of ~4–5 μs; assuming 20% uncertainty in the DM-derived distance and considering the (rough) upper limit on J1400−1432's distance, we find that the parallax's expected residual amplitude drops below our current RMS residuals. Since we do not measure a significant parallax signature in J1400−1432's residuals, the pulsar's distance may be near (or beyond) the upper limit on the DM-derived value. Assuming we can reduce our RMS residuals by a factor of ~ 2 with continued timing (observing J1400−1432 at its true position and measuring its variable DM), we expect to be able to measure parallax. With a corresponding, precise distance measurement, we can use J1400−1432 to measure the electron column density along the line of sight and we may be able to further constrain electron density models at small angular radii from the Sun (Lommen et al., 2006).

PSR J1400−1432 is approximately coincident with unidentified *Fermi* source 2FGL J1400.7−1438. Given that its timing position is on the edge of the 6^{1} 68% confidence region for the source and the non-variability of the *Fermi* source, an association is likely. For the following analysis, we used data from August 4, 2008 to July 15, 2015.[7]

First, we fit the pulsar's γ-ray spectrum with an exponential power law and a pure power law; the exponential power law was favored at the 3-σ level. The *Fermi* energy flux (100 MeV − 100 GeV) for this model is $9.3(7) \times 10^{-12}$ ergs cm^{-2} s^{-1}. Next, we assigned phases to γ-ray photons based on their arrival times and our current timing solution for PSR J1400−1432 (Table 3.2) and performed an H-Test (de Jager et al., 1989), looking for significance of pulsations. We performed this analysis once for the full data set and again using only the MJDs spanned by our timing solution and found weighted H-Test values of about 15 and 20, respectively. Pulsations are only confirmed with a 5-σ detection (H=40), so for now, we are unable to say that J1400−1432 exhibits pulsed γ-ray emission.

3.4.2 PSR J1822+0155

PSR J1821+0155 is unusual in that it has a 33 ms period, a spin down rate of 2.9×10^{-20} s s^{-1}, a weak magnetic field of 1.0×10^{9} G (see Table 3.3), and no companion. Lorimer et al. (2004) interpreted such objects as being disrupted recycled pulsars (DRPs), later defined by Belczynski et al. (2010) as isolated pulsars having $B < 3 \times 10^{10}$ G and $P > 20$ ms.

---

[7] Thanks to Paul Ray, who performed detailed γ-ray analysis of 2FGL J1400.7−1438, given the current timing solution (Table 3.2).

A DRP is thought to emerge from a scenario in which the pulsar is the first born neutron star in a binary system, with a massive companion. As its companion evolves off the main sequence, the pulsar accretes matter from the companion and gains spin angular momentum, which in turn makes the pulsar spin more rapidly and diminishes its inferred surface magnetic field strength. If the companion is sufficiently massive, it will undergo a supernova explosion, accretion will be interrupted and a small fraction of the time, the system will remain gravitationally bound, resulting in a double neutron star (DNS) system (Lorimer et al., 2004). This DNS "survival probability" is only 10%; the other 90% of the time, we expect the system to be disrupted, producing an isolated DRP, much like PSR J1821+0155.

Based on the low "survival probability" of a binary system to remain intact after the second supernova explosion, DRPs are expected to be roughly 10 times as common as DNS binaries in the Galaxy. However, observations indicate that there are comparable numbers of DRPs to DNS binaries. Belczynski et al. (2010) investigate this discrepancy using a sample of eight of the nine known DNS binaries and the 12 known DRPs[8]. They find that for an intermediate natal kick of $\sigma \sim 170$ km s^{-1}, which results in a mean velocity of 99 and 154 km s^{-1} for DNS and DRP populations respectively, there is a small ($\sim 25\%$) observational bias toward detecting DNS binaries. The observational bias in favor of detecting DNS binaries is not enough to explain the discrepancy between the two populations, thus necessitating further study.

In Rosen et al. (2013) the solution for J1821+0155 spanned two years, but with TOAs now spanning almost 4.5 years (see Figure 3.4), we have measured proper motion, as well as a gradient in dispersion measure over time. All measured parameters are listed in Table 3.3. Using the DM-derived distance, computed using the Cordes & Lazio (2002) NE2001 electron density model, we find a transverse velocity for J1821+0155 of $v_t = 65 \pm 13$ km/s, which falls well below Belczynski et al. (2010)'s predicted values for DRPs resulting from binary systems disrupted due to moderate natal kicks ($\sigma \sim 170$ km s^{-1}). Astrometric measurements also indicate that ~28% of the measured

---

[8] Belczynski et al. (2010) exclude 28 isolated pulsars with $B < 3 \times 10^{10}$ G and $P < 20$ ms as they are believed to have evolved from accretion from a low mass companion, such as a white dwarf, over a long period of time, resulting in the evaporation of the companion.

period derivative is due to the Shklovskii effect, thus the intrinsic period derivative is $\dot{P} = 2.2 \times 10^{-20}$ s/s.

3.4.3 PSR J1926−1314

PSR J1926−1314 is notable due to its long period (∼4.9 s, see Table 3.1) and significant nulling fraction. Nulls are times when the radio emission ceases or is greatly reduced. To characterize the nulling fraction in PSR J1926−1314, we analyzed single pulses at both 350 MHz and 820 MHz, following a methodology similar to that of Ritchings (1976). After initially excising any radio frequency interference, we defined on-pulse and off-pulse windows, where on-pulse and off-pulse refer to regions of pulse phase based on integrated intensity. The on-pulse and off-pulse windows have the same number of bins, where the on-pulse window encompasses the entire pulse profile with as little baseline as possible. We then fit a second-order polynomial to the remaining bins and subtracted this from both the on-pulse and off-pulse windows to flatten the baseline. To account for scintillation, for each 200 pulse segment, we normalized the intensity by the average intensity of those 200 pulses ($I/[I]$). Any single pulses with an off-pulse intensity greater than four times the RMS of the off-pulse windows was removed.

Figure 3.5 shows a histogram of the single-pulse intensity for both the on-pulse and off-pulse windows at 350 MHz (top panel) and 820 MHz (bottom panel). To calculate the nulling fraction, we follow the methodology in Wang et al. (2007), where we subtract the on-pulse distribution from the off-pulse distribution, which is multiplied by a trial nulling fraction starting with one and decreasing incrementally until the sum of the difference of the bins with intensities less than zero is equal to zero. The error in the nulling fraction is the square root of the number of null pulses divided by the total number of pulses. The observations at 820 MHz show a slightly higher nulling fraction than those at 350 MHz.

Biggs (1992) analyzed 72 radio pulsars and found that pulsar period is proportional to nulling fraction, consistent with earlier work by Ritchings (1976), and suggested that older pulsars are

PSR J1821+0155 Timing Solution

Spin & Astrometric Parameters	
Right Ascension (J2000)	18:21:38.883306(15)
Declination (J2000)	+01:55:21.9904(4)
R.A. Proper Motion (mas/yr)	$-5.6(2)$
Decl. Proper Motion (mas/yr)	$-1.9(6)$
Spin Period (s)	0.0337813319337547(7)
Period Derivative (s/s)	$2.858(3)\times10^{-20}$
Dispersion Measure (pc cm^{-3})	51.75267(8)
d(DM)/d*t* (pc cm^{-3}/yr)	0.00084(4)
Reference Epoch (MJD)	56337
Span of Timing Data (MJD)	55584–57174
Number of TOAs	169
RMS Residual (μs)	3.5
EFAC	$\sim$1.0

Derived Parameters	
Inferred Surface Magnetic Field (10^9 Gauss)	< 0.90
Spin-down Luminosity (10^{32} erg/s)	< 0.25
Characteristic Age (Gyr)	> 22
DM-derived Distance (kpc)	2.3
Total Proper Motion (mas/yr)	5.9(3)
Transverse Velocity (km/s)	65(13)
Shklovskii Effect (s/s)	$6.6(1.5)\times10^{-21}$
Intrinsic Spin-down (s/s)	$< 2.4\times10^{-20}$

Table 3.3: All timing solutions use the DE405 solar system ephemeris and the UTC (NIST) time system. The DM-derived distance was calculated using the NE2001 model of Galactic free electron density (Cordes & Lazio, 2002). We assume ∼20% uncertainty on the DM-derived distance and use this value and its error to estimate transverse velocity and the Shklovskii effect and their errors. By fitting a constant gradient in 350 MHz TOAs relative to 820 MHz TOAs, we measure d(DM)/d*t* using the full, ∼4.5 yr span of timing data.

harder to detect as they spend more time in their null state. Wang et al. (2007) found that nulling fraction correlates strongly with large characteristic age, even more than pulsar period, and Cordes & Shannon (2008) showed that nulling fraction decreases with period derivative.

Because statistics on nulling pulsars are poor and the number of pulsars discovered in the GBT surveys is small, it is difficult to make any firm statements about the percentage of nullers in our survey compared to others. Of the 31 pulsars discovered in the GBT 350-MHz drift scan survey and the PSC survey combined, three pulsars show a significant nulling fraction. By comparison, the Parkes Multibeam Pulsar Survey (Manchester et al., 2001) recognized significant nulling in 23 pulsars out of the 750 new discoveries of normal pulsars. This could be due to the PSC sky area coverage being away from the Galactic plane where pulsars are more likely to be older and show nulling behavior. In addition, the GBT 350-MHz drift scan survey and the PSC survey are much more sensitive than previous surveys, allowing us to recognize nulling in more pulsars.

3.4.4 PSR J1930−1852

PSR J1930−1852 was discovered and confirmed by two PSC students during the 2012 summer workshop in Green Bank. In the weeks following its discovery, we determined that J1930−1852 is in a binary system, orbiting a massive companion, and through continued follow-up timing, we solved for its binary parameters. Based on the system's orbital eccentricity of ~0.4, we hypothesized that J1930−1852's companion was another neutron star; our hypothesis was confirmed after optical follow-up observations and a timing measurement of the relativistic advance of periastron, $\dot{\omega} = 0.00078(8)\,\mathrm{deg\ yr}^{-1}$, which places a conservative, 2σ lower limit on the mass of the companion, $m_c > 1.30 M_O$.

In Chapter 4, we provide a detailed treatment of J1930−1852, a clear outlier among the small population of double neutron star (DNS) systems. It has the widest orbit of all DNS pulsars and the longest spin period and orbital period of first-born DNS pulsars by factors of two and three respectively. Because its parameters are so different from other first-born DNS pulsars, J1930−1852

Figure 3.5: A histogram of the single pulse intensity of the on-pulse and off-pulse windows at 350 MHz (top panel) and 820 MHz (bottom panel) for PSR J1926−1314. The x-axis is the normalized intensity, which accounts for scintillation effects, and is calculated by taking each pulse in a 200 pulse segment and subtracting the average intensity for those 200 pulses. The solid lines represent the on-pulse windows and the dashed lines represent the off-pulse windows. The on-pulse windows show a significant number of pulses with zero or negligible intensity indicating a large nulling fraction.

may help us better understand and constrain the evolutionary process that results in forming a DNS system (Andrews et al., 2015; Tauris et al., 2015). We are continuing with follow-up timing on this source and will also get precise astrometric measurements (e.g. proper motion, parallax, etc.) with a VLBA imaging campaign scheduled over the next year.

3.5 Conclusion

The PSC has now persisted for four years with little to no funding, but in that time, two scientific papers have been published, reporting six discoveries (J1955+10 remains unpublished). In seven years, over 2,500 students and 100 teachers from 18 states have participated in the PSC; 85 students have made significant contributions to PSC data analysis, earning them co-authorship on one or both of the two publications. In the coming year, the PSC will likely be funded to grow the program, with host institutions across the United States and online training programs and tutorials to facilitate participation for interested students. Although the PSC already offers high school students the unique opportunity to discover new pulsars by analyzing proprietary pulsar survey data, funding for the PSC expansion will provide additional incentive towards imagining new ways to get young scientists involved in current and relevant research.

Four PSC discoveries have interesting properties and two in particular are still being timed regularly, J1400−1432 (§3.4.1) and J1930−1852 (§3.4.4, Chapter 4). PSR J1400−1432 is a bright, nearby millisecond pulsar that has RMS residuals similar to several NANOGrav pulsars that are currently being timed to high precision in an effort to detect gravitational waves. Based on a revitalized timing effort, J1400−1432 looks like a possible addition to pulsar timing arrays; if added, it will act as a bridge, helping PSC students learn about the direct applications of their discoveries. We also hope that in seeing themselves as a part of a larger scientific community (NANOGrav), students will have more interest in pursuing careers in STEM fields.

Chapter 4

PSR J1930$-$1852: a Pulsar in the Widest Known Orbit Around Another Neutron Star

Swiggum et al. 2015, ApJ, 805, 156[1]

4.1 Introduction

To date, ~2,300 pulsars are known (Manchester et al., 2005) and ~10% of them are in binary systems, orbiting white dwarf (WD), neutron star (NS) or main sequence star (MS) companions. The vast majority of these binaries are NS-WD systems; many of these systems emerge from scenarios where the pulsar forms first, followed by its companion, which overflows its Roche Lobe; accretion transfers angular momentum to the pulsar, decreasing the spin period and resulting in a millisecond pulsar (MSP) orbiting a WD (Alpar et al., 1982b). This process of accretion and spin-up is commonly referred to as *recycling* and the period derivative of a recycled pulsar tends to be significantly lower than that of an unrecycled pulsar with the same spin period. There are four observed examples of pulsars orbiting stars that have yet to evolve off the main sequence (Johnston et al., 1992; Kaspi et al., 1994; Stairs et al., 2001; Lorimer et al., 2006b); an additional four have been found with planet-sized companions (Thorsett et al., 1993; Wolszczan, 1994; Bailes et al., 2011; Stovall et al., 2014). More massive companions end their evolution off the main sequence in supernovae, resulting in double neutron star (DNS) systems. DNS systems are far less likely to remain bound than NS-WD systems, since the former must survive two supernova explosions during formation. Only about 10% of these binary systems remain bound after one supernova

---

[1] Thanks to Tyler Hockett, Eugene Filik, James Marlowe – undergraduates from High Point University in North Carolina – and their advisor, Brad Barlow for conducting and describing CTIO optical follow-up observations and for providing Figure 4.5.

explosion (Bailes, 1989). The probability of remaining bound after two supernovae is much lower (~1%) and only nine such systems have been found and studied previously (see references in Table 4.2).

DNS systems have tantalizing applications — for example, testing theories of gravity by measuring relativistic effects (Fonseca et al., 2014; Weisberg et al., 2010; Kramer et al., 2006) and predicting DNS merger rates relevant to ground-based gravitational wave detectors like LIGO (Kim et al., 2010, 2013). DNS systems have also provided some of the most precise NS mass measurements, allowing for a statistical investigation of the underlying mass distribution (Özel et al., 2012; Schwab et al., 2010; Thorsett & Chakrabarty, 1999).

Thorsett & Chakrabarty (1999) used a sample of 26 NSs (21 MSPs and five binary companion NSs) with measured masses to determine a mean NS mass, $\langle m \rangle = 1.35 \pm 0.04\,M_{\odot}$. More recently, Schwab et al. (2010) argue that the underlying NS mass distribution for objects in DNS systems is bimodal, with narrow peaks at $1.246\,M_{\odot}$ and $1.345\,M_{\odot}$. They also suggest that these peaks indicate unique formation scenarios, where the lower mass component represents NSs that formed via electron capture (Nomoto, 1984; Podsiadlowski et al., 2004) and the higher mass component is indicative of iron core-collapse (Woosley & Weaver, 1986). Özel et al. (2012) use a Bayesian statistical approach to infer mass distributions for NSs with distinct evolutionary histories; they agree that NS masses provide clues about respective formation scenarios, however, they express skepticism that NS mass distributions are as narrow as Schwab et al. (2010) claim. Therefore, additional information is necessary in identifying a NS's evolutionary history.

Wong et al. (2010) investigate core-collapse mechanisms in eight Galactic DNS systems by inferring progenitor mass of the second-born NS and the magnitude of the supernova kick it received at birth from measured DNS orbital parameters and kinematic information. Using these methods, they conclude that NS companions of PSRs B1534+12 and B1913+16 underwent iron core-collapse supernovae, while J0737−3039A's companion likely formed via electron capture supernova. This final result was corroborated by Ferdman et al. (2013); through detailed pulse profile shape analysis, they constrained the double pulsar system geometry, concluding that the secondary supernova explosion was relatively symmetric, indicative of an electron capture process.

There is a long history of work contributing to the idea that J0737−3039B formed via an electron capture supernova. Podsiadlowski et al. (2004) first suggested that the critical stellar mass required to form a NS (10−12 M_0 for solitary stars) should be significantly lower for tight, interacting binary systems (6−8 M_0). Based on early scintillation velocity measurements, constraints were placed on the progenitor mass of J0737−3039B and kick velocity due to its supernova (Willems & Kalogera, 2004; Piran & Shaviv, 2005; Willems et al., 2005, 2006). Precise transverse velocity measurements from an extended timing campaign provided the necessary information to claim an unusually low progenitor mass for J0737−3039B and corresponding low supernova kick velocity (Stairs et al., 2006; Piran & Shaviv, 2006).

We draw attention to the double pulsar system here to illustrate the detailed process that is required to make claims about DNS formation scenarios. As a result of the mass constraints presented in this paper, J1930−1852 appears to be in a DNS system. Its unique spin and orbital parameters challenge models that describe DNS formation.

In §4.2, we describe the GBT 350 MHz Drift Scan survey and the Pulsar Search Collaboratory, as well as the follow-up timing campaign and the parameters measured for J1930−1852; §4.3 provides evidence that a NS companion is likely, although radio follow-up observations have not provided any evidence of a pulsar companion. In §4.4, we draw conclusions from our findings and outline plans for future work.

4.2 Timing Observations & Analysis

In May–August of 2007, when the Green Bank Telescope (GBT) was undergoing track replacement, the GBT 350-MHz Drift Scan Pulsar Survey (Boyles et al., 2013; Lynch et al., 2013) looked for radio pulsars as the sky drifted overhead. Of the 1,491 hours of recorded drift scan data,

~300 hours were allocated to the Pulsar Search Collaboratory[2] (PSC). The survey and follow-up timing observing campaigns, processing pipeline and the students' first five discoveries are discussed in detail in Rosen et al. (2013). PSR J1930−1852 is the sixth pulsar discovered by PSC students.

After J1930−1852 was flagged by PSC students in late July of 2012, we confirmed the candidate with a long scan at 350 MHz with the GBT, at which point we also verified the binary nature of the source, given the significantly different measured spin period than that reported on the discovery plot. Soon after confirmation, we performed "gridding" observations, tiling the 350 MHz beam with seven 820 MHz beam positions, since the higher-frequency receiver has a smaller angular beam size on the sky (~0.25 deg compared to ~0.5 deg). As described by Morris et al. (2002), gridding reduces the uncertainty on the pulsar's position and makes it easier to eventually achieve a phase-connected timing solution. At the GBT, the 350 MHz prime-focus receiver is usually only mounted for several days each month, while the 820 MHz receiver is up for the rest of the month, so gridding also provided more flexibility in our follow-up timing campaign.

We first conducted high-cadence, then monthly timing observations once we had an orbital solution. We observed J1930−1852 at 350 MHz and (primarily) 820 MHz center frequencies, with 100 MHz and 200 MHz of bandwidth respectively. For all observations, we used the Green Bank Ultimate Pulsar Processing Instrument (GUPPI; DuPlain et al. (2008)) with 81.92 μs time resolution and 2048 frequency channels.

During each session, we observed J1930−1852 for ~15 mins, manually excised RFI with psrzap (part of the PSRCHIVE[3] software package, Hotan et al. (2004b)) and then summed the signal across the entire bandwidth. We summed across the time domain to generate one mean pulse profile per session and compared it with a synthetic standard profile to compute a time of arrival (TOA) using the PSRCHIVE routine pat. Standard profiles, one for each observing fre-

---

[2] The PSC (Rosen et al., 2010) aims to interest high-school students in science, technology, engineering and mathematics (STEM) related career paths, focusing especially on engaging women and minority students as well as those from low-income families.

[3] http://psrchive.sourceforge.net

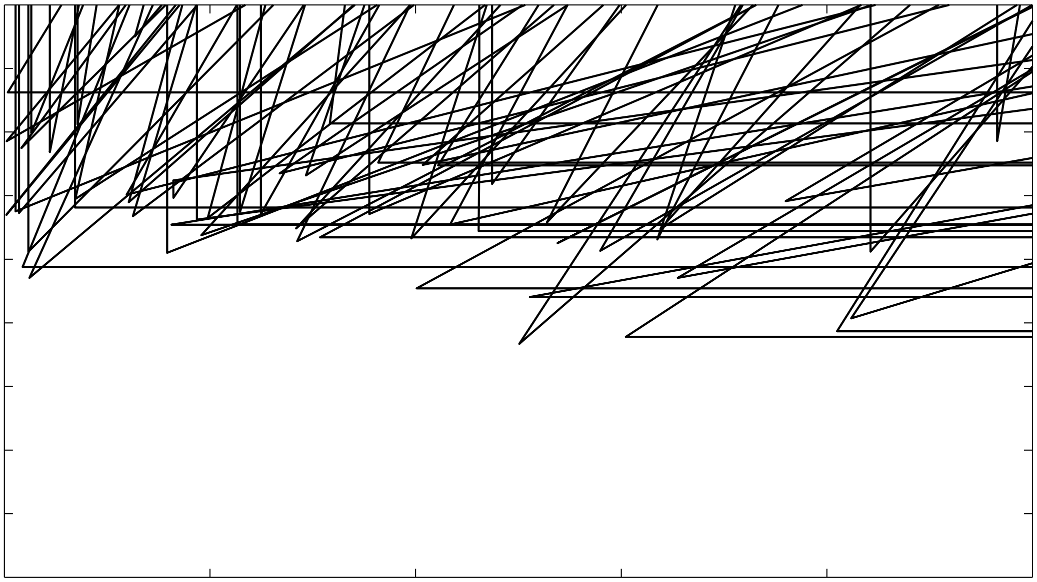

Figure 4.1: Roughness, calculated using trial orbital periods between 10 and 60 days. The clear minimum value of R at $P_{\rm orb} \sim 45$ days provided us with an initial orbital period for J1930−1852.

quency, were created by fitting Gaussian components to a high signal-to-noise profile.

Due to its orbital motion, the pulsar's intrinsic spin period is Doppler-shifted, such that the observed spin period $P_{\rm obs}$ varies periodically over time. At the beginning of our timing campaign, we measured J1930−1852's spin period at each observing epoch (see Figure 4.2), then used a *roughness* method from Bhattacharyya & Nityananda (2008) to solve for the system's orbital period, $P_{\rm orb}$. After choosing a trial $P_{\rm orb}$ and sorting measured spin periods by their respective orbital phases ($\varphi = 2\pi t/P_{\rm orb}$; t is time since periastron), the roughness parameter (R) can be calculated:

$$R = \sum_{i=1}^{N} \left[P_{\rm obs}(i) - P_{\rm obs}(i+1) \right]^2 , \tag{4.1}$$

where N is the number of adjacent pairs of data points. Trial $P_{\rm orb}$ values were chosen such that the increment, $\Delta P_{\rm orb}$ caused only a small orbital phase shift over the full data span (T), $(2\pi/P_{\rm orb}^2)\Delta P_{\rm orb} T \ll 1$. For trial $P_{\rm orb}$ values close to the true orbital period, $P_{\rm obs}(\varphi)$ varies smoothly

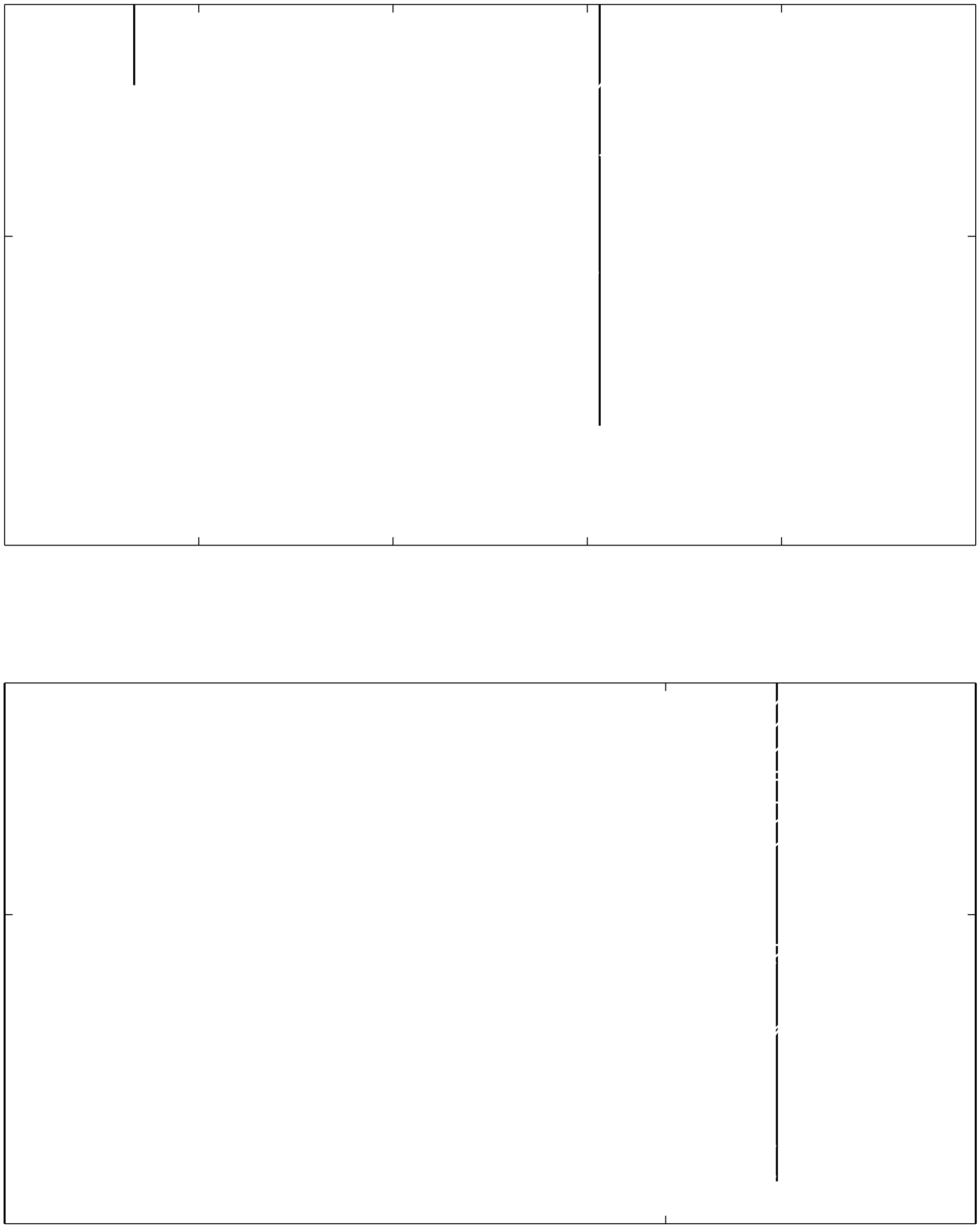

Figure 4.2: In both panels, black points show spin period measurements at various observing epochs with error bars, often smaller than the points themselves. The gray dashed lines illustrate predicted spin period versus phase (top panel) and versus time (bottom panel) based on our five Keplerian, orbital parameters. The apparent spin period variation shown here is a Doppler effect due to binary motion and the pulsar's intrinsic spin period and best fit binary parameters are given in Table 4.1.

Figure 4.3: Timing residuals for J1930−1852 plotted here correspond to fit parameters listed in Table 4.1. Red and black points represent 350 MHz and 820 MHz observations respectively. The group of 350 MHz TOAs at MJD 56904 come from a 3.5 hr observation at superior conjunction.

(e.g., see Figure 4.2, top panel) and R takes on a minimum value. We calculated roughness using trial orbital periods ranging from 0.1 to 300 days (Figure 4.1 shows $10 < P_{\rm orb} < 60$ days for clarity) and found that R is minimized for $P_{\rm orb} \sim 45$ days.

We further refined orbital parameters in TEMPO2[4] (Hobbs et al., 2006) to achieve a full, phase-connected solution, shown in Table 4.1. Our timing solution, in Barycentric Coordinate Time (TCB), uses the DE405 Solar System ephemeris and TT(BIPM) clock corrections. Subtracting TOAs from modeled arrival times determined by our phase-connected timing solution yields timing residuals shown in Figure 4.3. Since the reduced chi-squared statistic, $\chi^2_{\rm red} \sim 1$ for our timing residuals, we do not use a multiplicative "error factor" (EFAC), so uncertainties given in Table 4.1 are identical to those reported by TEMPO2.

On September 4, 2014, we observed J1930−1852 at superior conjunction (orbital phase, $\varphi \sim 0.373$) for 3.5 hrs with our normal 350 MHz setup described above. We obtained several TOAs from this epoch – displayed in Figure 4.3 and included in the timing solution reported in Table 4.1.

---

[4] http://tempo2.sourceforge.net

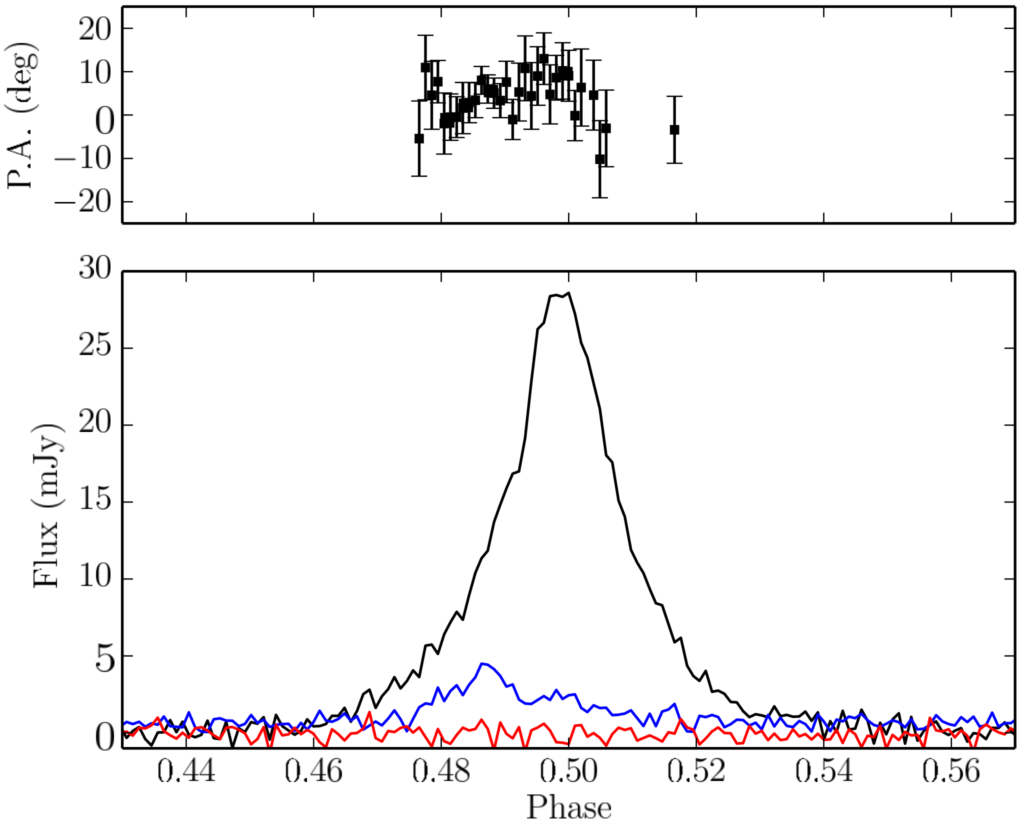

Figure 4.4: *Bottom panel:* A coherently dedispersed, flux- and polarization-calibrated pulse profile for J1930−1852 obtained from a 1 hr observation at 820 MHz with 200 MHz bandwidth and 1024 profile bins. The black line represents total intensity, while linear and circular polarization are shown in blue and red respectively. *Top panel:* The position angle (P.A.) swing due to slight linear polarization in the leading edge of the pulse profile.

Since the post-fit residuals did not show any sign of a Shapiro delay signature, we do not fit for Shapiro delay range (r) and shape (s) parameters here.

A flux- and polarization-calibrated, 820-MHz pulse profile for J1930−1852 is shown in Figure 4.4. About 15% of J1930−1852's emission is linearly polarized, but due to the relatively flat position angle curve, we were not able to fit this curve using the rotating vector model (Radhakrishnan & Cooke, 1969). There is no trace of circularly-polarized emission.

Spin & Astrometric Parameters	
Right Ascension (J2000)	19:30:29.7156(7)
Declination (J2000)	-18:51:46.27(6)
Spin Period (s)	0.18552016047926(8)
Period Derivative (s/s)	$1.8001(6)\times10^{-17}$
Dispersion Measure (pc cm^{-3})	42.8526(4)
Reference Epoch (MJD)	56513
Span of Timing Data (MJD)	56121−56904
Number of TOAs	75
RMS Residual (μs)	29
$\chi^2_{\rm red}$	1.05

Binary Parameters	
Orbital Period (days)	45.0600007(5)
Projected Semi-major Axis (lt-s)	86.890277(7)
Epoch of Periastron (MJD)	56526.642330(3)
Longitude of Periastron (deg)	292.07706(2)
Orbital Eccentricity	0.39886340(17)
Advance of Periastron (deg/yr)	0.00078(4)

Derived Parameters	
Surface Magnetic Field (10^{10} Gauss)	6.0
Spin-down Luminosity (10^{32} erg/s)	1.1
Characteristic Age (Myr)	163
Mass Function (M_8)	0.34690765(8)
Minimum Companion Mass (M_8)	1.30^5
Combined Mass (M_8)	2.59(4)
Mean S_{820} (mJy)	0.7

Table 4.1: Uncertainties in the last significant digit(s) are quoted in parentheses and represent 1σ errors on measured parameters. Since the flux density (S_{820}) quoted here is based on a single-epoch measurement, the uncertainty may be 10−20%.

4.3 Nature of the Companion

Given optical images of the sky surrounding J1930−1852 and mass constraints based on our timing solution (Table 4.1), the pulsar's companion is most likely another neutron star.

4.3.1 Optical Follow-up

Assuming the companion is a main sequence star, we can estimate its apparent bolometric magnitude and apparent SDSS g magnitude. First, with the mass-luminosity relation for an appropriate mass range $L_{\rm c,min}/{\rm L}_{0} = (m_{\rm c,min}/{\rm M}_{0})^{3.5}$ (Allen, 1973), where $m_{\rm c,min}$ is the minimum companion mass, we find $L_{\rm c,min} = 2.5\,{\rm L}_{0}$, which would correspond to an F5V spectral type. Next, using a DM-estimate distance, $d_{\rm DM} \sim 1.5\,$kpc (Cordes & Lazio, 2002) we estimate an apparent bolometric magnitude of $m_{\rm bol,c} = 14.7$. To convert this to an apparent g magnitude, we (i) applied a bolometric correction (BC ~ -0.09) to convert $m_{\rm bol,c}$ to an apparent V magnitude (Bessell et al., 1998), (ii) transformed this V magnitude to a SDSS g magnitude (Jester et al., 2005), and (iii) included the effects of extinction ($A_{\rm g} \sim 0.33\,$mag) using the estimates of Schlafly & Finkbeiner (2011). If the companion is a main sequence star, we find that it should have an apparent magnitude of $g_{\rm c} = 15.27$ or brighter.

We observed the field around J1930−1852 on the night of 9 May 2014 using the CTIO 0.9 m telescope, which was accessed through the sbs+10 (Subasavage et al., 2010) Consortium. We obtained 20 images of the field through a SDSS g filter ("CTIO 4770/1006") over the course of two hours; each individual exposure had an exposure time of 300 seconds, giving us a total integration time of 6000 seconds. To minimize processing time, we read out only a 291×375 pixel subsection of the full 2048×2048 pixel CCD, which, with a 0.401^{11}/pixel plate scale, gave us a $1.9^{1}\times2.5^{1}$ field of view (see Figure 4.5).

All frames were flat-fielded and bias-subtracted using standard routines in IRAF[6] (Tody, 1986),

---

[6] IRAF is distributed by the National Optical Astronomy Observatories, which are operated by the Association of Universities for Research in Astronomy, Inc., under cooperative agreement with the National Science Foundation.

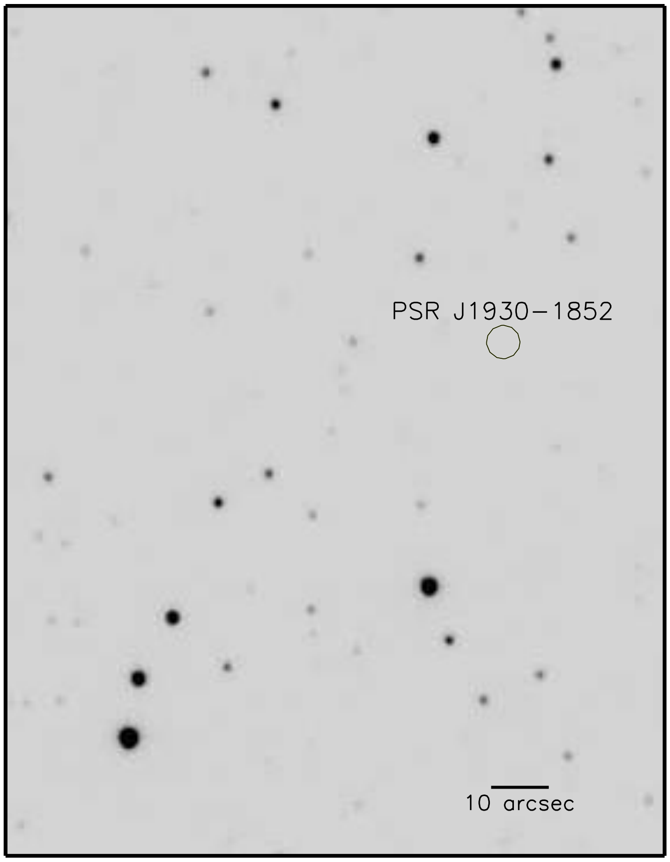

Figure 4.5: This $1.9^{1} \times 2.5^{1}$ field of view surrounding J1930−1852 is the result of stacking 20 300 s images taken with a SDSS *g* filter and the CTIO 0.9 m telescope. No objects were detected within a five-arcsecond radius around J1930−1852 — well beyond the uncertainties in measured position.

and the 20 reduced object frames were averaged together into a master frame with the imcombine task. We used *astrometry.net* to perform an astrometric calibration of the master frame to a precision of better than 0.1^{11}. To place an upper limit on the magnitude of any optical signatures, we first determined the aperture diameter that maximized the signal-to-noise (S/N) ratio in the photometry of nearby stars (2.4^{11}, or about two times the seeing); next, we calculated the number of counts in the area of sky centered on J1930−1852 and determined the level of noise at this position. Setting a 5σ detection threshold requirement for faint stars in the vicinity, we find a limiting magnitude of $g = 20.5$ for a possible optical counterpart of J1930−1852.

Since the estimated g magnitude for a MS star companion $g_\mathrm{c} = 15.27$ is ~125 times brighter than the limiting magnitude achieved here, we rule out a MS companion. The uncertainty in d_DM ($\sim 25\%$) does not alter this conclusion.

4.3.2 Mass Constraints

The mass function expresses the mass of the pulsar (m_p) and that of the companion (m_c) in terms of Keplerian orbital parameters $a_\mathrm{p} \sin i$ (projected semi-major axis) and P_b (orbital period). Using those measured parameters and setting the inclination angle $i = 90^\circ$, we place a lower limit on m_c for any given m_p.

The measurement of the relativistic advance of periastron ($\dot{\omega}$) also provides the system's total mass, $M_\mathrm{tot} = 2.59(4)\,M_0$. Taking $i = 90^\circ$, we use the mass function and double the uncertainties on M_tot to place 2σ lower/upper limits on the mass of the companion ($m_\mathrm{c} \geq 1.30\,M_0$) and the mass of the pulsar ($m_\mathrm{p} \leq 1.32\,M_0$) respectively. Shaded regions in Figure 4.6 show forbidden combinations of m_c and m_p based on orbital parameter measurements.

Considering the companion mass lower limit $m_\mathrm{c,LL} = 1.30\,M_0$, the orbital eccentricity $e \sim 0.4$, the spin period and period derivative of J1930−1852, a NS is the most likely companion.

Figure 4.6: A mass-mass diagram showing possible configurations of m_c and m_p for J1930−1852. The black shaded region is forbidden by the mass function, assuming $i = 90^\circ$. Since we have not yet measured J1930−1852's inclination, we choose $i = 90^\circ$ here because it is the least constraining.

The dashed red line shows $M_{tot} = 2.59\ M_0$, while red shaded regions are 2σ from this best value. Mass limits come from corners of forbidden regions on the mass-mass diagram; $m_c \geq 1.30\ M_0$and $m_p \leq 1.32\ M_0$.

4.3.3 Radio Follow-up

We dedispersed our 3.5 hr superior conjunction observation using the DM measured for J1930−1852 ($\mathrm{DM} = 42.85\,\mathrm{pc\,cm^{-3}}$), took a discrete Fourier Transform of the resulting timeseries and performed an acceleration search for a possible pulsar companion. To do so, we used the accelsearch routine from the PRESTO[7] suite of pulsar search software (Ransom, 2001), examining the frequency domain with a matched filter template up to 20 Fourier bins wide. To maximize our sensitivity to pulsars with narrow profiles, we summed up to 16 harmonics for candidate signals. This procedure returned over 800 high-significance ($S/N > 9$) candidates, from which we removed obvious RFI and those that were harmonically related to J1930−1852 or each other.

We folded and visually inspected the remaining candidates, but did not find any evidence of a pulsar counterpart. Assuming the harmonic summing was close to ideal, we were sensitive to $S/N > 9$ signals in the time domain, which corresponds to a 350 MHz flux limit of $\sim$30 μJy, given our observing set-up. These results suggest that a possible pulsar companion is either too weak to be detected or is not beaming along our line of sight. Given the sensitivity limit reached, the latter explanation is more likely.

4.4 Summary & Conclusions

Analysis presented in §4.3 implies that J1930−1852's most likely counterpart is another NS. We compare J1930−1852's parameters with those of other pulsars in known DNS systems that have similar evolutionary scenarios in Table 4.2. Given J1930−1852's moderately short spin period and period derivative well below those measured for otherwise similar unrecycled pulsars, J1930−1852 is partially recycled and therefore, most likely formed before its companion. On a $P - \dot{P}$ diagram (see Figure 4.7), J1930−1852 falls in the same region as other recycled DNS systems. Meanwhile, it has a longer spin period ($P_{\mathrm{spin}} \sim 185\,\mathrm{ms}$) and higher rate of spin-

---

[7] https://github.com/scottransom/presto

Figure 4.7: A P–$\dot{P}$ diagram showing all pulsars in DNS systems (stars/squares) and all other known pulsars (dots). Measured P and $\dot{P}$ come from the ATNF Pulsar Catalog (Manchester et al., 2005) and lines of characteristic age and surface magnetic field are shown with dot-dash and dashed lines, respectively. Recycled DNS pulsars (stars) appear between the normal and millisecond pulsar populations and are listed in Table 4.2. Despite its significantly longer spin period, J1930−1852 clearly belongs in the population of recycled DNS pulsars, unlike J1906+0746 and J0737−3039B (squares) – neither of which have undergone recycling.

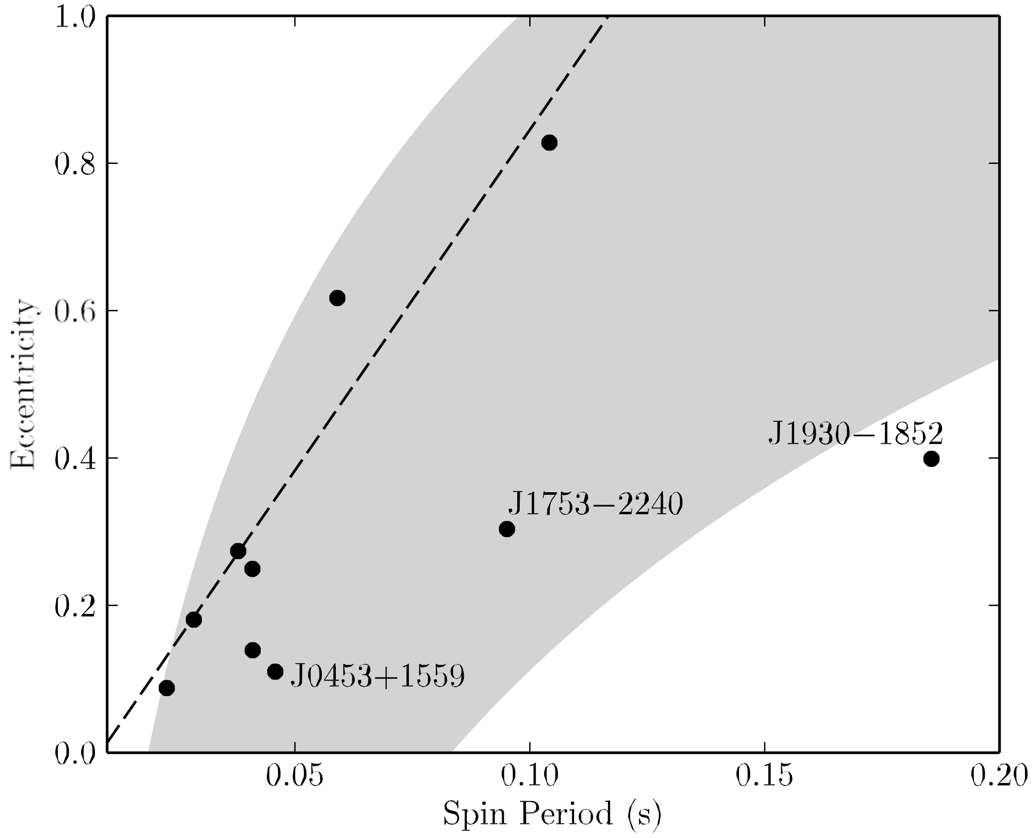

Figure 4.8: The dashed line shows the spin period-eccentricity relation first noted by McLaughlin et al. (2005) and Faulkner et al. (2005), which is simply a fit using the first seven known primary, partially-recycled DNS pulsars (unmarked points). The shaded region shows the approximate spread in properties of simulated DNS systems according to Dewi et al. (2005), assuming a small Maxwellian kick velocity dispersion induced by the second supernova ($\sigma_2 = 20\,\mathrm{km\,s^{-1}}$). Although we were unable to obtain actual population synthesis results from Figure 3 in that paper, we estimated the spread in spin period and eccentricity for simulated DNS systems by eye. PSRs J1753−2240 and J1930−1852 have been labeled because they both fall off the dashed line, but have spin periods and eccentricities that are still roughly consistent with the Dewi et al. (2005) synthetic population. PSR J0453+1559, a recently discovered DNS with a large mass asymmetry, described by Martinez et al. (2015), is consistent with the shaded region as well as the distribution of previously-discovered DNS pulsars shown here.

Pulsar	P_{spin} (ms)	$\dot{P}$ (10^{-18} s/s)	e	P_{orb} (days)	m_{p} ($M_\odot$)	m_{c} ($M_\odot$)	M_{tot} ($M_\odot$)	Recent References
J0737−3039A	22.7	1.8	0.09	0.10	1.34	1.25	2.59	Kramer et al. (2006)
J1756−2251	28.5	1.0	0.18	0.32	1.34	1.23	2.57	Ferdman et al. (2014)
B1913+16	59.0	8.6	0.62	0.32	1.44	1.39	2.83	Weisberg et al. (2010)
B1534+12	37.9	2.4	0.27	0.42	1.33	1.35	2.68	Fonseca et al. (2014)
J1829+2456	41.0	0.05	0.14	1.18	<1.34	>1.26	2.53	Champion et al. (2004, 2005)
J0453+1559	45.8	0.19	0.11	4.07	1.54	1.19	2.73	Martinez et al. (2015)
J1518+4904	40.9	0.03	0.25	8.63	<1.17	>1.55	2.72	Janssen et al. (2008)
J1753−2240	95.1	1.0	0.30	13.6	–	–	–	Keith et al. (2009)
J1811−1736	104	0.9	0.83	18.8	<1.64	>0.93	2.57	Corongiu et al. (2007)
J1930−1852	186	18	0.40	45.1	<1.32	>1.30	2.59	—

Table 4.2: A comparison between J1930−1852 and all other known primary, partially-recycled DNS pulsars, sorted by P_{orb}. PSRs J1906+0746 and J0737−3039B were omitted because neither underwent recycling (Lorimer et al., 2006a; Kramer et al., 2006). PSR B2127+11C (Jacoby et al., 2006) was also omitted because it was formed in a globular cluster, indicating a different evolutionary history.

down ($\dot{P} \sim 2 \times 10^{-17}$ s/s) than any other first-born, recycled DNS pulsar and an orbital period ($P_{\mathrm{b}} \sim 45$ days) longer than any other DNS system. These together may imply a shorter than average and/or inefficient mass transfer phase before the companion went supernova. Since accretion is thought to be the source of significant mass gain for recycled NSs (Zhang et al., 2011), a short and/or inefficient accretion period is consistent with the relatively low upper limit we place on the mass of J1930−1852, $m_{\mathrm{p}} < 1.32\, M_0$. The upper mass limit for J1930−1852 is lower than those of all other recycled DNS pulsars, except J1518+4904.

4.4.1 Spin Period–Eccentricity Relationship

The $P_{\mathrm{spin}} - e$ relationship was first noted in McLaughlin et al. (2005) and Faulkner et al. (2005), after the discoveries of J1756−2251 and J1829+2456; Faulkner et al. (2005) performed a linear fit in spin period/eccentricity space (see Figure 4.8), using the first seven known primary, partially recycled DNS pulsars and found a Pearson correlation coefficient $r = 0.97$. Monte Carlo simulations showed that such high r values would only be expected to occur by chance 0.1% of the time.

In the absence of a supernova kick, a positive correlation between eccentricity and spin period is expected. Without an appreciable kick, the DNS system's eccentricity following the second supernova explosion is directly proportional to the mass lost in the process (Willems et al., 2008). A lower-mass secondary will evolve more slowly, prolonging the mass transfer phase and allowing the primary more time to accrete material and spin up. The low-mass secondary loses relatively little mass during its supernova explosion, so the resulting DNS system (if it remains bound) has low eccentricity and a primary NS with a short spin period. Conversely, a high-mass secondary evolves more quickly. A short mass transfer phase before the secondary's supernova leaves the primary with a long spin period; greater mass loss during the supernova results in a DNS system with high eccentricity.

Using population synthesis simulations of DNS formation, Dewi et al. (2005) show that this expected $P_{\rm spin} - e$ relationship persists for small supernova kick velocities. The authors assume standard and double-core formation scenarios and that most of the matter accreted by the primary NS comes from a helium star companion during the He-star–NS binary mass transfer phase. Finally, they assume that the accretion rate is limited by the Eddington rate for helium accretion and invoke a model to account for accretion-induced spin-up of the primary NS. By applying a small Maxwellian kick velocity distribution with dispersion $\sigma_2 = 20\,{\rm km\,s^{-1}}$ for the secondary supernova explosion, the distribution of simulated DNS systems exhibits a slope similar to that of the empirical $P_{\rm spin} - e$ relationship first noted by McLaughlin et al. (2005) and Faulkner et al. (2005). The $P_{\rm spin} - e$ relationship is maintained in the simulated population for $\sigma < 50\,{\rm km\,s^{-1}}$, regardless of the kick velocity imparted by the primary supernova.

We plot a representation of the simulated DNS population from Dewi et al. (2005) as a shaded region in Figure 4.8. Keith et al. (2009) used a similar representation to argue that J1753−2240 is perhaps more representative of the DNS population than previously discovered DNS pulsars, which all lie closer to the more sparsely-populated, low-$P_{\rm spin}$ edge of the shaded region. Although J1930−1852 appears to be approximately consistent with the Dewi et al. (2005) simulations, its location in a sparsely-populated portion of the proposed $P_{\rm spin} - e$ distribution draws the model's assumptions and conclusions into question.

In their paper, Dewi et al. note that the $P_{\mathrm{spin}} - e$ relationship is destroyed (randomized) in a simulated population of DNS systems with high supernova kick velocities ($\sigma > 50\,\mathrm{km\ s^{-1}}$). There is good evidence (e.g. Wong et al., 2010) that both B1913+16 and B1534+12 require high supernova kicks, possibly $\gg 150\,\mathrm{km\ s^{-1}}$, but these DNS systems remain completely consistent with the simulated distribution of systems with low kick velocities shown in Figure 4.8. Therefore, there is currently no known DNS system that supports the claim from Dewi et al. (2005) that high supernova kick velocity systems do not follow a $P_{\mathrm{spin}} - e$ relationship. However, J1930−1852 (like J1753−2240) provides further evidence that any relationship between spin period and eccentricity is probably much broader than was originally thought.

4.4.2 Orbital Period-Eccentricity Relationship

For short orbital period binary systems, one would expect a prolonged or more efficient recycling process than for long orbital period systems. Since the amount of recycling that occurs is inversely related to both orbital period and spin period, these quantities are expected to track one another (i.e. long orbital period DNS binaries should have long spin periods). We see this relationship in the known DNS population and Table 4.2 illustrates it nicely. Building on arguments in §4.4.1, we expect DNS systems with longer orbital periods to also have larger eccentricities. Chaurasia & Bailes (2005) show that eccentric, short orbtial period binary systems tend to rapidly circularize due to gravitational radiation. This mechanism also contributes to the expected orbital period-eccentricity relationship in DNS binaries.

Andrews et al. (2015) simulate DNS system formation, considering three dominant evolutionary channels for the primary NS's companion: (i) wide-orbit common envelope, followed by iron core-collapse supernova, (ii) tight-orbit common envelope, followed by a second round of mass transfer, then iron core-collapse supernova, and (iii) similar to channel ii, but a lower-mass secondary He core forms a NS through electron capture supernova. Using currently understood evolutionary histories for PSRs J0737−3039A/B, B1534+12 and B1913+16, the authors constrain DNS population models and binary parameters. For each synthetic population representing a given model, they compare confidence intervals that result from simulations to the actual DNS population in the $P_b - e$ plane. Confidence intervals for all evolutionary channels combined follow a roughly positive slope in the $P_b - e$ plane, as one would expect. High-confidence regions shift depending on the chosen set of model parameters and evolutionary channel. For example, higher supernova kick velocities tend to produce systems with higher eccentricities; decreasing the efficiency of the common envelope ejection mechanism produces systems with wider orbits. Of the three evolutionary channels, the first typically has the broadest distribution in orbital period. In most cases (i.e. for most chosen sets of model parameters), the known DNS population falls well within 3σ confidence intervals considering all evolutionary channels (i, ii and iii) combined. Comparing J1930−1852's parameters to the confidence intervals shown for the reference model in Andrews et al. (2015) (Figure 1 in that paper), the combination of orbital period and eccentricity is inconsistent with simulated parameters of systems from the three dominant evolutionary channels at the $4 - 5\sigma$ level. Many models in Andrews et al. (2015) do not produce systems like J1930−1852, which suggests that it may be useful for constraining theory.

4.4.3 Future Work

PSR J1930−1852's parameters set it apart from previously-studied primary DNS pulsars: the widest orbit (longest orbital period), the longest spin period, the largest spin-down rate. We hope to determine the pulsar and companion masses independently and accurately measure proper motion to infer (i) the progenitor mass of the second-born NS and (ii) the magnitude of the supernova kick it received at birth. Then, following work by Wong et al. (2010), we can make meaningful predictions about J1930−1852's true evolutionary history.

So far, we detect no Shapiro delay signature in our timing residuals (see Figure 4.3), despite having good orbital coverage and a 3.5 hr superior conjunction observation. This non-detection could be a result of a combination of factors including: inadequate timing precision, low companion mass and/or small inclination angle. If the non-detection is related to timing precision, continued timing observations may result in a measurement of the delay, and hence an additional constraint on the companion mass.

Upcoming VLBA observations will provide high-precision position, proper motion and parallax measurements, which will help isolate spin, orbital and post-Keplerian parameters in our timing residual fits. Also, because J1930−1852 is relatively nearby ($d_{\rm DM} \sim 1.5$ kpc), we will be able to resolve the orbit with VLBA imaging; at the estimated distance, the major axis of J1930−1852's orbit spans ~250 μas and the VLBA routinely obtains 50 μas precision or better with an in-beam calibrator available (Deller et al., 2012). Resolving the orbit will allow us to place constraints on the system's inclination angle and in turn, the masses of J1930−1852 and its companion. These measurements are critical for eventually understanding the formation scenario for J1930−1852 and other wide-orbit DNS systems.

Acknowledgements

We thank Robert Ferdman, Ingrid Stairs and Jeffrey Andrews for useful discussions. The PSC was funded through NSF ITEST award number 0737641. J.K.S., M.A.M., and D.R.L. are supported through NSF PIRE award number 0968296. T.H., E.F., J.A.M, and B.N.B. acknowledge High Point University, which provided the financial support necessary to conduct the photometric observations on-site at the CTIO 0.9-m telescope. The National Radio Astronomy Observatory is a facility of the National Science Foundation operated under cooperative agreement by Associated Universities, Inc.

Chapter 5

Conclusions & Future Work

5.1 Understanding the MSP Population

In a review of PTA science and progress, McLaughlin (2014) points out that $20-30$ MSPs have been discovered annually since 2009 due to successful blind radio surveys (e.g. PALFA, GBNCC and HTRU) and radio searches targeting unidentified *Fermi* point sources; the first MSP was discovered in 1982 and the MSP population has *tripled* since 2008. This boom in MSP discoveries in recent years makes the population ripe for more detailed analysis. Lorimer et al. (2015) have already provided a more accurate model for MSP spin periods; further studies investigating the MSP luminosity function and radial distribution will improve our ability to predict survey yields and design future surveys that will add to the growing pool of possible PTA sources.

In Chapter 2 of this thesis, I described a method for estimating the size of the potentially-detectable Galactic MSP population, which is highly uncertain ($N_{\rm MSP} = 15,000^{+85,000}_{-6,000}$). Based on this estimate, I predicted 12^{+70}_{-5} MSP detections in the PALFA survey by early 2014 and 31 were actually detected. With slightly more sky coverage, the PALFA survey has now detected ~ 50 MSPs, including 17 discoveries Lazarus et al. (2015). Based on these results, the full PALFA survey could provide much better constraints on the size of the underlying MSP population.

While adding more pulsars is currently the best way to improve our sensitivity to a stochastic background of GWs (Siemens et al., 2013), Burt et al. (2011) and Simon et al. (2014) propose ways in which we can improve PTA sensitivity to *continuous* GW sources (e.g. supermassive black hole binary systems), which has inspired an all-sky MSP sensitivity map (see Figure 5.1). Representing a true comparison between surveys that use different center frequencies requires making assumptions about the MSP spectral index and assessing their various sensitivites requires some

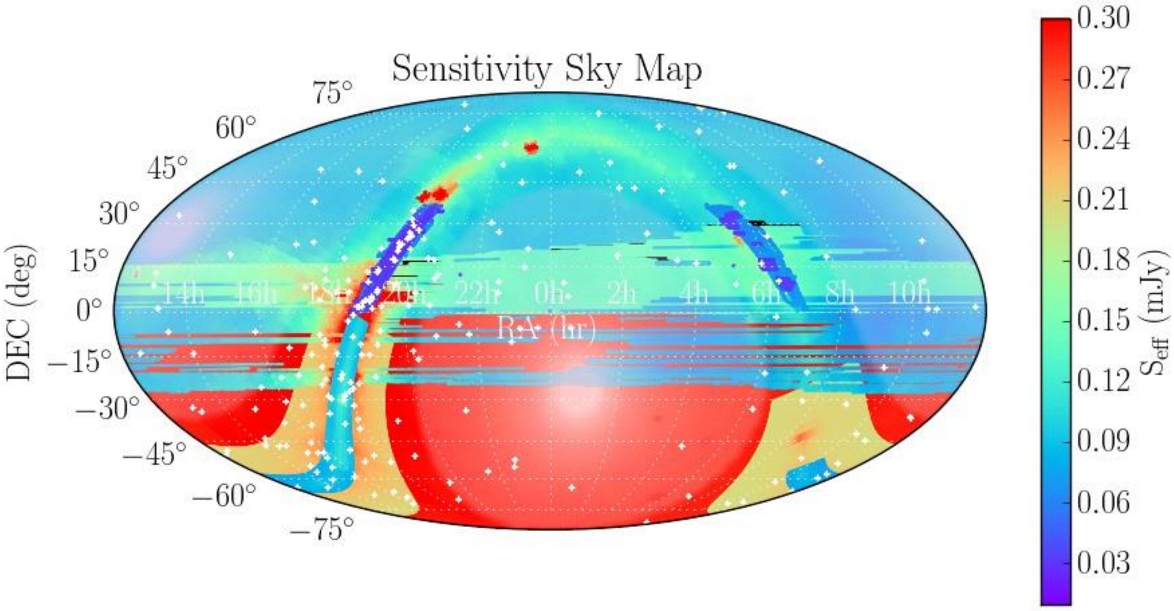

Figure 5.1: This plot shows a realization of the minimum sensitivities of current pulsar surveys, scaled to $f_{\mathrm{obs}} = 1.4$ GHz, considering a test source with $P_{\mathrm{spin}} = 3$ ms, DM = 75 pc/cc, duty cycle $\delta = 0.1$ and spectral index $\alpha = -1.9$. Sky coverage shown here is from the PALFA, GBNCC, HTRU (low-, mid- and high-latitude), GBT 350 MHz Drift Scan and Arecibo 327 MHz Drift Scan surveys. The color scale indicates the effective minimum sensitivity to the test source reached at each sky position. Partially-transparent white regions show portions of sky in which the expected DM (Cordes & Lazio, 2002) is smaller than the DM of the test source. All known MSPs in the Galactic field (excluding those in globular clusters) are plotted as white crosses.

knowledge of MSP flux. Due to the small sample size of MSPs in the past, flux and spectral index distributions have not been well-determined, but NANOGrav alone gets regular polarization and flux-calibrated observations of ∼ 40 MSPs (Arzoumanian et al., 2015), automatically providing a high-quality data set to begin adressing questions about MSP fluxes and survey sensitivity to MSPs.

5.2 An 820 MHz survey of the Cygnus-X region

Pulsar surveys with added sensitivity and/or those probing new frequency regimes access new “phase spaces" of the pulsar population and discover sources that push the boundaries of our understanding. This has certainly been true of the PSC portion of the 350 MHz Drift Scan survey, which has turned up a nearby MSP, a disrupted recycled pulsar, a DNS system and an extreme nuller, among others (see Chapters 3 and 4). The Cygnus-X region, $75^\circ < \ell < 94^\circ$ and $-3^\circ < b < 6^\circ$ has been the subject of multi-wavelength studies in the past (Cygnus-X Spitzer Legacy Survey, Chandra Cygnus OB2 Legacy Survey, Herschel imaging survey of OB Young Stellar objects, etc.), but past pulsar surveys have been lacking in the region; surveys that have covered Cygnus-X in the past have done so at low frequency where background sky temperatures in the Galactic plane degrade sensitivity. The 15 known pulsars in the region have DMs ranging from 93–429 pc cm^{-3} and several (like J2021+3651) show significant scattering, even at 1.4 GHz (Roberts et al., 2002).

Surveying the Cygnus-X region with the Green Bank Telescope at 820 MHz will provide more than a factor of two improvement over previous GBT low-frequency surveys, avoiding some of the deleterious effects of scatter broadening and dispersive smearing, while still taking advantage of pulsars' higher flux below the more typical 1.4 GHz center frequency. Simulations predict ~ 60 discoveries, including five new MSPs in ~ 450 hours, a discovery rate slightly better than PALFA's (one discovery per ~ 10 hours). This survey will be a pilot program for a potential, large-scale 820 MHz survey using the multipixel Academia Sinica Institute of Astronomy & Astrophysics (ASIAA) feed, which may be available in several years. A multipixel, 820 MHz receiver at the GBT would make an ideal system for conducting an efficient, all-sky survey targeting MSPs.

Since Cygnus-X is a rich star-forming region in the Galactic plane, we expect to find young pulsars that have not yet migrated far from their birthplaces in the plane. Young pulsars have large spindown rates and some have measurable braking indices that provide insight into various factors contributing to pulsar spindown, like magnetic braking and winds. When these pulsars can be associated with supernova remnants, we can get independent estimates of neutron star ages. Although population simulations predict only a handful of detectable MSPs in the region, surveying at 820 MHz, we will have access to sources previously undetectable due to smearing. Since there are no known MSPs in the Cygnus-X region to date, new discoveries will help improve PTA sky coverage for GW detection.

A portion of the Cygnus-X survey data will be processed and reserved for outreach purposes, involving high school and undergraduate students in current, hands-on research.

5.3 Student Involvement

Last summer, Sonny Ernst (Rowan County H.S.) discovered PSR J1955+10 (see Chapter 3) in a single pulse plot generated from 350 MHz Drift Scan survey data. Since the pulsar was not also found in periodicity searches, we did not initially have a spin period from the discovery. Being a particularly enthusiastic student, Sonny wanted to get involved with further analysis, so for the first few months of follow-up timing, I generated dedispersed timeseries using the discovery DM, then sent him lists of high S/N pulses with timestamps so that he could figure out the pulse period on his own. After three or four timing observations, Sonny was able to find a consistent pulse period, which I used to start folding the data to make TOAs and get a timing solution.

Under normal operation, the Pulsar Search Collaboratory (see Chapter 3) involves students in pulsar survey data analysis and candidate selection, but there is little for students to do after a discovery is made. Some more interested students have participated in timing observations via Skype, but outlets for especially enthusiastic students like Sonny are rare.

As the PSC prepares to scale up with additional funding, it will be important to give specific thought to new activities that allow for additional/enhanced student participation. Online infrastructure will be particularly important for remote access and establishing tiered mentorship programs at partner universities – between faculty, post-docs, graduate students, undergrads and high school students – will help increase the amount of one-on-one time participants have with local experts.

Bibliography

Allen, B., et al. 2013, ApJ, 773, 91

Allen, C. W. 1973, Astrophysical quantities

Alpar, M. A., Cheng, A. F., Ruderman, M. A., & Shaham, J. 1982a, Nature, 300, 728

—. 1982b, Nature, 300, 728

Andrews, J. J., Farr, W. M., Kalogera, V., & Willems, B. 2015, ApJ, 801, 32

Arzoumanian, Z., et al. 2015, ArXiv e-prints

Bagchi, M. 2013, International Journal of Modern Physics D, 22, 30021

Bailes, M. 1989, ApJ, 342, 917

Bailes, M., et al. 2011, Science, 333, 1717

Bates, S. D., Lorimer, D. R., Rane, A., & Swiggum, J. 2014, MNRAS, 439, 2893

Bates, S. D., Lorimer, D. R., & Verbiest, J. P. W. 2013, MNRAS, 431, 1352

Bates, S. D., et al. 2011, MNRAS, 416, 2455

Belczynski, K., Lorimer, D. R., Ridley, J. P., & Curran, S. J. 2010, MNRAS, 407, 1245

Bessell, M. S., Castelli, F., & Plez, B. 1998, A&A, 333, 231

Bhat, N. D. R., Cordes, J. M., Camilo, F., Nice, D. J., & Lorimer, D. R. 2004, ApJ, 605, 759

Bhattacharya, D., Wijers, R. A. M. J., Hartman, J. W., & Verbunt, F. 1992, A&A, 254, 198

Bhattacharyya, B., & Nityananda, R. 2008, MNRAS, 387, 273

Biggs, J. D. 1992, ApJ, 394, 574

Blaauw, A. 1961, B.A.N., 15, 265

Boyles, J., et al. 2013, ApJ, 763, 80

Burgay, M., et al. 2003, Nature, 426, 531

—. 2013, MNRAS, 433, 259

Burt, B. J., Lommen, A. N., & Finn, L. S. 2011, ApJ, 730, 17

Carroll, B. W., & Ostlie, D. A. 2006, An Introduction to Modern Astrophysics and Cosmology (Pearson Education, Inc.)

Champion, D. J., Lorimer, D. R., McLaughlin, M. A., Cordes, J. M., Arzoumanian, Z., Weisberg, J. M., & Taylor, J. H. 2004, MNRAS, 350, L61

Champion, D. J., et al. 2005, MNRAS, 363, 929

Chatterjee, S., et al. 2009, ApJ, 698, 250

Chaurasia, H. K., & Bailes, M. 2005, ApJ, 632, 1054

Cocke, W. J., Disney, M. J., & Taylor, D. J. 1969, Nature, 221, 525

Cordes, J. M., & Chernoff, D. F. 1997, ApJ, 482, 971

Cordes, J. M., & Lazio, T. J. W. 2002, ArXiv Astrophysics e-prints

Cordes, J. M., & Shannon, R. M. 2008, ApJ, 682, 1152

Cordes, J. M., et al. 2006, ApJ, 637, 446

Corongiu, A., Kramer, M., Stappers, B. W., Lyne, A. G., Jessner, A., Possenti, A., D’Amico, N., & Löhmer, O. 2007, A&A, 462, 703

Crawford, F., et al. 2012, ApJ, 757, 90

de Jager, O. C., Raubenheimer, B. C., & Swanepoel, J. W. H. 1989, A&A, 221, 180

Deller, A. T., et al. 2012, ApJ, 756, L25

Demorest, P. B., et al. 2013, ApJ, 762, 94

Dewey, R. J., Taylor, J. H., Weisberg, J. M., & Stokes, G. H. 1985, ApJ, 294, L25

Dewi, J. D. M., Podsiadlowski, P., & Pols, O. R. 2005, MNRAS, 363, L71

Dowd, A., Sisk, W., & Hagen, J. 2000, in Astronomical Society of the Pacific Conference Series, Vol. 202, IAU Colloq. 177: Pulsar Astronomy - 2000 and Beyond, ed. M. Kramer, N. Wex, & R. Wielebinski, 275–276

DuPlain, R., Ransom, S., Demorest, P., Brandt, P., Ford, J., & Shelton, A. L. 2008, in Society of Photo-Optical Instrumentation Engineers (SPIE) Conference Series, Vol. 7019, Society of Photo-Optical Instrumentation Engineers (SPIE) Conference Series, 1

Faucher-Giguère, C.-A., & Kaspi, V. M. 2006, ApJ, 643, 332

Faulkner, A. J., et al. 2004, MNRAS, 355, 147

—. 2005, ApJ, 618, L119

Faulkner, J., & Gribbin, J. R. 1968, Nature, 218, 734

Ferdman, R. D., et al. 2013, ApJ, 767, 85

—. 2014, MNRAS, 443, 2183

Fonseca, E., Stairs, I. H., & Thorsett, S. E. 2014, ApJ, 787, 82

Freire, P. C. C., et al. 2011, MNRAS, 412, 2763

Gold, T. 1968, Nature, 218, 731

Greenstein, G. 1983, Frozen star

Haslam, C. G. T., Salter, C. J., Stoffel, H., & Wilson, W. E. 1982, A&AS, 47, 1

Hewish, A., Bell, S. J., Pilkington, J. D. H., Scott, P. F., & Collins, R. A. 1968, Nature, 217, 709

Hobbs, G., Lorimer, D. R., Lyne, A. G., & Kramer, M. 2005, MNRAS, 360, 974

Hobbs, G., et al. 2004, MNRAS, 352, 1439

Hobbs, G. B., Edwards, R. T., & Manchester, R. N. 2006, MNRAS, 369, 655

Hotan, A. W., van Straten, W., & Manchester, R. N. 2004a, PASA, 21, 302

—. 2004b, PASA, 21, 302

Jackson, J. D. 1962, Classical Electrodynamics

Jacoby, B. A., Cameron, P. B., Jenet, F. A., Anderson, S. B., Murty, R. N., & Kulkarni, S. R. 2006, ApJ, 644, L113

Janssen, G. H., Stappers, B. W., Kramer, M., Nice, D. J., Jessner, A., Cognard, I., & Purver, M. B. 2008, A&A, 490, 753

Jenet, F. A., Hobbs, G. B., Lee, K. J., & Manchester, R. N. 2005, ApJ, 625, L123

Jester, S., et al. 2005, AJ, 130, 873

Johnston, S., Manchester, R. N., Lyne, A. G., Bailes, M., Kaspi, V. M., Qiao, G., & D’Amico, N. 1992, ApJ, 387, L37

Kaspi, V. M., Johnston, S., Bell, J. F., Manchester, R. N., Bailes, M., Bessell, M., Lyne, A. G., & D’Amico, N. 1994, ApJ, 423, L43

Keith, M. J., Kramer, M., Lyne, A. G., Eatough, R. P., Stairs, I. H., Possenti, A., Camilo, F., & Manchester, R. N. 2009, MNRAS, 393, 623

Keith, M. J., et al. 2010, MNRAS, 409, 619

Kim, C., Bhakthi Pranama Perera, B., & McLaughlin, M. A. 2013, ArXiv e-prints

Kim, C., Kalogera, V., & Lorimer, D. 2010, New Astronomy Reviews, 54, 148

Kramer, M., Xilouris, K. M., Lorimer, D. R., Doroshenko, O., Jessner, A., Wielebinski, R., Wolszczan, A., & Camilo, F. 1998, ApJ, 501, 270

Kramer, M., et al. 2003, MNRAS, 342, 1299

—. 2006, Science, 314, 97

Large, M. I., Vaughan, A. E., & Mills, B. Y. 1968, Nature, 220, 340

Lazarus, P. 2013, in IAU Symposium, Vol. 291, IAU Symposium, ed. J. van Leeuwen, 35–40

Lazarus, P., et al. 2015, ArXiv e-prints

Levin, L., et al. 2013, MNRAS, 434, 1387

Lommen, A. N., Kipphorn, R. A., Nice, D. J., Splaver, E. M., Stairs, I. H., & Backer, D. C. 2006, ApJ, 642, 1012

Lorimer, D. R. 1995, MNRAS, 274, 300

—. 2001, Living Reviews in Relativity, 4, 5

—. 2005, Living Reviews in Relativity, 8, 7

—. 2008, Living Reviews in Relativity, 11, 8

—. 2010, Highlights of Astronomy, 15, 807

Lorimer, D. R. 2013, in IAU Symposium, Vol. 291, IAU Symposium, ed. J. van Leeuwen, 237–242

Lorimer, D. R., Bailes, M., Dewey, R. J., & Harrison, P. A. 1993, MNRAS, 263, 403

Lorimer, D. R., & Kramer, M. 2004, Handbook of Pulsar Astronomy (UK: Cambridge University Press)

Lorimer, D. R., et al. 2004, MNRAS, 347, L21

—. 2006a, ApJ, 640, 428

—. 2006b, MNRAS, 372, 777

—. 2015, MNRAS, 450, 2185

Lynch, R. S., et al. 2013, ApJ, 763, 81

Lyne, A. G., & Graham-Smith, F. 1998, Pulsar astronomy (U.K.; New York : Cambridge University Press)

Manchester, R. N., Hobbs, G. B., Teoh, A., & Hobbs, M. 2005, AJ, 129, 1993

Manchester, R. N., et al. 2001, MNRAS, 328, 17

Maran, S. P., & Cameron, A. G. W. 1968, Physics Today, 21, 41

Martinez, J. G., et al. 2015, ApJ, 812, 143

McLaughlin, M. A. 2014, ArXiv e-prints

McLaughlin, M. A., et al. 2005, in Astronomical Society of the Pacific Conference Series, Vol. 328, Binary Radio Pulsars, ed. F. A. Rasio & I. H. Stairs, 43

McLaughlin, M. A., et al. 2006, Nature, 439, 817

Meltzer, D. W., & Thorne, K. S. 1966, ApJ, 145, 514

Mickaliger, M. B., et al. 2012, ApJ, 759, 127

Morris, D. J., et al. 2002, MNRAS, 335, 275

Nice, D. J., et al. 2013, ApJ, 772, 50

Nomoto, K. 1984, ApJ, 277, 791

Ostriker, J. 1968, Nature, 217, 1227

Özel, F., Psaltis, D., Narayan, R., & Santos Villarreal, A. 2012, ApJ, 757, 55

Pacini, F., & Salpeter, E. E. 1968, Nature, 218, 733

Pilkington, J. D. H., Hewish, A., Bell, S. J., & Cole, T. W. 1968, Nature, 218, 126

Piran, T., & Shaviv, N. J. 2005, Physical Review Letters, 94, 051102

—. 2006, ArXiv Astrophysics e-prints

Podsiadlowski, P., Langer, N., Poelarends, A. J. T., Rappaport, S., Heger, A., & Pfahl, E. 2004, ApJ, 612, 1044

Radhakrishnan, V., & Cooke, D. J. 1969, ApJ letters, 3, 225

Ransom, S. M. 2001, PhD thesis, Harvard University

Ransom, S. M., Eikenberry, S. S., & Middleditch, J. 2002, AJ, 124, 1788

Richards, D. W., & Comella, J. M. 1969, Nature, 222, 551

Ritchings, R. T. 1976, MNRAS, 176, 249

Roberts, M. S. E., Hessels, J. W. T., Ransom, S. M., Kaspi, V. M., Freire, P. C. C., Crawford, F., & Lorimer, D. R. 2002, ApJ, 577, L19

Rosen, R., et al. 2010, Astronomy Education Review, 9, 010106

—. 2013, ApJ, 768, 85

Schlafly, E. F., & Finkbeiner, D. P. 2011, ApJ, 737, 103

Schwab, J., Podsiadlowski, P., & Rappaport, S. 2010, ApJ, 719, 722

Shapiro, I. I. 1964, Physical Review Letters, 13, 789

Siemens, X., Ellis, J., Jenet, F., & Romano, J. D. 2013, Classical and Quantum Gravity, 30, 224015

Simon, J., Polin, A., Lommen, A., Stappers, B., Finn, L. S., Jenet, F. A., & Christy, B. 2014, ApJ, 784, 60

Smits, R., Lorimer, D. R., Kramer, M., Manchester, R., Stappers, B., Jin, C. J., Nan, R. D., & Li, D. 2009, A&A, 505, 919

Spitler, L. G., et al. 2014, ApJ, 790, 101

Stairs, I. H., Thorsett, S. E., Dewey, R. J., Kramer, M., & McPhee, C. A. 2006, MNRAS, 373, L50

Stairs, I. H., et al. 2001, MNRAS, 325, 979

Stovall, K., et al. 2014, ApJ, 791, 67

Subasavage, J. P., Bailyn, C. D., Smith, R. C., Henry, T. J., Walter, F. M., & Buxton, M. M. 2010, in Society of Photo-Optical Instrumentation Engineers (SPIE) Conference Series, Vol. 7737, Society of Photo-Optical Instrumentation Engineers (SPIE) Conference Series

Swiggum, J. K., et al. 2014, ApJ, 787, 137

Tauris, T. M., Langer, N., & Podsiadlowski, P. 2015, ArXiv e-prints

Tauris, T. M., & Savonije, G. J. 1999, A&A, 350, 928

Thorsett, S. E., Arzoumanian, Z., & Taylor, J. H. 1993, ApJ, 412, L33

Thorsett, S. E., & Chakrabarty, D. 1999, ApJ, 512, 288

Tody, D. 1986, in Society of Photo-Optical Instrumentation Engineers (SPIE) Conference Series, Vol. 627, Instrumentation in astronomy VI, ed. D. L. Crawford, 733

Toscano, M., Bailes, M., Manchester, R. N., & Sandhu, J. S. 1998, ApJ, 506, 863

Toscano, M., Sandhu, J. S., Bailes, M., Manchester, R. N., Britton, M. C., Kulkarni, S. R., Anderson, S. B., & Stappers, B. W. 1999, MNRAS, 307, 925

Vivekanand, M., & Narayan, R. 1981, Journal of Astrophysics and Astronomy, 2, 315

Wang, N., Manchester, R. N., & Johnston, S. 2007, MNRAS, 377, 1383

Weisberg, J. M., Nice, D. J., & Taylor, J. H. 2010, ApJ, 722, 1030

Willems, B., Andrews, J., Kalogera, V., & Belczynski, K. 2008, in American Institute of Physics Conference Series, Vol. 983, 40 Years of Pulsars: Millisecond Pulsars, Magnetars and More, ed. C. Bassa, Z. Wang, A. Cumming, & V. M. Kaspi, 464–468

Willems, B., & Kalogera, V. 2004, ApJ Letters, 603, L101

Willems, B., Kalogera, V., & Henninger, M. 2005, in Astronomical Society of the Pacific Conference Series, Vol. 328, Binary Radio Pulsars, ed. F. A. Rasio & I. H. Stairs, 123

Willems, B., Kaplan, J., Fragos, T., Kalogera, V., & Belczynski, K. 2006, PhRvD, 74, 043003

Wolszczan, A. 1994, Science, 264, 538

Wong, T.-W., Willems, B., & Kalogera, V. 2010, ApJ, 721, 1689

Woosley, S. E., & Weaver, T. A. 1986, ARA&A, 24, 205

Zhang, C. M., et al. 2011, A&A, 527, A83